Synthesis, Characterization, and Molecular Dynamics Analysis of Ultrathin Amorphous Carbon Films

by

Na Wang

A dissertation submitted in partial satisfaction of the

requirements for the degree of

Doctor of Philosophy

in

Engineering – Mechanical Engineering

in the

Graduate Division

of the

University of California at Berkeley

Committee in charge:
Professor Kyriakos Komvopoulos, Chair
Professor Hari Dharan
Professor Ron Gronsky

Fall 2013

Abstract

Synthesis, Characterization, and Molecular Dynamics Analysis of Ultrathin Amorphous
Carbon Films

by

Na Wang

Doctor of Philosophy in Engineering-Mechanical Engineering

University of California, Berkeley

Professor Kyriakos Komvopoulos, Chair

Increasing demands for high magnetic storage capacity have led to the increase of the recording area density by more than 100,000 times over the past 30 years. Among all the approaches considered to increase the area density, reducing the magnetic spacing is an effective solution that directly impacts the thickness and quality of the carbon overcoat. One of the methods of carbon overcoat deposition is chemical vapor deposition, which uses carbon-containing precursor gases as the source of carbon radicals and atoms to form the carbon overcoat. The produced carbon film is characterized by high hydrogen content (20%–50%), depending on the carbon-to-hydrogen ratio of the precursor gas and process parameters. Because of the hydrogen content, CVD-deposited hydrogenated amorphous carbon (a-C:H) deposited by CVD exhibit density of 1.7–2.2 g/cm^3, which is much lower than the density (~3 g/cm^3) of hydrogen-free amorphous carbon (a-C) films deposited by filtered cathodic vacuum arc (FCVA).

The superior nanomechanical/tribological properties of FCVA-deposited a-C films have been widely-reported; however, most studies have examined relatively thick (tens of nanometers) a-C films, while current demands require much thinner films of thickness in the range of 1-4 nm. FCVA-deposited a-C films overcoats are desirable protective overcoats for HDDs provided they can maintain their demonstrated high quality even for thickness as low as 1 nm. In this dissertation, an in-depth study of the structure of FCVA-deposited a-C films deposited on silicon was carried out using high-resolution transmission electron microscopy (HRTEM) and analytical electron energy loss spectroscopy (EELS). Both low- and high (core)-loss EELS spectra of Si and C were analyzed to determine the elemental content and through-thickness structure of ~20-nm-thick a-C films. Calculations of atomic carbon hybridization based on EELS spectra were used to track the film structure evolution. The average content of carbon hybridization in the top few nanometers of the a-C film, determined from EELS analysis, was found to be ~50%, much less than 73% of the bulk film. This multilayer structure was also validated by X-ray photoelectron spectroscopy (XPS). Results indicate that the minimum thickness of a-C films deposited by the FCVA method under conditions of optimum substrate bias (–100 V) should be equal to 3–3.5 nm, which is the total thickness of the buffer and surface layers.

1

The effects of other important FCVA process parameters on film growth were also investigated to explore the prospect of further decreasing the *a*-C film thickness. The incidence angle effect of energetic C^+ ions bombarding onto the growing film surface was studied in terms of the deposition rate, topography, and film structure. Cross-section TEM measurements combined with Monte Carlo (T-DYN) simulations revealed that the deposition yield (rate) is independent of the ion fluence but varies with the incidence angle according to a relationship derived from sputtering theory. XPS and atomic force microscopy (AFM) studies were also performed to examine carbon hybridization and film topography. The optimum incidence angle for FCVA deposition was found equal to 45°.

A relatively new technology that shows potential for further breakthroughs in magnetic recording is heat-assisted magnetic recording (HAMR). This technology utilizes a tightly focused laser beam to heat and temporarily reduce the coercivity of magnetic nanodomains below that of the magnetic field applied by the magnetic head. Impulsive laser heating (typically <1 ns) raises the temperature in the magnetic medium above its Curie temperature, i.e., the temperature above which the coercivity of the magnetic medium decreases significantly, thus enabling rapid data encoding by the magnetic field of the head. Among all other issues raised by this new technology, the thermal stability of the carbon overcoat of HAMR disks is of great concern. To address this concern, the stability of CVD- and FCVA-deposited carbon overcoats d by exposing them laser heating of different power. FCVA-deposited *a*-C films demonstrated higher stability than CVD-deposited *a*-C:H films, suggesting that hydrogen in the CVD-deposited films diffused at relatively lower temperatures before the commencement of structural changes in the carbon film. The thermal stability of the FCVA-deposited *a*-C films also showed a decreasing trend with decreasing film thickness.

The thermal stability of *a*-C:H films synthesized by plasma-enhanced CVD (PECVD) was also studied by rapid thermal annealing (RTA) experiments, to accurately estimate the critical temperature for *a*-C:H film degradation. X-ray reflectivity (XRR) and XPS measurements did not reveal any discernible changes in the film thickness and the sp^3 content due to RTA, indicating that oxidization and graphitization of the *a*-C:H films was either secondary or negligible during RTA. However, Raman spectra showed significant changes with annealing temperature increasing above 450 ^{o}C. Hydrogen depletion, the increase of the sp^2 cluster size, and the enhancement of carbon network ordering are the most likely factors affecting the structural stability of the *a*-C:H films. The obtained results suggest that the structural stability of *a*-C:H films deposited on current hard disks by PECVD can be preserved, provided they are not heated to temperatures above ~400 °C during the read/write operation process of HAMR HDDs.

In addition to the above experimental studies, molecular dynamics simulations were also performed to study the growth mechanism of *a*-C film due to an atom-by-atom deposition process, which is physically close to the real FCVA deposition process. Using the second-generation reactive empirical bond order (REBO) potential, *a*-C films with different structures were simulated by varying the carbon atom incident energy in the range of 1-120 eV. Atomic hybridization and ring connectivity were used to study the film microstructure. A multi-layer film structure consisting of an intermixing layer, bulk film, and surface layer was observed for relatively high carbon atom deposition energy, in agreement with the subplantation model. The highest film density (3.3 g/cm^3) and sp^3 fraction (~43%) and best intermediate-range order were obtained for ~80 eV incident energy, which is in good agreement with experimental findings.

Table of content

i

List of Figures

List of Tables

Chapter 1
Introduction

Carbon is probably one of the most complicated and versatile materials in nature. It exists in both crystalline and amorphous forms, exhibiting various mechanical, tribological, chemical, and electrical properties. Amorphous carbon (*a*-C) films of a wide range of thickness can be deposited by different methods on various substrates, mainly to reduce friction and wear and provide protection against corrosion.

a-C films are widely used as protective overcoats mainly due to their high hardness and good wear resistance [Robertson, 2002; Grill, 1999; Hauert, 2004]. The structure of *a*-C films is characterized by two types of atomic carbon bonding: graphite-like and diamond-like (DLC), characterized by sp^2 and sp^3 hybridizations, respectively. The outermost s and p orbitals of carbon atoms form π and σ bonds in sp^2 hybridizations and only σ bonds in sp^3 hybridizations. The π-bond existing only in sp^2 hybridizations is weaker than the σ-bond. It is well known that σ bonds influence the mechanical properties, while π bonds are mainly responsible for the electrical and optical properties [Robertson, 2002; Diaz et al., 1996]. The high hardness of *a*-C films is closely related to the sp^3 content, with higher sp^3 contents usually correlating with better film protection [McKenzie, 1996; Monteiro, 2001].

An application in which *a*-C films are of paramount importance to the device reliability and performance is hard-disk drives (HDDs). In HDDs, information is stored in the magnetic medium of a hard disk by the magnetic field applied by a transducer embedded in the trailing edge of the flying magnetic head. The structure of modern HDDs is illustrated as figure 1.1. The disk has a multi-layered structure. On top of the magnetic layer, an ultrathin *a*-C film is coated for protection against impact, wear, and corrosion, which is critical to the longevity of HDDs [Kryder, et al., 2008; Yasui et al., 2009]. The outmost lubricant layer is designed to further reduce friction at the hard-disk interface (HDI) whenever intermittent contact between the flying head with the rotating disk is encountered.

High demands for high-capacity, low-cost HDDs have led to the significant increase of the magnetic recording density. As shown in figure 1.2, over the last 30 years the areal density increased more than 10,000 times and is expected to continue to grow, but at slower rate due to challenging technical difficulties [Bandic and Victora, 2008]. The fastest increase in areal density occurred in the 1990s, principally due to technique breakthroughs, including the invention of the thin-film head and the giant magnetoresistance head, improvements in sputtered thin-film media, advancements in digital recording channels, and the decrease of the magnetic spacing.

Magnetic spacing is the distance between the magnetic head and the media. According to Wallace's law, the strength of a magnetic signal decays exponentially with distance. To further increase the storage density, the distance between the read/write transducer of the magnetic head and the magnetic medium of the hard disk must be reduced below 6.5 nm [Yasui et al., 2009].

For such small spacing, the thickness of the carbon overcoat and lubricant layer as well as the physical distance between the head and the disk must be greatly reduced [Wood et al., 2002; Anders et al., 2001]. To achieve this goal, the thickness of the carbon overcoat must decrease from typically ~4 nm in current HDDs to ~1 nm. At the same time, this ultrathin a-C film must be continuous and maintain its mechanical and tribological features to serve as a protective layer.

Various deposition techniques can be used to grow a-C films. The most common methods for synthesizing ultrathin a-C films are filtered cathodic vacuum arc (FCVA) [Monteiro, 2001; Brown, 1998], pulsed laser deposition [Monteiro, 2001; Voevodin and Donley, 1996], chemical vapor deposition [Monteiro, 2001; Fung et al., 2000; Leng et al., 2000], and sputtering [Wan and Komvopoulos, 2006]. Depending on the type of deposition process and ranges of controlling process parameters (e.g., plasma power, substrate bias voltage, and ion fluence), a-C films possessing different microstructures and mechanical properties can be deposited on various substrates [Robertson, 2002; Grill, 1999; Hauert, 2004; Brown, 1998]. Among the previous methods, FCVA is more advantageous because it is a cost-effective technique for depositing ultrathin, hydrogen-free a-C films with high sp^3 contents, also known as tetrahedral a-C films [Robertson, 2002]. Because a-C films demonstrate a hardness of ~80 GPa and an elastic modulus in the range of 710–805 GPa, they are ideal protective overcoats for mechanical wear [Espinosa et al., 2006; Grierson et al., 2010]. The concern is, whether a-C films can demonstrate sifficiently high hardness and good wear resistance at such small thicknesses. To answer this question, the detailed film structure needs to be studied.

FCVA is a plasma-based technology for film fabrication. In FCVA, the plasma energy can be controlled by adjusting the pulsed substrate biasing voltage. Because of the nature of energetic ion deposition, the film exhibits a layered structure, which can be explained by the subplantation model. In Chapter 3, high-resolution transmission electron microscopy and spatial resolution scanning transmission electron microscopy with electron-energy loss spectroscopy to were used to perform in-depth studies of the structure of FCVA-deposited a-C films and determine the minimum film thickness for FCVA optimum deposition conditions.

To control the film thickness, several processing parameters can be adjusted, including deposition time, arc discharge current, and incidence angle. Since FCVA-deposited films possess a layered structure, shortening the deposition time would only reduce the total film thickness and may result in low-sp^3 intermixing layer and sp^2-rich surface layer of constant thickness. The arc discharge current has a minimum requirement to ignite the plasma and arcing cannot be stabilized within a very short time. Thus, shortening the deposition time and/or reducing the arc discharge current are not effective solutions. The only other key parameter that can be varied is the incidence angle. By changing the incidence angle a sputtering effect is introduced in the film growth process, which is helpful to produce ultrathin film. Due to the competing effect of film deposition and film sputtering, the quality of the a-C film would also be affected. An in-depth examination of the incidence angle effect of energetic carbon ions on the deposition rate, topography, and structure of ultrathin a-C films deposited by FCVA is presented in Chapter 4.

Intense competition among traditional and contemporary HDD technologies, such as solid-state drives, has further increased the demand for higher capacity and lower cost. An effective means of increasing the magnetic storage density is to decrease the magnetic grain size and closely pack the magnetic grains. However, if the ferromagnetic grains become too small,

thermal fluctuations would cause a random change in the magnetic direction of the grain. In this case, the information stored in the magnetic materials will be lost. Therefore, if the magnetic grain size reduction reaches the limit determined by the thermal-stability zone (figure 1.2), further increasing the storage density will be inhibited by the superparamagnetic limit. A promising magnetic recording technology for overcoming this major obstacle is heat-assisted magnetic recording (HAMR).

HAMR uses a laser-optical system integrated into the magnetic head to locally heat a fine-grained, high-magnetic-anisotropy energy density material above its Curie temperature, to store single bits in very small areas without being limited by the superparamagentic effect. Figure 1.3(a) shows the desired coercivity change versus temperature. At ambient/room temperature, the coercivity is very high, implying stable magnetic grains. During the write process, information is stored in the media by adjusting the orientation of the magnetic grains. The integrated laser (figure 1.3(b)) is turned on to locally heat the magnetic grain to a temperature above the Curie temperature, and reduce the coercivity below a critical level so that the orientation of the magnetic grains can be easily controlled by the magnetic field applied by the read/write transducer on the magnetic head. The mechanism during the write process is illustrated in figure 1.3(a).

An important issue raised by the new HAMR technology is the thermal stability of carbon overcoats. For the most promising HAMR magnetic material (i.e., highly anisotropic $L1_0$ phase FePt), the Curie temperature is ~750 K [Kryder et al., 2008]. This means that the temperature in the carbon overcoat should be raised to least 750 K within 1 ns [Challener et al., 2009] under write conditions. In view of the elevated temperature, intensive heating, and rapid cooling, the carbon overcoat may undergo graphitization ($sp^3 \rightarrow sp^2$), oxidation, loss of thickness, and possibly structure change. These changes may negatively impact the mechanical and tribological properties of the overcoat, leading to the depletion of the overcoat protection. A study aimed at examining the effect of laser heating on the overcoat thermal stability is presented in Chapter 5. Results are shown from experiments performed with a free-standing laser that repetitively heated different a-C films at different power levels.

Laser heating experiments can resemble the real HAMR working condition better than other thermal annealing experiments on the time scale. However, because of the very small laser spot (<100 nm in diameter when using a near-field transducer) and short heating time in HAMR, it is difficult, if not impossible, to directly and accurately measure the temperature rise in the carbon film due to laser heating. In the HAMR application, accurate estimation of the critical temperature for a-C film degradation is critical to the success of HAMR, because it determines the maximum laser power for a given magnetic medium. Thus, rapid thermal annealing (RTA) was used to study the structure stability of a-C film in Chapter 6. Although in high-temperature environments, tetrahedral a-C films perform better than carbon films with lower sp^3 contents [Anders et al., 1997; Wang and Komvopoulos, 2011], the FCVA deposition equipment is not in good compatibility with the disk manufacturing line because of its S-duct filter configuration. Therefore, RTA was used to examine the thermal stability of ultrathin a-C:H films deposited by PECVD, which are used as protective overcoats in some current HDDs, to provide a limit for the Curie temperature of magnetic materials used in HAMR.

Carbon film characterization becomes increasingly difficult with decreasing film thickness, especially when the film thickness is on the order of a few nanometers. For example, the XPS measurement usually requires a film thickness of >10 nm, otherwise the intensity of the C1s peak would be low and it would take a very long time to acquire a stronger signal. This is also true for Raman spectroscopy. When the film thickness is <3 nm, the Raman signal-to-noise ratio would be very low, making it difficult to fit/analyze the curve.

The main objectives of this dissertation are to investigate the structure properties of ultrathin a-C films used in HDDs, and evaluate their potential to serve as protective overcoats in HAMR HDDs. The dissertation is organized as following:

Chapter 1 provides a background and the motivation of the experimental and MD simulation studies. In addition, the application of ultrathin a-C films as protective overcoats in HDDs is discussed in the context of high demands for high-capacity HDDs, which require extremely thin a-C overcoats possessing good mechanical and tribological properties, continuity, and thermal stability. The latter is of high importance in HAMR HDDs where localized laser heating can degrade the overcoat protective properties.

A major part of this dissertation is devoted to experimental studies of a-C films, including the structure of a-C films deposited with the FCVA method, the effect of process parameters (incidence angle) during FCVA deposition on the film structure, and the thermal stability of ultrathin a-C films. General information about carbon film deposition methods and common characterization methods are presented in Chapter 2.

a-C films deposited by FCVA exhibit superior mechanical properties and wear resistance than a-C films deposited by other methods, such as sputtering, electron-beam evaporation, and chemical vapor deposition. Because of continuously increasing demands for the development of protective ultrathin a-C films in various leading technologies, such as information storage and optoelectronics, knowledge of the structure of such films is of high technological and scientific importance. In Chapter 3, ~20-nm-thick a-C films deposited on Si(100) by the FCVA method are examined by high-resolution transmission electron microscopy (HRTEM), electron energy loss spectroscopy (EELS), and X-ray photoelectron spectroscopy (XPS). Results of the plasmon excitation energy shift and the through-thickness elemental concentration show the formation of a multilayered a-C film structure consisting of an interface layer consisting of C, Si, and, possibly, SiC, a buffer layer with continuously increasing sp^3 fraction, a relatively thicker layer (bulk film) of constant sp^3 content, and an ultrathin surface layer rich in sp^2 hybridization. A detailed study of the C K-edge spectrum suggests that the buffer layer between the interface layer and the bulk film is due to partial backscattering of the C^+ ions interacting with the heavy atoms of the silicon substrate. The obtained HRTEM and EELS results provide insight into the minimum thickness of a-C films synthesized under optimum substrate bias FCVA conditions.

To further decrease the thickness of a-C films synthesized under optimum substrate bias FCVA conditions, the effect of the incidence angle of energetic carbon ions on the thickness, topography, and structure of ultrathin a-C films is examined in Chapter 4. The thickness of a-C films deposited at different incidence angles was investigated in the light of Monte Carlo simulations, and the calculated depth profiles were compared to those obtained from HRTEM. The topography and structure of the a-C films were studied by AFM and XPS, respectively. The

film thickness decreased with the increase of the incidence angle, while the surface roughness increased and the sp^3 content significantly decreased with the increase of the incidence angle above 45°, measured from the surface normal. TEM, AFM, and XPS results indicate that the smoothest and thinnest a-C films with the highest content of sp^3 carbon bonding were produced for an incidence angle of 45°. The findings of the work presented in Chapter 4 have direct implications in ultrahigh-density magnetic recording, where ultrathin and smooth a-C films with high sp^3 contents are of critical importance.

Heat-assisted magnetic recording (HAMR) uses a laser-optical system integrated into the magnetic head to heat locally a fine-grained, high-magnetic-anisotropy energy density material above its Curie temperature, to store single bits in very small areas without being limited by the superparamagnetic effect. However, localized laser heating may affect the thermal stability of the carbon overcoat on the hard disk. The effect of repetitive laser heating on the overcoat thermal stability is examined in Chapter 5. Ultrathin a-C films of similar thickness (~3.6 nm) synthesized by FCVA and CVD were subjected to repetitive laser heating at different power levels. Carbon hybridization and surface roughness of the a-C films were examined by Raman spectroscopy and AFM, respectively. For the laser power range examined (150–300 mW), a-C films produced by the FCVA technique demonstrated greater thermal stability than CVD films of similar thickness. To investigate the possibility of further reducing the magnetic spacing, thinner (~0.9 nm) a-C films deposited by the FCVA method were subjected to the same laser heating conditions. Although the thermal stability of the FCVA-synthesized a-C films exhibited thickness dependence, even the thinner (~0.9 nm thick) FCVA film demonstrated higher thermal performance than the much thicker (~3.6 nm) CVD film. The results presented in Chapter 5 illustrate the high potential of FCVA as a coating method for HAMR.

Although FCVA is an attractive method for synthesizing ultrathin a-C films with high sp^3 content, the integration of FCVA to the HDD manufacturing line is not an easy task because of the irregular S-duct filtering system of FCVA. Currently the most popular way to synthesis carbon overcoats in HDD industry is CVD. In Chapter 6, rapid thermal annealing (RTA) was used to examine the thermal stability of ultrathin a-C:H films deposited by PECVD. Structural changes in the a-C:H films induced by RTA were studied by XPS, Raman spectroscopy, XRR, and conductive AFM. It is shown that the films exhibit thermal stability up to a critical temperature in the range of 400–450 °C. Heating above this critical temperature, resulted in the depletion of hydrogen and the enhancement of sp^2 clustering. The determined critical temperature represents an upper bound of laser heating in HAMR hard-disk drives and provides a limit for the Curie temperature of magnetic materials used in HAMR.

For ultrathin a-C films of thickness <5 nm, molecular dynamics (MD) simulations provide better insight into the film growth and structure. By choosing an appropriate force field, MD analysis can yield predictions for the film structure and properties. This is invaluable information that is complementary to the experimental findings. In Chapter 7, molecular dynamics simulations were performed to study the growth mechanism and the structure of a-C films using the second-generation REBO potential. By changing the carbon atom incident energy in the range of 1-120 eV, a-C films with different structures were simulated. The film density and film residual stress were calculated after the system reached equilibrium. Short- and intermediate-range carbon atom ordering was examined in terms of atomic hybridization and ring connectivity, respectively. A multi-layer film structure, including intermixing layer, bulk film, and surface

layer, was observed for relatively high deposition energy, in accord with the subplantation model. Changes in film structure with the deposition energy elucidated by MD simulation results are in good agreement with experimental findings.

Main findings of this dissertation are summarized in Chapter 8.
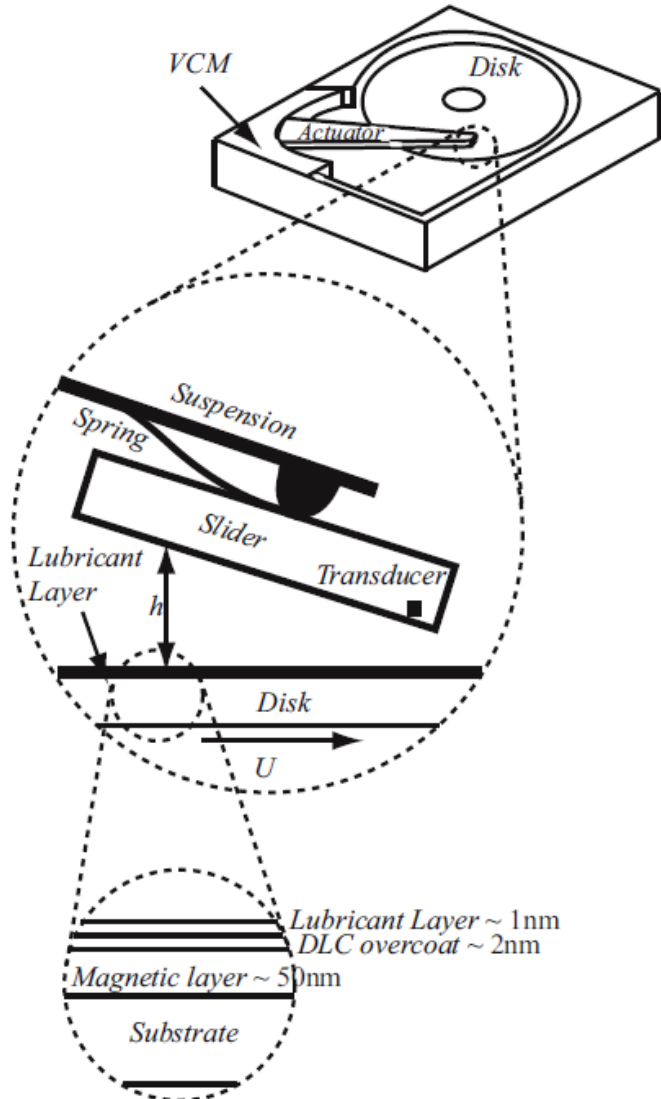
Figure 1. 1 Structure of modern HDDs.
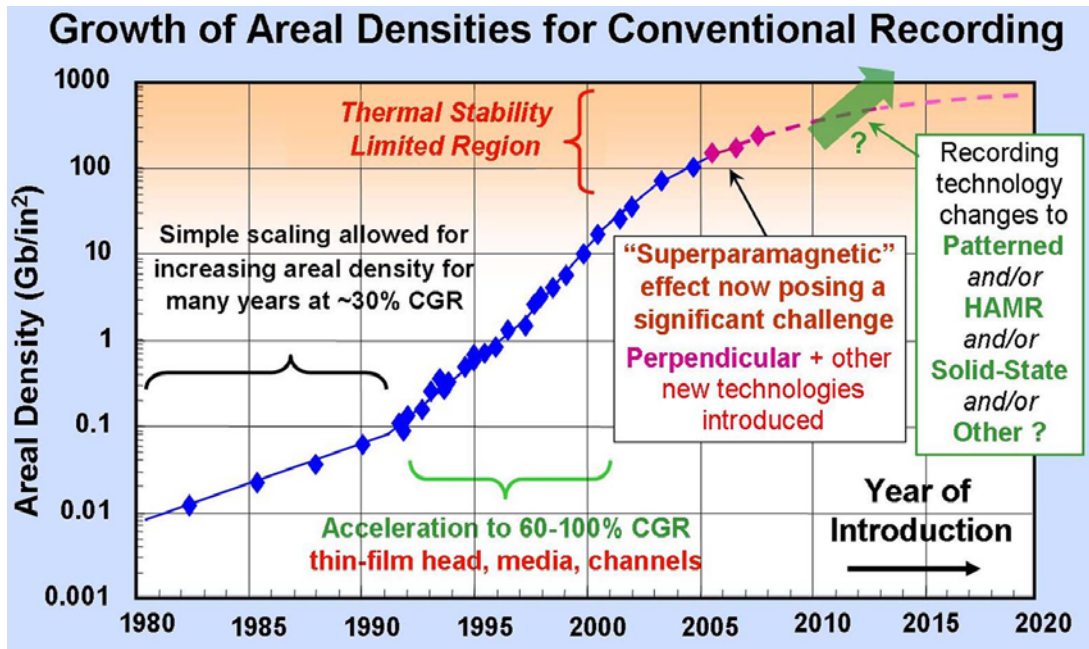
Figure 1. 2 Bit areal density progress in magnetic hard disk drives [Bandic and Victora, 2008].
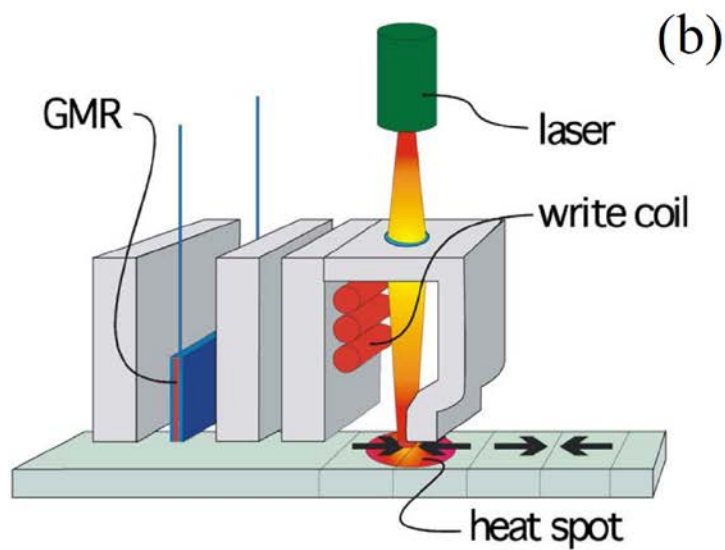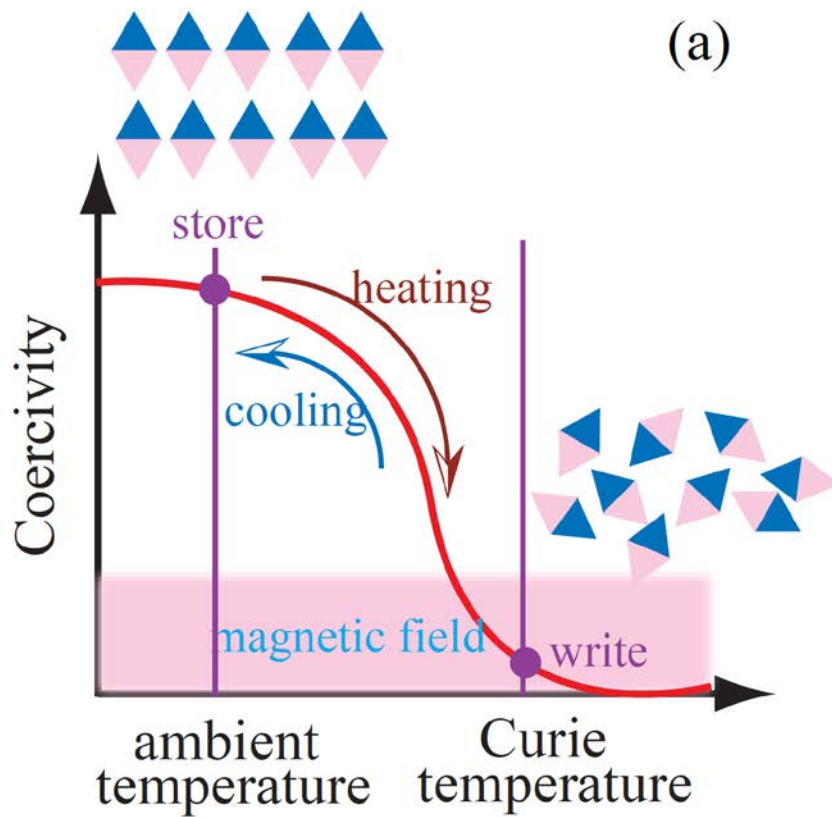
Figure 1. 3 (a) Diagram of coercivity change due to temperature rise; (b) Diagram of read/write magnetic head with near-field optics [Dobisz et al., 2008].

Chapter 2
Experimental procedures

2.1 Introduction

As we stated in chapter 1, the major part of this dissertation will focus on experimental investigations on ultrathin amorphous carbon films. Some widely-used film deposition techniques, such as filtered cathodic vacuum arc (FCVA) and plasma-enhanced chemical vapor deposition (PECVD), and those film characterization methods, such as atomic force microscopy (AFM), X-ray photoelectron spectroscopy (XPS), Raman spectroscopy (RS) and transmission electron microscopy (TEM), are employed in different parts of this dissertation. Thus, we would like to introduce the operation principles of these experimental techniques in general in this chapter.

2.2 Carbon film deposition techniques

Amorphous carbon film has been produced by various deposition techniques, of which can be divided into two catalogues by the deposition mechanisms: physical vapor deposition (PVD) and chemical vapor deposition (CVD). In PVD, films are formed by atoms/ions directly transported from source to the substrate through gas phase. In CVD, films are formed by chemical reaction on the surface of substrate.

The microstructure and properties of carbon films strongly depend on the deposition methods and process parameters. In this dissertation, we will focus on the FCVA- and CVD-deposited a-C film. Other deposition method will be briefly introduced.

2.2.1 Filtered cathodic vacuum arc (FCVA)

Filtered cathodic vacuum arc is a low-temperature thin film deposition technique, in which a high power electric arc discharged at the target material, blasts away some into highly ionized vapor to be deposited onto the substrate. By applying a pulsed substrate bias, the energy of the ions can be manipulated to change the film properties.

Figure 2.1 shows the schematics of the FCVA system. At the high-purity (99.999%) graphite cathode, the arc current is concentrated at a small number of discrete sites called cathode spots with a size in the range of 1-10 microns. The current density at the cathode spot is very high, on the order of 10^6-10^8 A/cm^2 [Brown, 1998]. The carbon plasma is formed by an explosive emission process. The plasma generated at the cathode sites is a mixture of microdroplets, macroparticles and carbon ions. When guided to the sample surface, only carbon ions can follow the magnetic field lines and go through the S-duct magnetic filter. Those microdroplets and macroparticles would hit the chamber walls and get out of the plasma. Thus, the plasma ionization increases from about 30% near the cathode to nearly 100% at the filter exit

[Robertson, 2002]. This pure carbon ions plasma is then condensed onto the substrate to produce *a*-C film.

The advantage of the FCVA method is that it produces highly ionized plasma with an energetic species. With optimum substrate bias to modify the ions energy to about 100 eV, the hydrogen-free *a*-C film can have the sp^3 fraction as high as 87.5% [Xu et al., 1996; Pharr et al., 1996, Anders, 2002]. As the mechanical properties of *a*-C film is highly related to its sp^3 fraction, these films are featured with high hardness, good wear-resistance and corrosion-resistance.

Our in-house cathodic vacuum arc system is operated in direct current mode, which yields higher deposition rates than pulsed arc mode. The details of the system configuration can be found elsewhere [Zhang and Komvopoulos, 2008].

2.2.2 Plasma-enhanced chemical vapor deposition (PECVD)

PECVD is among the most popular deposition methods for carbon overcoats [Wei, Q. and Narayan, J., 2000]. The reactor consists of two electrodes of different area. In some cases, magnetrons and/or microwaves are used for plasma generation to enhance the chemical reaction. Generally speaking, the principle of the PECVD process is to introduce a carbon containing gas at a pressure allowing a glow discharge by applying a bias voltage on the substrate holder. This glow discharge will activate the hydrocarbon precursor and produce radicals and atoms, which deposit and react on the surface of the substrate to form the coating.

The carbon containing gases, or precursor gases, are chosen based on the requirements of the hydrogen content in the film. Of course the ease to manage the gas and safety issues are also considerations for the choice of precursor gases. The most popular gases include CH4, C2H2, C2H4, etc. Due to its nature of the hydrocarbon species deposition, the resulted film contains hydrogen up to 50% [Bhushan et al., 1992; Grill et al.,1990].

2.2.3 Other techniques

Other popular deposition techniques for a-C films include Sputtering, Ion beam deposition, pulsed-laser deposition, etc.

In sputtering deposition [Savvides and Window, 1985], the carbon coating is deposited by the sputtering of graphite target with the bombardment of Ar^+ ion plasma. The positive ions from the plasma strike the graphite target to knock out the carbon atoms by momentum transfer. This method is not suitable for ultrathin carbon films with a thickness less than 5 nm, otherwise the film will not be continuous.

In ion beam deposition [Aisenberg and Chabot, 1971], the carbon coating is deposited from an accelerated carbon ion beam. A negative potential is applied to the substrate to attract the positive ions. For insulating films, an AC or RF potential is applied to the substrate to attract the electrons to cancel the surface charge.

In pulsed-laser deposition, lasers with various wavelengths have been used to ablate the graphite target to produce carbon coatings [Krishnaswamy et al., 1989]. Due to the non-

equilibrium process and the high kinetic energy of the laser plasma, the carbon film produced by this method processes high quality, in terms of high sp^3 fraction and high hardness.

2.3 Film characterization techniques

For surface topography, AFM is used to measure the roughness. XPS and RS are used to detect the microstructure evolution during different treatments. TEM with high resolution is used to accurately calibration the film thickness. STEM-EELS can detect the elementary information in the film.

2.3.1 Atomic force microscope (AFM)

Atomic force microscopy (AFM) is one kind of scanning probe microscopy (SPM). Since its invention in 1986 by Gerd Binning and Heinrich Rohrer, AFM has been widely used to examine surface morphology and properties.

In the AFM, a sharp tip is placed in a compliant cantilever. The general concept is using a force to image a surface due to the interatomic interaction between the very sharp tip and the sample. The force is proportional to the vertical deflection of the cantilever and typically the deflection of the cantilever is measured using a laser spot reflected from the top surface of the cantilever into an array of photodiodes. The schematic of basic AFM operation, real micro-cantilever and components are shown in figure 2.2.

AFM (Dimension 3100, Digital Instrument) has been used to measure the sample topography and surface roughness in this dissertation. AFM imaging was usually performed with Si tips of nominal radius of curvature less than 10 nm at a scanning speed of 2 ~ 4 µm/s in the tapping mode. All of the AFM samples were cleaned with acetone before scanning. For statistical analysis, at least three different surface locations on the sample were imaged with the AFM, and the obtained roughness data were assumed to follow normal distributions.

2.3.2 X-ray photon spectroscopy (XPS)

X-ray photon spectroscopy (XPS) is a widely-used non-destructive surface analytical technique based on the photoelectric effect. The characteristic binding energy of each atom in the surface is equal to the ionization energy of the core electron. When an X-ray beam is directed to the sample surface, the energy of the X-ray photon will be adsorbed by the core electron of an atom in the surface. If the photon energy, h, is large enough, the core electron will have enough energy to escape from the atom and emit out of the surface. The emitted electron with the kinetic energy of E_k is then referred to as the photoelectron. The binding energy of the core electron is given by the Ernest Rutherford (1914) relationship:

$$E_b = hv - E_k - \Phi \qquad (2.1)$$

Where E_b is the binding energy of the electron, h is the X-ray photon energy; E_k is the kinetic energy of photoelectron, which can be measured by the energy analyzer; and Φ is the work function induced by the analyzer.

The PHI 5400 X-ray photoelectron spectroscopy (XPS) system (Physical Electronics, Chanhassen, MN) is used in most parts in this dissertation except for Chapter 6. This XPS equipment located in Molecular Foundry, Lawrence Berkeley National Laboratory (LBNL), has a spatial resolution of 0.5 mm and energy resolution of 0.7 eV. It works with non-monochromatic Al-Kα radiation of 1486.6 eV energy and work function of 5.7 eV, under a vacuum pressure of less than 2×10^{-8} Torr. This XPS system can perform elemental and chemical state analysis of the first few nanometers of the surface with ~1 atomic percent sensitivity.

To determine the sp^3 film content, multiplex narrow-scan spectra of the C1s core-level peak were acquired with pass energy of 37.75 eV, using a channel width of 0.1 eV/step and acquisition time fixed at 50 ms/step. Spectra were collected after 50 sweeps in the binding energy range of 280–292 eV. The film samples were fixed to the XPS specimen holder by conductive clips to prevent surface charging.

The C1s peak was fitted with five Gaussian distributions after Shirley background subtraction. The C1s-1, C1s-2, and C1s-3 peaks were corresponding to sp^1, sp^2, and sp^3 C-C hybridizations, respectively, and C1s-4 and C1s-5 representing high-order C–O and C=O bonds, respectively. The binding energy of each carbon chemical state was assigned the peak energy of the corresponding Gaussian distribution. The sp^2 and sp^3 fractions were defined as the C1s-2 and C1s-3 distribution areas, respectively, divided by the sum of the C1s-2 and C1s-3 distribution areas.

2.3.3 Raman spectroscopy (RS)

Raman spectroscopy (RS) is a non-destructive spectroscopic technique used to observe vibrational, rotational and other low-frequency modes in a system [Smith and Dent, 2005]. It relies on inelastic scattering of monochromatic light, usually from a laser source. Inelastic scattering means that the frequency of photons in monochromatic light changes upon interaction with a sample. Photons of the laser source are absorbed by the sample and then reemitted. Frequency of the reemitted photons is shifted up or down in comparison with original monochromatic frequency, which is called the Stokes and Anti-Stokes Raman scattering. These shifts provide information about the vibrational modes in the system. The Raman shift is defined by:

$$\Delta\omega = \frac{1}{\lambda_0} - \frac{1}{\lambda_1} \tag{2.2}$$

Where $\Delta\omega$ is the Raman shift in wavenumber (cm^{-1}), λ_0 is the excitation wavelength, and λ_1 is the reemitted photons wavelength.

For characterizing carbon system, Raman spectroscopy is a standard characterization technique used to determine the structure and composition of carbon films. In visible Raman (usually with 514 nm wavelength laser source), all carbons show common features in the 800-2000 cm^{-1} region in the spectra: the D peak at around 1360 cm^{-1} and the G peak at around 1560 cm^{-1}. Both of the G and D peaks are due to sp^2 sites. The difference is that, the G peak is due to the E$_{2g}$ bond stretching of all pairs of sp^2 atoms in both rings and chains, while the D peak is due

to the A_{1g} breathing modes of sp^2 atoms only in rings. From the shape and intensity of these two peaks, the disorder of carbon networks can be evaluated.

2.3.4 Transmission electron microscopy (TEM)

2.3.4.1 Sample preparation

In this work, cross-section TEM samples are prepared by mechanical grinding and dimpling. Film samples are cleaned with Acetone and Mecelone and then cleaved into two halves. M-bond 610 epoxy was used to glue the cleaved sample face-to-face. After curing at 160˚C for 1 h, dummy Si(100) was glued to both side of the sandwiched film samples to increase the sample thickness to > 3 mm. The samples were then sectioned in 500-µm-thick slices with a diamond blade and saw-cut to 3-mm-diamter disks. Finally, the disks were ground down to a thickness of 5-8 µm at the center by double-side dimpling and then ion milled from the top and the bottom with Ar+ ion guns operated at 5 kV and 5 mA (Fischione Instruments, Export, PA) to produce a through-thickness hole across the sample/epoxy/sample interface. 10 mins Ar+ ion treatment with lower energy (2 kV and 2 mA) was used to further clean the sample. The sample preparation process is illustrated in figure 2.2.

2.3.4.2 High-resolution transmission electron microscopy (HRTEM)

Microscopy is a device that transfers information form the specimen to the image. HRTEM is an imaging mode of the TEM that allows the imaging a specimen at atomic resolution. The resolution δ is given approximately by

$$\delta \approx \frac{1.22\lambda}{\beta} \tag{2.3}$$

Where λ is the wavelength of the electron beam, β is the semi-angle of collection of the magnifying lens. The wavelength of electrons is related to their energy. For a 200 kV electron beam, its relativistic wavelength is about 2.51 pm, which is much smaller than the diameter of an atom.

Two microscopies have been used in this dissertation. Both of them are located in National Center for Electron Microscopy (NCEM) at LBNL. The 200 kV FEI monochromated F20 UT Tecnai is used in Chapter 3 to take HRTEM images and carry out EELS study. The spherical aberration C_s is 0.5 mm and the chromatic aberration C_c is 1.1 mm. With monochromator off, the information limit is 0.12 nm for HRTEM and spatial resolution is 0.14 nm for STEM. The Philips CM200/FEG is used in Chapter 4 to take HRTEM images. The spherical aberration C_s is 1.2 mm and the chromatic aberration C_c is 1.2 mm. Their images are shown in figure 2.4.

2.3.4.3 Electron energy-loss spectrometry (EELS)

When electrons enter a solid, they interact with the atoms through electrostatic (Coulomb) forces. As a result of these forces, some of the electrons are scattered; the direction of their momentum is changed and in some cases they transfer an appreciable amount of energy to the specimen. These interactions can be divided into two categories: elastic and inelastic.

Elastic scattering involves the interaction of an incident electron with an atomic nucleus. Because the nucleus mass is much larger than that of an electron, the energy exchange due to this interaction is very small and usually undetectable.

Inelastic scattering results from the interaction of an incident electron with electrons in the specimen. Due the similarity of the mass, the energy loss due to this interaction ranges from a few electron volts to hundreds of electron volts.

Electron energy-loss spectroscopy (EELS) measures the energy distribution of electrons that have come through the specimen. The EELS spectrum shows the number of electrons as a function of their decease in kinetic energy. These energy-loss events are highly related to the chemistry and the electronic structure of the specimen atoms, from which the bonding structure, the free-electron density and the specimen thickness can be analyzed. Take carbon for example, the carbon atom has hybridized s and p orbitals. Graphite contains sp^2 bonds in the basal plane with Van der Walls bonding between the planes. Differently, diamond has four sp^3 covalent bonds, which forms a tetrahedral structure. The strong peak K edge at 284 eV identifies the empty π* states into which the K shell electrons are transferred in graphite, while the diamond K edge has no π* peak but shows a strong σ* peak at around 290 eV. Figure 2.5 shows the differences between the ELNES of the carbon-K edge from various forms of carbon. From these information, the hybridization structure of a-C films can be derived.
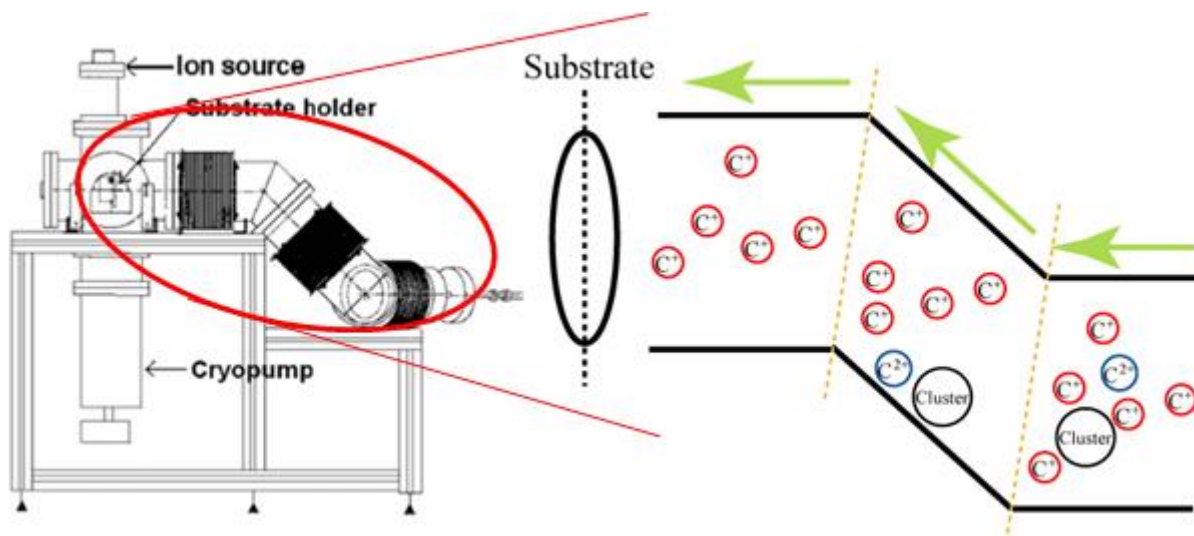
Figure 2. 1 Diagram of FCVA filtering mechanism
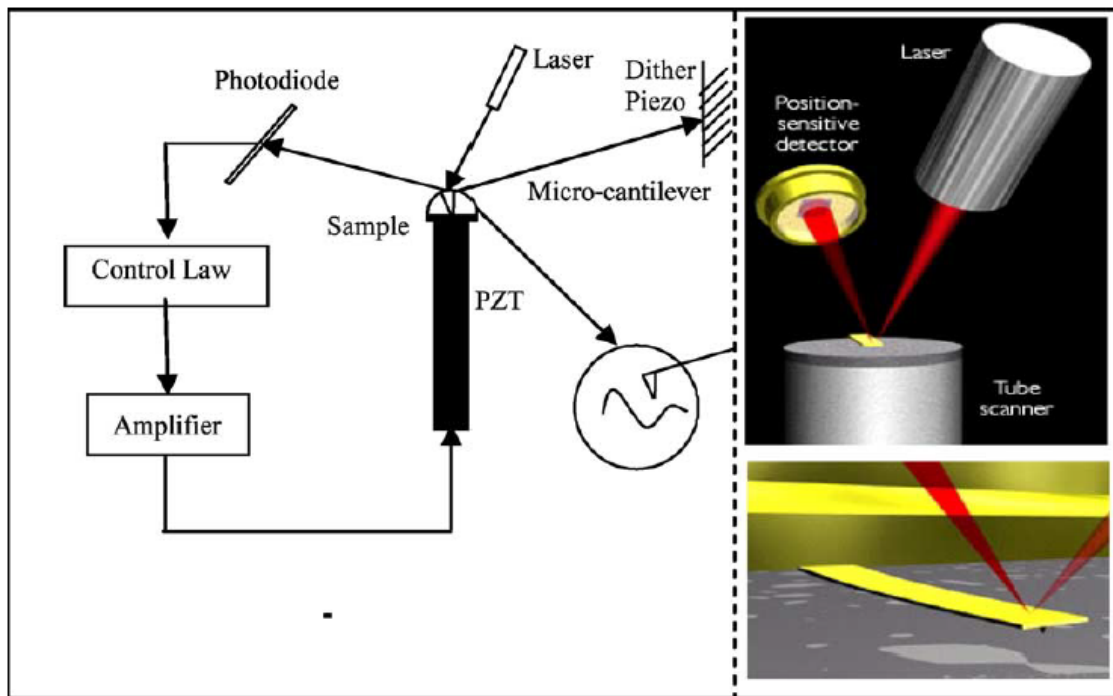
Figure 2. 2 Schematic of basic AFM operation (left), real micro-cantilever and components (right). [Jalili and Laxminarayana, 2004]

(1) Cleave into two pieces

(3) Attached dummy Si
to increase thickness

(1)

Sample

(2)

(3)

(2) Glue face to face

(4) Cut into slices

(6) grinding/polishing/
dimpling

(4)

(5)

(6)

~100 μm

(5) Disc saw

~5 μm

(7)

3 mm

(7) Ion milling create a hole
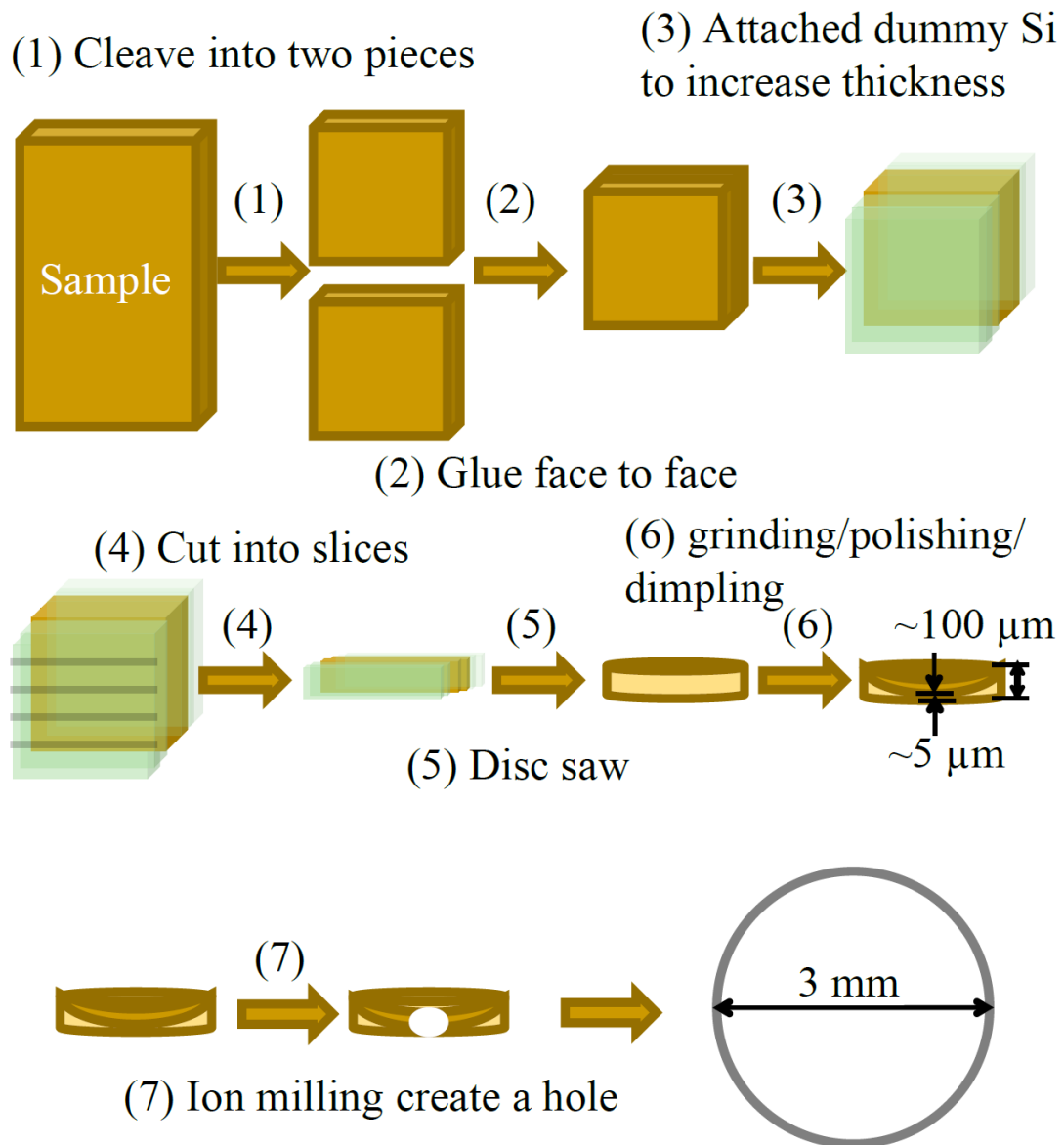
Figure 2. 3 Cross-section TEM sample preparation procedure.

<center>(a)   (b)</center>

Figure 2. 4 Images of the TEM system: (a) Philips CM2000; (b) Tecnai.
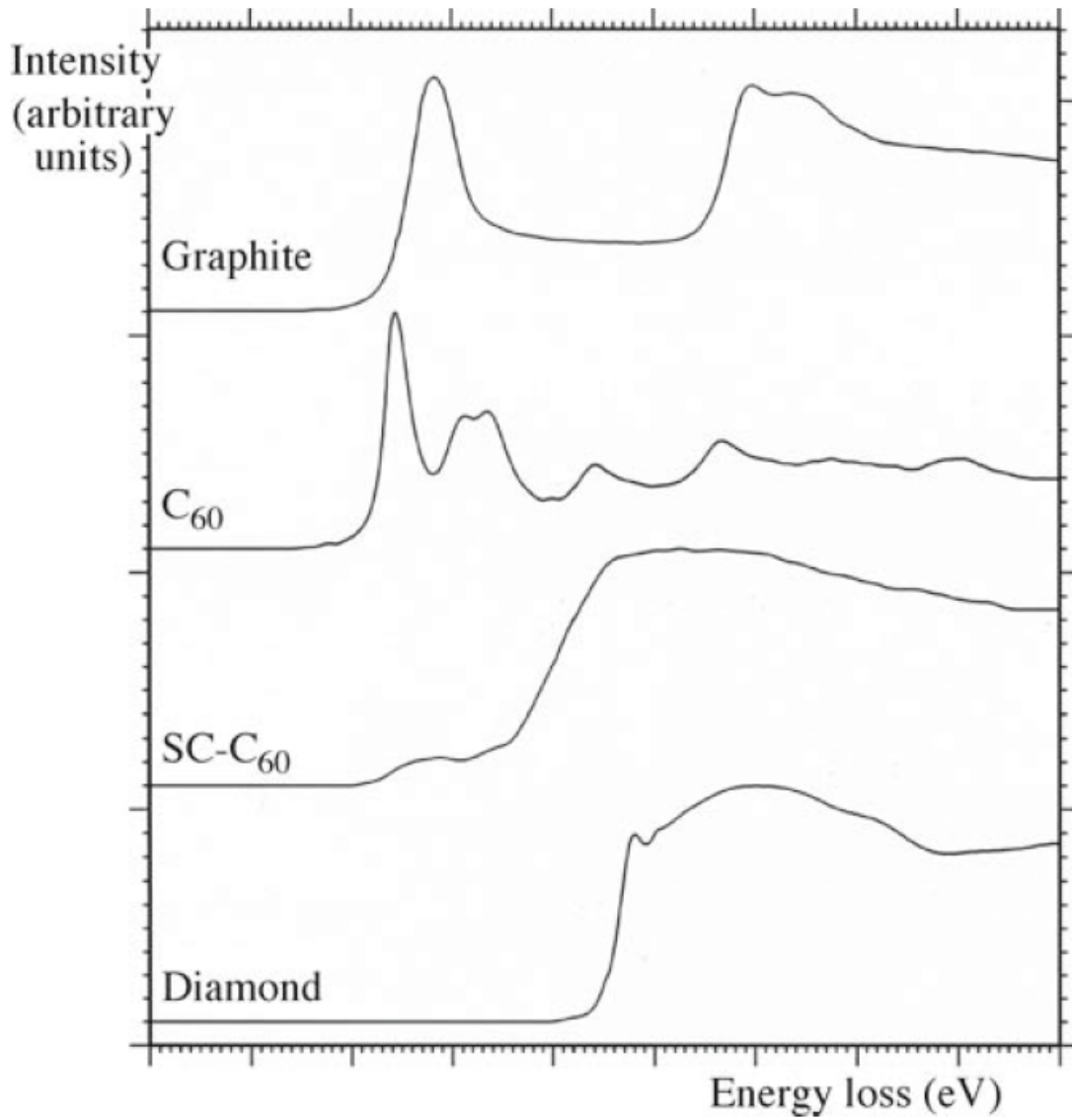
Figure 2. 5 Differences between the ELNES of the carbon-K edge from various forms of carbon. [Williams and Carter, 2009]

Chapter 3
The multilayered structure of ultrathin amorphous carbon films synthesized by filtered cathodic vacuum arc deposition

3.1 Introduction

Filtered cathodic vacuum arc (FCVA) is one of the most effective ultrathin-film deposition methods. Amorphous carbon (*a*-C) films synthesized by the FCVA method exhibit high purity, excellent uniformity, very small roughness, high hardness, low friction, and good wear and corrosion resistance.[Roberteson, 2002; Monteiro, 2001; Brown, 1998; Voevodin and Donley, 1996] The superior nanomechanical/tribological properties of these *a*-C films, demonstrated by nanoindentation and nanoscratching experiments, [Fung et al., 2000; Hauert, 2004; Erdemir and Donnet, 2006; Zhang and Komvopoulos, 2009] are mainly attributed to the high fraction of tetrahedral (sp^3) carbon atom hybridization. The structures of various types of carbon films have been extensively studied by X-ray photoelectron spectroscopy (XPS) and Raman spectroscopy. [Zhang and Komvopoulos, 2009; Diaz et al., 1996; Yasui et al., 2009; Zhu et al., 2008; Ferrari and Robertson, 2004; Ferrari and Robertson, 2000; Knight and White, 1989] However, because the information obtained by these methods is averaged over a depth of a few nanometers, XPS and Raman spectroscopy cannot provide information about the through-thickness structure of nanometer-thick *a*-C films. Although elemental depth profiles may be obtained with *in situ* high-energy Ar^+ plasma sputtering during XPS, it is difficult to accurately calibrate and control the sputtering rate of ultrathin films. In addition, the intense energetic Ar^+ ion bombardment during sputter etching may alter the film structure.[Oswald and Reiche, 2001; Poudel et al., 2012] Detailed structural analysis of ultrathin films requires cross-section transmission electron microscopy (TEM) samples and microanalysis techniques with a very high spatial resolution, such as electron energy loss spectroscopy (EELS).

Previous EELS studies of *a*-C films deposited on silicon by the FCVA method under different substrate bias conditions have revealed a layered film structure consisting of an interface layer, the bulk film, and a surface layer.[Zhu et al., 2008; Siegal et al., 2000; Davis et al., 1998; Davis et al., 1995; Riedo et al., 2000] According to the subplantation model, [Lifshitz et al., 1990] the interface layer is less dense than the bulk film and its formation is a result of partial backscattering of the C^+ ions impinging onto the heavy Si atoms, the bulk film is due to C^+ ion subplantation and is characterized by a high compressive stress, and the surface layer is dominated by trigonal (sp^2) carbon atom hybridization and is also less dense than the bulk film. The thickness of the interface and surface layers depends on the penetration depth of the C^+ ions, which is a function of the C^+ ion energy.[Siegal et al., 2000; Davis et al., 1998; Davis et al., 1995] Surface and interface layers of thickness equal to ~12 and ~3 nm have been reported for 55-nm-thick *a*-C films deposited on Si(100) by FCVA under plasma conditions of 90 eV C^+ ion energy [Siegal et al., 2000] However, significantly thinner surface layers of thickness between 0.4 ± 0.2 and 1.3 ± 0.3 nm have been observed in other studies for C^+ ion energy of 35 and 320 eV, respectively.[Davis et al., 1998; Davis et al., 1995]

The quality of FCVA-deposited a-C films strongly depends on the C^+ ion energy. Intensification of collision cascades between C^+ ions and substrate atoms with the increase of the C^+ ion energy yields localized high pressures that are conducive to sp^3 hybridization. However, high C^+ ion energy may also promote thermal relaxation, resulting in sp^3-to-sp^2 rehybridization. Because of these competing processes, there is an optimum C^+ ion energy (typically, ~120 eV) [Robertson, 2002; Pharr et al., 1996] for depositing a-C films with maximum sp^3 content. The majority of previous studies dealing with the structure of FCVA-deposited a-C films were focused on the effect of substrate bias but not the optimum C^+ ion energy. Therefore, a principal objective of this study was to perform a detailed analysis of the through-thickness structure of ultrathin a-C films synthesized by the FCVA technique under optimum C^+ ion energy conditions. Because the energy of C^+ ions generated by arcing is ~20 eV, [Robertson, 2003; Robertson, 2001; Byon and Anders, 2003] a substrate bias voltage of –100 V was used to obtain C^+ ion energy of ~120 eV during film deposition. High-resolution transmission electron microscopy (HRTEM) and analytical EELS were used to study the a-C film structure. Low- and high (core)-loss EELS spectra of Si and C were analyzed to determine the elemental content and through-thickness structure of ~20-nm-thick a-C films. Calculations of atomic carbon hybridization based on EELS spectra were used to track the film structure evolution. The average content of carbon hybridization in the top few nanometers of the a-C film determined from EELS analysis was validated by XPS results.

3.2 Experimental Procedures

3.2.1 Film deposition by filtered cathodic vacuum arc

Commercially available p-type Si(100) wafers were sectioned into 10×10 mm^2 substrates, which were cleaned by rinsing in isopropanol and acetone for 10 min, respectively, and dried by blowing nitrogen gas. After pumping down the FCVA chamber to $<5 \times 10^{-7}$ Torr and, subsequently, introducing Ar gas that increased the chamber pressure to 2×10^{-4} Torr, the substrate was sputtered for 2 min with 500-eV Ar$^+$ ions generated by a 64-mm Kaufman ion source to remove the native SiO$_2$ layer. The incidence angle of the bombarding Ar$^+$ ions was fixed at 60°, as measured from the normal to the substrate surface. After reaching a base pressure of $<5 \times 10^{-7}$ Torr, carbon plasma was generated by arcing on the cathode (99.99% pure graphite) surface and stabilized by a cusp-configuration magnetic field applied to the cathode.[Zhang and Komvopoulos, 2008] Any macroparticles and/or droplets were filtered out by the magnetic field of electromagnetic coils having an S-shape duct configuration. At the exit of the filter structure, the carbon plasma comprised only high-purity (~99.99%) C$^+$ ions. To control the C$^+$ ion energy during film deposition, a pulsed bias voltage of –100 V (time-average magnitude) and a 25 kHz frequency was applied to the substrate holder. To obtain ultrathin a-C films, the deposition time was set at 30 s. FCVA deposition under plasma conditions of –100 V substrate bias produces ultrathin a-C films with the highest sp^3 fraction and nanohardness.[Zhang and Komvopoulos, 2009] To enhance the film uniformity in the radial direction, the substrate was rotated at 60 rpm during film deposition. More details about the FCVA system used in this study can be found elsewhere.[Zhang and Komvopoulos, 2008]

3.2.2 Transmission electron microscopy and electron energy-loss spectroscopy

Cross-sectional TEM samples were prepared by mechanical grinding and dimpling and surface finished by ion milling. The film samples were cleaved into two halves and glued face-to-face using M-bond 610 epoxy. To ensure that the EELS carbon signal was only due to the *a*-C film, a thin Au layer was evaporated onto the sample surface before sample bonding. More details about the preparation of the TEM samples can be found elsewhere. [Wang and Komvopoulos, 2012; Wan and Komvopoulos, 2004] To minimize surface adsorption of hydrocarbon from the ambient, the TEM samples were kept in a vacuum of $<10^{-5}$ Torr and observed with the TEM within two days from fabrication.

HRTEM images and EELS spectra were obtained with a FEI Tecnai (F20 UT) spectrometer operated at 200 kV, using a CCD camera (2048 × 2048 pixels) positioned 42 mm behind the Gatan imaging filter. The spatial resolution of the scanning TEM (STEM), without a monochromator, is ~0.14 nm. A 13.5-mrad C2 semi-angle and a 100-µm C2 aperture were used in this study. The EELS collection semi-angle was set at 47 mrad. Using the full width at half maximum (FWHM) of the zero-loss peak (ZLP), the energy resolution was found equal to 0.58 eV, which is sufficiently small for distinguishing sp^2 from sp^3 hybridizations since their band gap difference is about 0.8–0.9 eV. ZLP and low-loss spectra were collected in 0.02 s. Because the core-edge signal is significantly weaker than elastic scattering, the Si $L_{2,3}$-edge and the C K-edge were collected for 4 s in order to enhance the observation of fine structure details.

3.3.3 X-ray photoelectron spectroscopy

A PHI 5400 XPS system (Physical Electronics, Chanhassen, MN) with conventional (non-monochromatic) Al-Kα radiation of 1486.6 eV energy and 4.8 eV work function operated under a vacuum pressure of $<2 \times 10^{-8}$ Torr was used to study carbon atom hybridization in the *a*-C films. The system has a spatial resolution of 0.5 mm and energy resolution of 0.7 eV. The spectrum of a clean Ag foil was used to calibrate the XPS system. The samples were not cleaned before the XPS analysis in order to preserve their surface elemental and chemical state and were fixed on the sample holder by conductive screws. To avoid possible charging effects, spectra were acquired near the fixture. Multiplex narrow-scan spectra of the C1s core-level peak were acquired with pass energy of 37.75 eV, using a channel width of 0.1 eV/step and acquisition time equal to 50 ms/step. Spectra were collected after 60 sweeps in the binding energy range of 280–292 eV. To ensure consistency, three spectra were obtained from different locations of the same sample. Before narrow scanning to obtain the C1s peak, a spectrum was collected in the binding energy range of 0–1100 eV using a step of 1 eV. The O1s peak obtained from this scan was found to be at 532.0 eV, indicating negligible charging effects on the samples during the XPS analysis.

3.3 Results and discussion

The removal of the native SiO_2 layer by the highly energetic Ar^+ ions may cause amorphization of the Si(100) substrate. The structure of the silicon substrate is important because it controls the initial growth of the carbon film. The bright-field, phase-contrast HRTEM image of the Si(100) substrate obtained after sputter cleaning with 500-eV Ar^+ ions (Figure 3.1A) shows the formation of a 2.5 ± 0.5-nm-thick surface layer of amorphous silicon (*a*-Si). The

difference in brightness is mainly due to density differences between Si(100) and *a*-Si. The HRTEM image of the *a*-C film deposited on the cleaned Si(100) substrate in 30 s under a substrate bias voltage of –100 V (Figure 3.1B) shows the formation of a ~20.9 ± 0.3-nm-thick *a*-C film, including an approximately 3-nm-thick interface layer of intermixed C, Si, and, possibly, SiC.

3.3.1 Plasmon peak

The elemental composition of the *a*-C film shown in Figure 3.1B was studied by analytical EELS. This technique uses the energy loss of electrons passing through the specimen to determine the chemical composition and electronic structure of the specimen. Electron energy loss is mainly due to inelastic electron-electron collisions. [Williams and Carter, 2009; Egerton, 2011] Beam electrons interacting with electrons of the conduction and/or valence bands of the specimen material are detected in the low-energy loss range (typically, <50 eV) of the EELS spectrum. Because the electronic properties of a material are controlled by the weakly bound electrons in the conduction and valence bands, the distribution of the EELS spectrum below 50 eV provides information about specific phases or features in the TEM image.

Assuming free electrons, i.e., not bound to any specific atom or ion, the energy loss E_p of the beam electrons generating a plasmon frequency ω_p is given by [Williams and Carter, 2009]

$$E_p = \frac{h}{2\pi}\omega_p = \frac{h}{2\pi}\left(\frac{ne^2}{\varepsilon_0 m}\right)^{1/2} \qquad (3.1)$$

where *h* is the Planck's constant, *e* and *m* are the electron charge and mass, respectively, ε_0 is the permittivity of free space, and *n* is the electron density. For single-crystal Si and *a*-C with a low sp^3 fraction, the plasmon peak position is typically at ~16–17 eV [Egerton, 2009; Olevano and Reining, 2001] and 24–25 eV, [McKenzie et al., 1991; Duarte-Moller et al., 1999] respectively, while for graphitic carbon and amorphous diamond the plasmon peak position is at 26–27 and 30–33 eV, respectively.[Duarte-Moller et al., 1999; Berger et al., 1988] The film structure can be examined by studying the through-thickness variation of the plasmon peak position.

Since the energy-loss spectrometer is susceptible to external fields and the ZLP shifts over time, each EELS spectrum was calibrated by shifting the ZLP to the zero position. Figure 3.2A shows a cross-sectional STEM image and EELS spectra obtained from different locations in the depth direction of the TEM sample. Spectrum (a) with a plasmon peak at ~16 eV corresponds to the Si(100) substrate. Location (b) is on the line of maximum contrast between Si(100) and amorphous structures. The plasmon peak position in spectrum (b) is slightly above 16 eV and its reduced intensity indicates a weakening of the Si signal. The large shift of the plasmon peak of spectrum (c) to ~21.7 eV is attributed to the contribution of plasmon signals from both Si and C. The contribution of Si features to the electron energy loss decays, while that of C features intensifies with increasing depth distance. The change from spectrum (b) to spectrum (c) reveals the existence of a thin interfacial region with gradually changing C and Si contents. The spectra obtained away from this interfacial region, i.e., spectra (d) and (e), have very similar distributions and a plasmon peak centered at ~29 eV. These spectra correspond to the bulk of the carbon film and are representative of steady-state film growth. A plasmon peak

position close to that of diamond indicates a high fraction of sp^3 hybridization. The plasmon peak position in spectrum (f) corresponding to the film surface is at ~24 eV, which is close to that of graphitized carbon. This implies that the surface structure of the carbon film is dominated by sp^2 hybridization. The gold layer shows a very weak plasmon signal (spectrum (g)), indicating insignificant hydrocarbon contamination of the TEM specimen. The plasmon peak in the epoxy spectrum (h) is centered at ~22 eV.

To quantify the change in the plasmon peak position in the depth direction of the cross-sectional TEM sample, EELS spectra were obtained at depth increments of 2 nm. Figure 3.2B shows the variation of the plasmon peak position in the depth sample direction after ZLP calibration. The zero-depth position corresponds to the location exhibiting the highest contrast between carbon film and the gold layer (i.e., film surface). The low-energy-loss range (<50 eV) reveals a multilayered structure consisting of single-crystal Si, amorphous C, Si, and, possibly SiC (interface layer), graphite-like carbon (buffer layer), diamond-like carbon (bulk film), and graphite-like carbon (surface layer).

3.3.2 Silicon concentration

The high-energy-loss range (>50 eV) contains information about inelastic interactions between beam electrons and inner or core-shell electrons. Thus, information about the elemental composition can be extracted from the ionization edges. Since the interface layer was found to consist of C and Si, its elemental concentration was determined from the core-loss energy of the Si $L_{2,3}$ peak centered at 99 eV along a 20-nm-long scan line using a step increment of 0.5 nm. The silicon concentration was calculated as the ratio of the Si $L_{2,3}$ peak intensity in the spectrum of the interface layer to that in the spectrum of the single-crystal Si(100) region. Figure 3.3A shows high-energy-loss spectra obtained from different locations after background subtraction. Spectra (a) and (b) correspond to the Si(100) substrate, and their similar distributions and strength intensities indicate similar structures and compositions. A comparison of spectra (c)–(e) shows a profound decrease in the intensity of the Si $L_{2,3}$ peak. This trend is attributed to the continuously decreasing Si concentration through the interface layer and toward the interface with the bulk film. The normalized intensity of the Si $L_{2,3}$ peak, defined as the ratio of the area under the EELS spectra from 94 to 104 eV to the corresponding area of the Si(100) spectrum, is shown as a function of depth in Figure 3.3B. Because all of the measurements were obtained along a very short distance (20 nm), variations in the specimen thickness were negligible and the variation of the signal intensity is only due to the relative concentration of Si. The transition band has a thickness of ~4.5 nm, which is slightly larger than that of the a-Si layer on the Si(100) substrate (Figure 3.1A). This difference may be attributed to the bombardment effect of energetic C^+ ions in the initial stage of film deposition, resulting in the implantation of C into the Si substrate and, in turn, thickening of the a-Si layer at the interface of the Si(100) substrate and the a-C film.

3.3.3 Carbon concentration

Figure 3.4 shows high-energy-loss spectra of the C K-edge obtained in the depth direction of the cross-sectional TEM sample using a step size of 0.5 nm. The locations from where spectra were obtained are very close to those shown in Figure 3.2A. Spectra locations were slightly offset during the acquisition of the low- and high-energy-loss spectra to avoid sample damage

and/or carbon re-deposition from previous spectra acquisitions. All C K-edge spectra were calibrated by centering the π^* peak at 285 eV. As expected, spectra (a) and (b) of the Si(100) substrate are featureless. However, spectrum (c) of the interface layer contains a small π^* peak and a well-defined σ^* peak, with both peaks attributed to electron beam interactions with C atoms. The similar distributions and significantly intensified signal in spectra (d) and (e) indicate a high carbon concentration in the bulk film. The decrease of the signal intensity at the film surface and the dominance of the π^* peak in the corresponding spectrum (f) suggest that carbon atom hybridization at the film surface is predominantly sp^2. The gold layer does not produce C K-edge signal (spectrum (g)), while the epoxy shows a strong π^* peak and a weak σ^* peak (spectrum (h)). Information about the chemical composition and carbon hybridization of the a-C film derived from Figure 3.4 is in good agreement with that obtained from Figure 3.2A.

3.3.4 Carbon film hybridization

EELS spectra in the range of 280–305 eV were analyzed to determine the sp^2 and sp^3 fractions in the a-C film. Figure 3.5 shows a representative high-energy-loss spectrum of the a-C bulk film. The location in the bulk film from where the spectrum was obtained is marked by a circle in the STEM image shown on the right. The peak at 285 eV is due to the excitation of electrons from the ground-state 1s core levels to the vacant π^* states. The π^* peak is fitted with a Gaussian distribution, whereas the σ^* peak is integrated within a small energy window from 290 to 305 eV in order to minimize effects of plural scattering. The area ratio of these two peaks is proportional to the relative number of the π^* and σ^* orbitals.[36] The fraction of sp^2 bonded carbon atoms x is given by [Cuomo et al., 1991]

$$\frac{(\pi^*/\sigma^*)_{\text{film}}}{(\pi^*/\sigma^*)_{\text{std}}} = \frac{3x}{4-x} \tag{3.2}$$

where the standard sample is assumed to be pure graphite with 100% sp^2 atomic carbon hybridization.

Figure 3.6A shows a depth profile of the sp^3 fraction calculated from the C K-edge spectra using Eq. (3.2). Similar to the Si $L_{2,3}$-edge, the intensity of the C K-edge was calculated from an integration performed from 280 to 305 eV. The depth profile of the normalized C K-edge intensity is shown in Figure 3.6B. The sp^3 atomic fraction (Figure 3.6A) and the carbon concentration (Figure 3.6B) reveal the existence of six distinctly different regions through the cross-sectional sample. Data points of the sp^3 fraction are not shown in range I because the C signal intensity is almost zero in the Si(100) substrate. Region II represents the ~4.5-nm-thick interface layer and is characterized by an increasing C concentration and a merely constant sp^3 fraction of ~45.0 ± 5.8%. In the ~2-nm-thick carbon layer above the interface layer (region III), the carbon intensity reaches a maximum, while the sp^3 fraction increases from ~45% to ~70%. The next region IV corresponds to a ~12.5-nm-thick bulk a-C film with a constant sp^3 fraction equal to 73.2 ± 1.9%. The sp^3 fraction in the ~1.5-nm-thick surface layer of the a-C film (region V) rapidly decreases to 50.6 ± 3.3% toward the surface. Region VI represents a gold particle separating the a-C film from the epoxy glue. Because of the low carbon signal produced by the gold particle, data of the sp^3 fraction were also omitted from region VI.

Different from the traditional three-layer model of carbon films deposited by energetic carbon ions, [Siegal et al., 2000; Davis et al., 1998; Davis et al., 1995; Lifshitz et al., 1990] a

fourth (buffer) layer of thickness ~2 nm was discovered between the interface layer consisting of intermixed C and Si and the bulk of the a-C film. The buffer layer exhibits a very high carbon concentration (>95%) and its sp^3 fraction increases from the substrate interface toward the bulk film interface with the increase of the thickness of the interface layer. The observed four-layer structure of the ultrathin a-C film can be explained by the following film-growth model. The initial stage of film deposition is dominated by backscattering and penetration of energetic C^+ ions into the a-Si surface layer of the substrate, resulting in the growth of an interface (intermixing) amorphous layer consisting of C, Si, and, possibly, SiC. This interface layer exhibits a relatively low sp^3 fraction because of the low carbon concentration. Although the structure of SiC is similar to that of an sp^3 hybridized carbon structure, the ionization energy of C1s core-level electrons of carbidic components is usually in the range of 282.3–283.4 eV with a broad FWHM of ~2 eV, [Iwanowski et al., 1999] which is much lower than the ionization energy of sp^3 carbon atom hybridization. Therefore, even if there is some SiC formed at the interface layer, it won't help increasing the sp^3 fraction. This explains the low sp^3 concentration in the interface layer (region II), despite of the possible existence of SiC. The arrival of more C^+ ions leads to the formation of a thin buffer layer of pure carbon (region III) on top of the interface layer. However, because the C^+ ion penetration depth exceeds the initial thickness of the buffer layer, some of the impinging C^+ ions are backscattered by the Si atoms in the interface layer. Since the probability of C^+ ion-Si atom interaction decreases with the thickness of the buffer layer, the sp^3 fraction exhibits a positive gradient toward the interface of the buffer layer with the bulk film. When the thickness of the buffer layer exceeds the penetration depth range of the C^+ ions, only carbon-carbon interactions occur and the localized compressive stresses induced by the subplantation process promote the occurrence of sp^3 hybridization. The resulting steady-state film growth conditions lead to the formation of the bulk film with constant and high sp^3 content (region IV). However, because the bulk film surface experiences relatively less C^+ ion bombardment, a surface layer with increased sp^2 content and thickness about equal to the C^+ ion penetration (region V) is produced during the final stage of film deposition.

The sp^3 fraction was also calculated from the C1s core-level XPS spectrum shown in Figure 3.7. The C1s peak was deconvoluted by five Gaussian distributions corresponding to sp^1 (C1s-1), sp^2 (C1s-2), sp^3 (C1s-3), C–O (C1s-4), and C=O (C1s-5) carbon bonding. Details about the deconvolution method can be found elsewhere.[Wang and Komvopoulos, 2012;Wan and Komvopoulos, 2007] The sp^3 fraction is usually defined as the ratio of the area under the corresponding distribution to the sum of the areas under the sp^2 and sp^3 distributions. On the basis of this definition, the sp^3 fraction determined from XPS analysis is equal to 73.9 ± 1.5%. However, in the EELS C K-edge spectrum only the π* and σ* peaks were used to represent the sp^2 and sp^3 hybridizations, respectively, while the XPS C1s spectrum was deconvoluted by five Gaussian distributions. Thus, to compare EELS with XPS results, it is necessary to define the sp^3 fraction as the ratio of the area under the sp^3 distribution to the sum of the areas of the five Gaussian distributions used to deconvolute the C1s peak. Using this definition, the sp^3 fraction is found equal to 58.7 ± 0.8%, which is significantly lower than the value (73.2 ± 1.9%) calculated from the EELS C K-edge spectrum.

This discrepancy is expected because XPS is a surface-sensitive method. The XPS signal from the subsurface is attenuated due to inelastic scattering of photoelectrons travelling through the specimen. The probability of a single photoelectron scattering event can be estimated by:

$$P(x) = e^{-x/\lambda} \tag{3.3}$$

where x is the distance traveled and λ is the inelastic mean free path of a photoelectron. For $x = \lambda$ and 3λ, Eq. (3.3) gives $P(\lambda) = 0.368$ and $P(3\lambda) = 0.05$, respectively, implying 63.2% and 95% of the photoelectrons detected originate from within the distances 1λ and 3λ below the sample surface, respectively. The inelastic mean free path for carbon materials for 1486.6 eV photoelectron energy is typically in the range of 1–3.5 nm. [Tanuma et al., 1991; Gries, 1996] Assuming $\lambda = 1.5$ nm, which is equal to the thickness of the surface layer, a linear relation between sp^3 fraction and XPS signal intensity, and using the sp^3 fraction of the surface layer and the bulk film determined from the EELS analysis (50.6 ± 3.3% and 73.2 ± 1.9%, respectively), the sp^3 fraction of the a-C film is: 63.2% × 50.6% + (1–63.2%) × 73.2% = 58.92%, which is close to the value (58.7 ± 0.8%) predicted by XPS. The significantly lower sp^3 fraction obtained from the XPS analysis provides supportive evidence of the formation of a thin surface layer of significantly lower sp^3 fraction than that of the bulk a-C film.

3.4 Conclusions

The structure of ultrathin a-C films deposited by the FCVA method under plasma conditions of optimum substrate bias voltage was studied in the light of TEM, EELS, and XPS results. The plasmon excitation energy position in low-energy-loss spectra revealed a multilayered film structure. Depth profiles of carbon atom concentration and sp^3 carbon hybridization obtained from the analysis of high-energy-loss spectra showed that the film structure consists of a ~4.5-nm-thick interface layer (a mixture of C, Si, and, possibly, SiC), a ~2-nm-thick buffer layer of pure carbon with outward increasing sp^3 fraction, a ~12.5-nm-thick bulk film of constant and high sp^3 fraction (~74%), and a ~1.5-nm-thick surface layer of high sp^2 content. XPS results confirmed the sp^3 fraction calculated from the C K-edge EELS spectrum. The buffer and surface layers possess similar thickness, which depends on the C^+ ion penetration depth that is controlled by the kinetic energy of the bombarding C^+ ions. The results of this study show that the minimum thickness of a-C films deposited by FCVA under conditions of optimum substrate bias (–100 V) is equal to 3–3.5 nm, which is the total thickness of the buffer and surface layers. The a-C film thickness can be further decreased by considering the effects of other important FCVA process parameters on film growth, such as the incidence angle effect of energetic C^+ ions bombarding onto the growing film surface [Wang and Komvopoulos, 2012].
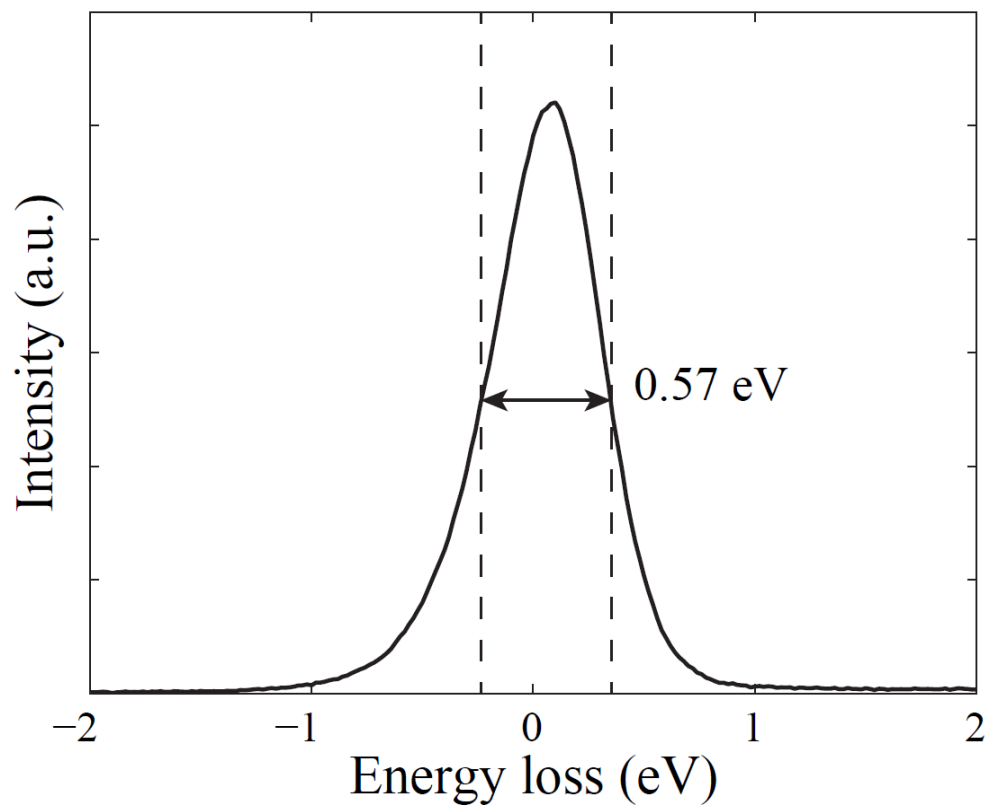
Figure 3. 1 Zero-loss-peak and its FWHM
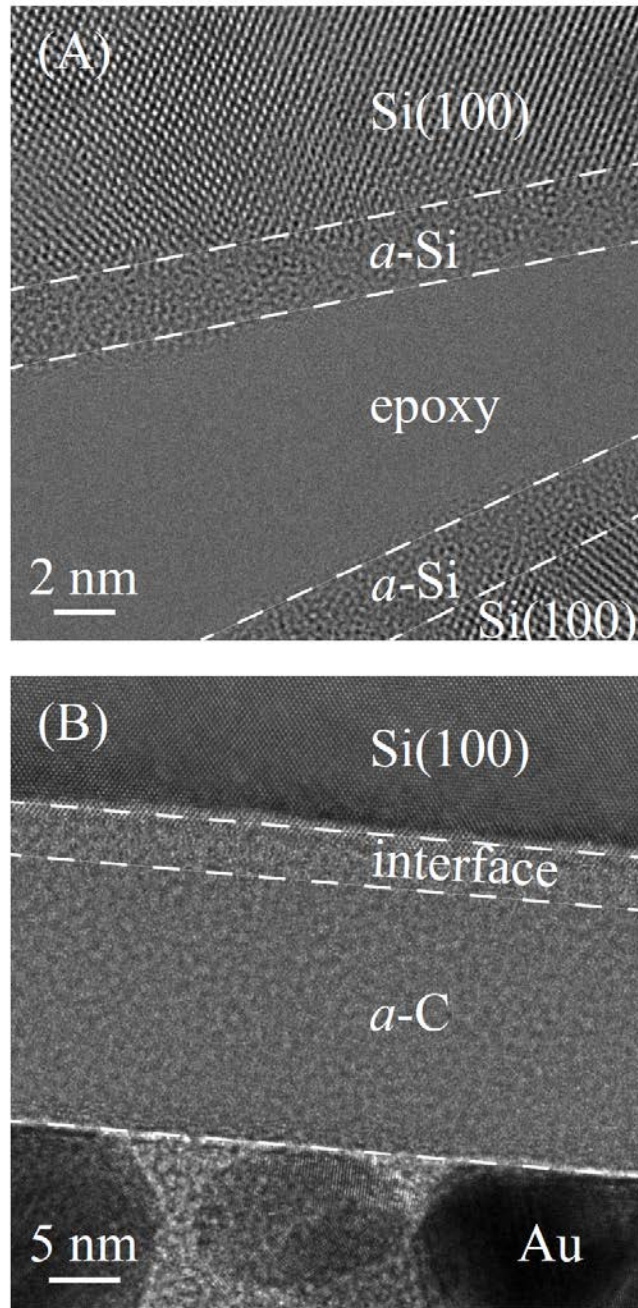
Figure 3. 2 Bright-field HRTEM images of (A) the Si(100) substrate after a 2-min sputter-etching by 500-eV Ar$^+$ ions to remove the native SiO$_2$ layer and (B) the a-C film deposited in 30 s on the sputter-etched Si(100) substrate by the FCVA method under plasma conditions of optimum substrate bias voltage (–100 V). Interfaces are distinguished by dashed lines.
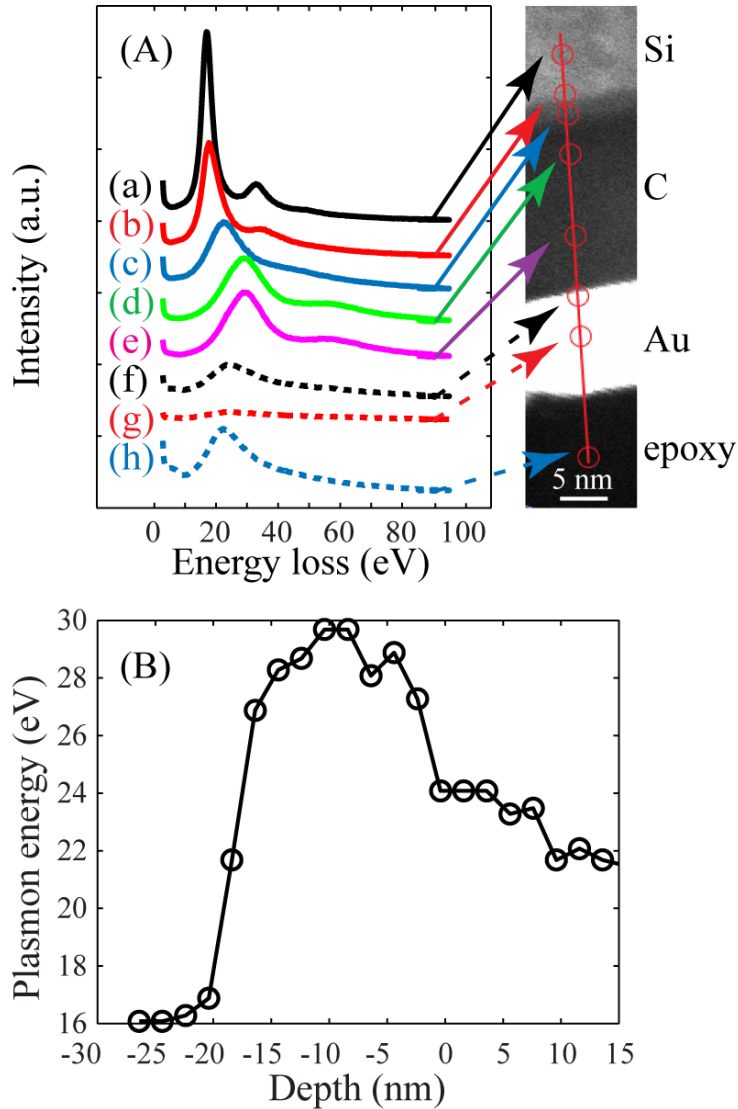
Figure 3. 3 (A) EELS spectra obtained from different locations across the interface of the Si(100) substrate and the *a*-C film, shown in the z-contrast STEM image shown on the right. The brightest region corresponds to evaporated Au used to distinguish the surface of the *a*-C film from the epoxy surface. The spectra were calibrated by shifting the ZLP to 0 eV. Local electronic change at the atomic level is discerned according to the position of plasmon peak. (B) Depth profile of the plasmon peak position.
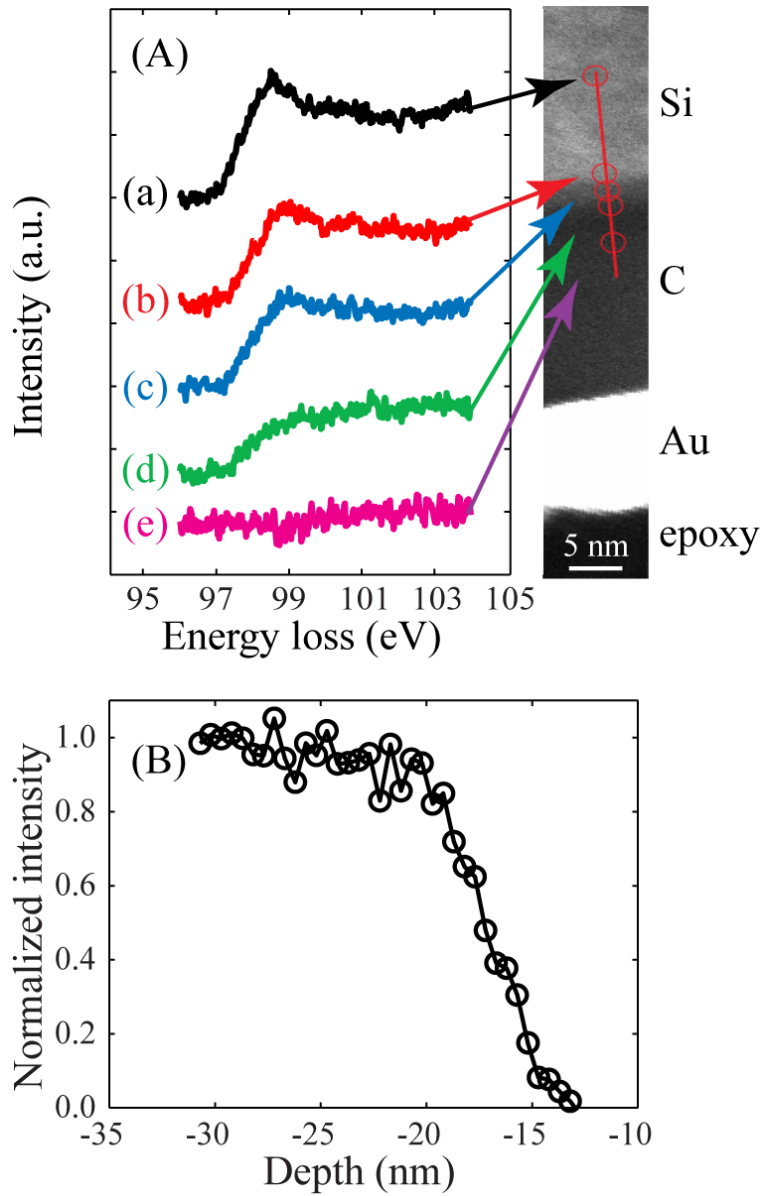
Figure 3. 4 (A) Variation of the Si $L_{2,3}$-edge across the interface of the Si(100) substrate and the *a*-C film, shown in the STEM image shown on the right. The spectra were calibrated by shifting the Si $L_{2,3}$-edge to 99 eV after background subtraction. (B) Depth profile of the normalized intensity of the Si $L_{2,3}$-edge.
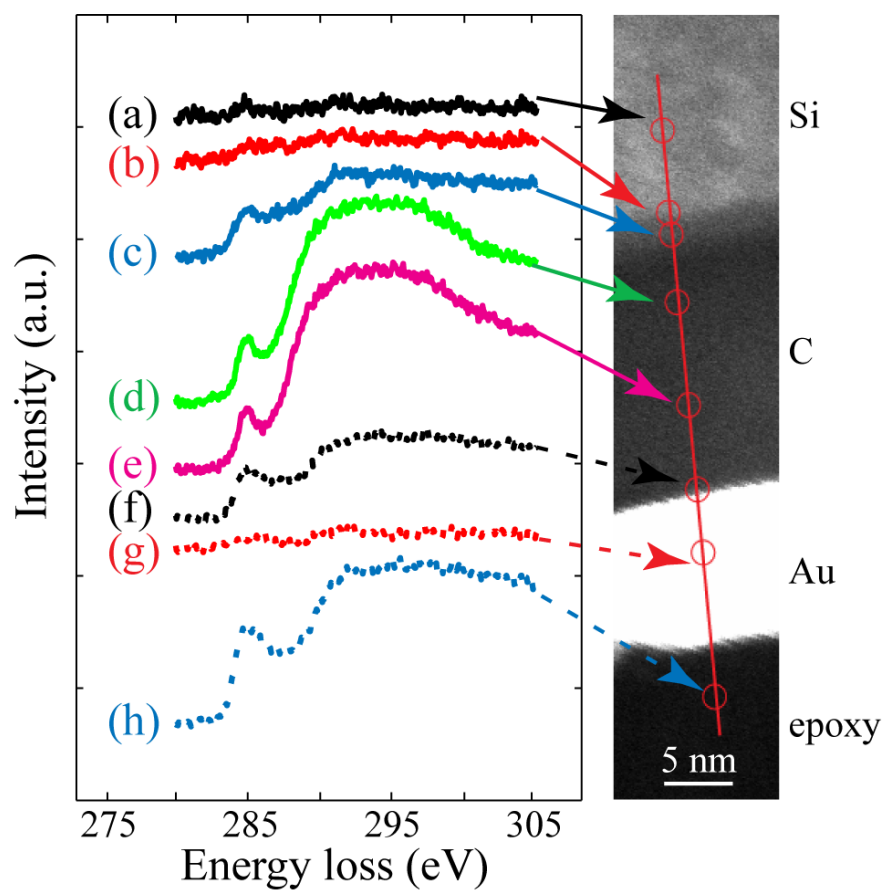
Figure 3. 5 C K-edge spectra obtained from different locations across the interface of the Si(100) substrate and the *a*-C film, shown in the STEM image shown on the right. The spectra were calibrated by shifting the π^* peak of all C K-edge spectra to 285 eV after background subtraction.
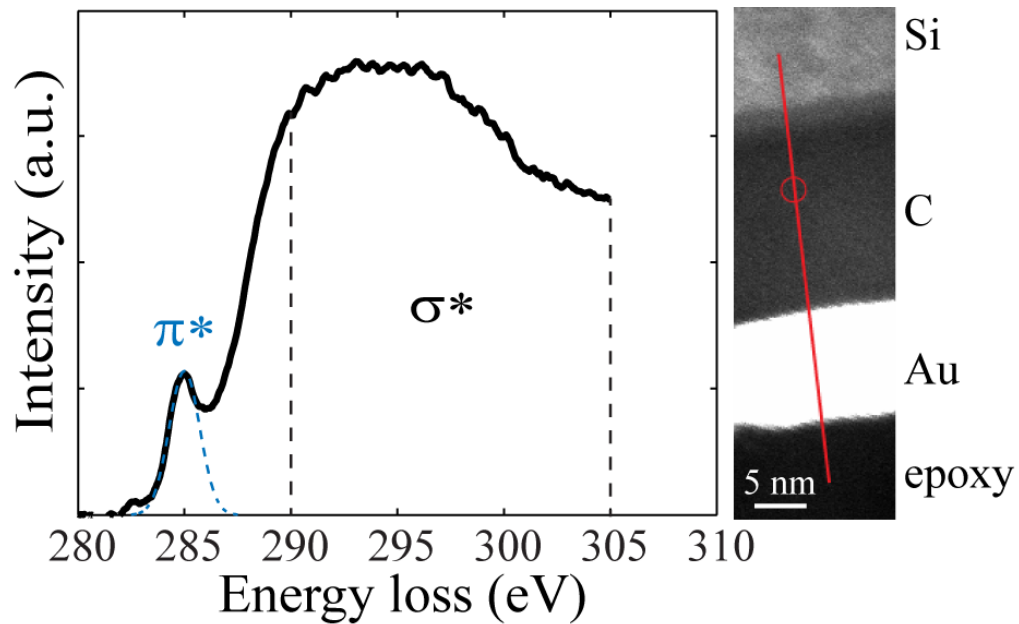
Figure 3. 6 Decomposition of the C K-edge spectrum of the *a*-C bulk film into π^* and σ^* peaks. The location in the bulk film from where the spectrum was obtained is marked by a circle in the STEM image shown on the right. The π^* peak is represented by a Gaussian distribution from 282 to 287.5 eV, whereas the σ^* peak is defined as the spectrum in the energy window from 290 to 305 eV.
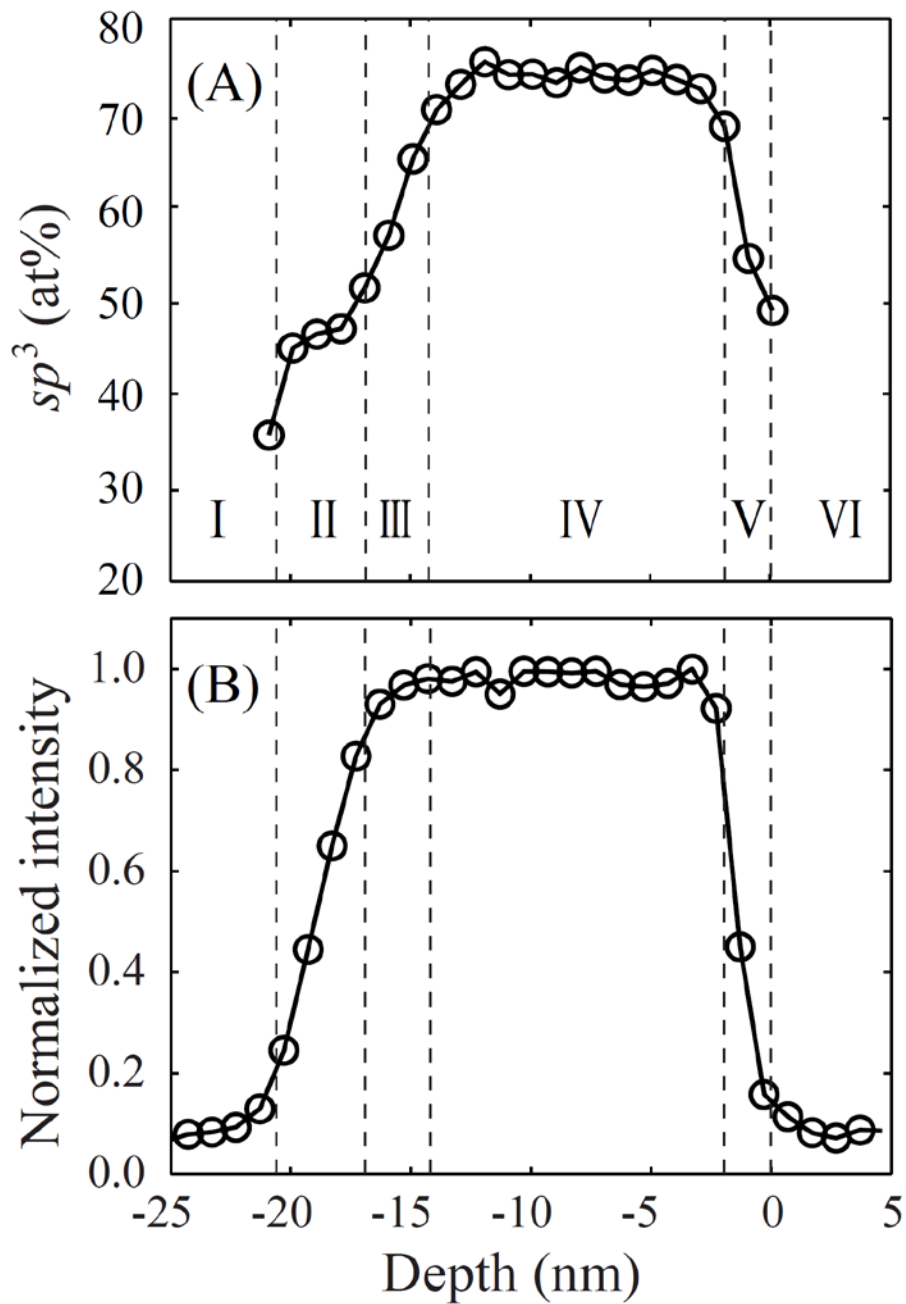
Figure 3. 7 Depth profiles of (A) the sp^3 fraction calculated from C K-edge spectra and (B) normalized intensity of the C K-edge. Boundaries of neighboring regions are distinguished by dashed lines.
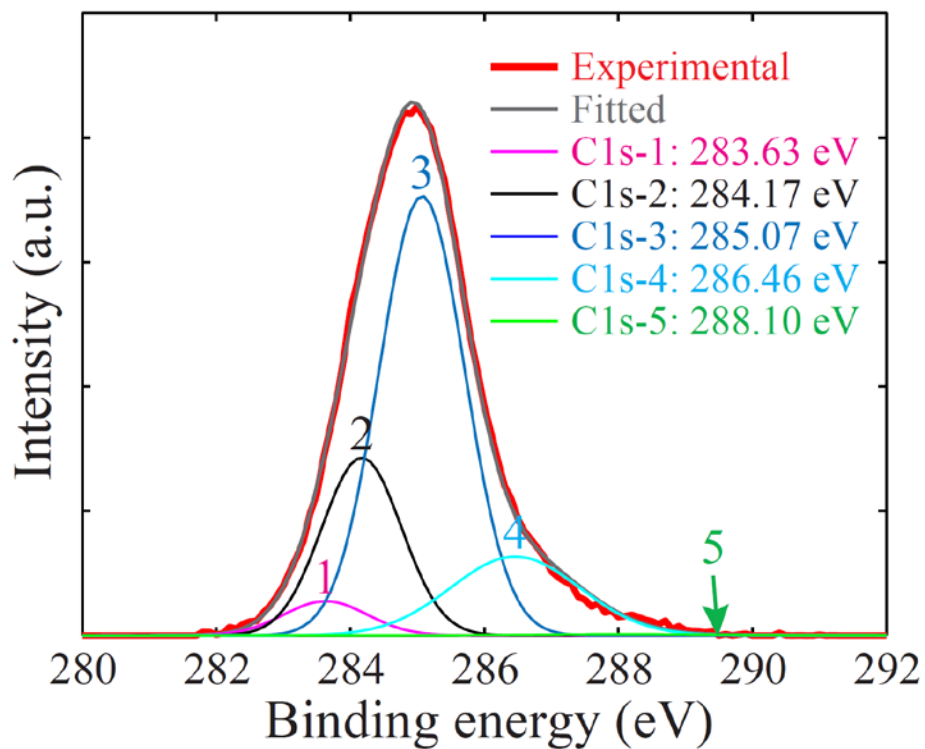
Figure 3. 8 C1s core-level XPS spectrum of *a*-C film after Shirley inelastic background subtraction with five fitted Gaussian distributions corresponding to sp^1, sp^2, sp^3, C–O, and C=O carbon bonding.

Chapter 4

FCVA deposition: incidence angle effect of energetic carbon ions on deposition rate, topography, and structure of ultrathin amorphous carbon films

4.1 Introduction

To achieve magnetic storage levels of 1Tb/in^2 and beyond in next-generation HDDs [Wood, 2009; Bandić and Victora, 2008; Yuan et al., 2009], the physical gap between the magnetic head and the hard disk must be reduced to less than 2~4 nm, implying an overcoat thickness of less than ~2 nm [Robertson, 2003; Ferrari, 2004; Goglia et al., 2001; Casiraghi et al., 2004(A); Casiraghi et al., 2004(B); Zhong et al., 2009]. It is critical that this significant decrease in overcoat thickness does not degrade important film properties, such as high sp^3 content, low surface roughness (≤ 0.2 nm) [Casiraghi et al., 2004(A)], and high hardness (> 40 GPa) [Beghi et al., 2002]. Traditional deposition methods, such as sputtering, cannot produce continuous ultrathin a-C films of such high quality. FCVA is a promising alternative method that allows for deposition of continuous a-C films of a thickness less than 2 nm.

However, the FCVA-deposited *a*-C film has a multilayer structure due to the subplantation of the energetic ions, as investigated in Chapter 3. By studying the STEM-EELS spectrum of the cross-section sample, we find out that, with the optimum substrate bias (-100 V), the minimum thickness of a-C films deposited by FCVA is about 3-3.5 nm, which includes the buffer layer and surface layer. In order to further decrease the a-C film thickness, we need to consider optimizing other FCVA process parameters beyond substrate bias.

The film precursors in FCVA are energetic ions, which imping onto the substrate surface resulting in direct and/or recoil implantation and deposition, depending on the process conditions (e.g., substrate pulsed bias voltage). To deposit thin films, the total number of ions arriving at the growing film surface may be reduced by decreasing either the deposition time or the arc discharge current. However, both of these approaches are limited, because there is a minimum arc discharge current to ignite the plasma and stable arcing cannot be established in a very short time. A more effective approach for depositing thin films is to increase the ion energy. High-energy ions can knock-off atoms from the film surface, resulting in the formation of thin films [Zhang and Komvopoulos, 2008]. However, because the film quality depends strongly on the ion energy, arbitrary changes in the ion energy might be detrimental to the film properties [Robertson, 2002; Brown, 1998; Zhang and Komvopoulos, 2009; Zhu et al., 2008].

Varying the incidence angle of bombarding ions is more advantageous because the effect on the film microstructure and properties is secondary compared to that resulting from changes in the ion energy or ion fluence [Cuomo et al., 1992]. Consequently, an alternative approach for ultrathin a-C film deposition by the FCVA method might be to vary the incidence angle of

impinging ions θ (defined as the angle between the trajectory of the C+ ions and the substrate normal), while maintaining the desired C+ ion energy. This method is referred to as oblique deposition and is depicted schematically in Figure 4.1.

Oblique deposition has been used to synthesize films of specific surface structure or orientation on patterned substrates, such as nano-imprinted solar cells [Yang et al., 2010] and fibers [Yusop et al., 2011; Jayawardhana et al., 2011]. However, fundamental studies of oblique deposition on smooth substrates are sparse. In particular, the role of sputtering during deposition has not been elucidated, while knowledge of the incidence angle effect on the quality and thickness of ultrathin a-C films is limited. Molecular dynamics (MD) simulations have been used to study the incidence angle effect on film growth. Dong et al. [1996] used the Lennard-Jones potential to describe interatomic forces and obtained MD simulation results showing a decrease in film density and void formation with increasing deposition angle. Ma et al. [2007] simulated interatomic force interactions by the reactive-empirical-bond-order potential and reported a decrease in film density, sp^3 fraction, and compressive stress with increasing incidence angle. The incidence angle effect on film deposition has also been examined in several experimental studies. Cuomo et al. [1992] studied the incidence angle effect on the quality of DLC films deposited by various methods and observed a sharp decrease in the sp^3 content of DLC films deposited by pulsed laser vaporization for incidence angles larger than 45°; however, the incidence angle effect on the sp^3 content of DLC films deposited by FCVA was not considered in that study. Liu et al. [2003] used pulsed cathodic arc to deposit DLC films of thickness in the range of 60~120 nm and discovered that ~100-nm-thick DLC films possessed lower sp^3 contents and higher roughness for incidence angles above 80° and below 50°. Raman spectroscopy studies of Liu et al. [2007] have shown significantly lower internal stresses in DLC films deposited at large incidence angles; however, the effect on the hardness was less significant, while the film structure was not examined in the light of direct microanalysis results.

In contrast to other deposition methods, FCVA with a filtering mechanism yields high-quality plasmas and enables the modulation of the energy of bombarding ions via a pulsed bias voltage applied to the substrate. During substrate biasing, ions accelerate through the plasma sheath and bombard the growing film surface, while in the absence of substrate biasing, film growth is governed by atomic diffusion and collision cascades at the film surface. Different from other deposition methods, the incidence angle effect in FCVA is only encountered during substrate biasing, with the pulsed bias voltage leading to the formation of a three-layer structure consisting of the substrate, an intermixing layer, and a surface film [Liu and Wang, 2009]. The properties of ultrathin films deposited by the FCVA method are expected to differ from those of thicker films. Since previous studies were focused on relatively thick films (> 60 nm), understanding the incidence angle effect on the growth of ultrathin a-C films synthesized by the FCVA method is of high importance.

The objective of the present study was to examine the effect of the incidence angle of energetic carbon ions on the deposition rate, topography (roughness), and structure of FCVA-deposited ultrathin a-C films. Film depth profiles were determined from Monte Carlo simulations and cross-sectional transmission electron microscopy (TEM), while the topography (roughness) and structure of the films were examined by atomic force microscopy (AFM) and X-ray photoelectron spectroscopy (XPS), respectively. Analytical and experimental results are

contrasted to illustrate the incidence angle effect on the quality of ultrathin a-C films and to determine the optimum incidence angle for FCVA film deposition.

4.2 Experimental and simulation procedures

4.2.1 Film deposition process parameters

It has been reported that local compressive stresses favors the formation of sp^3 hybridization, whereas tensile stresses are conducive to sp^2 hybridization. During FCVA deposition, collision cascades between C^+ ions and film atoms increase the local density and compressive stress, leading to $sp^3 \rightarrow sp^2$ rehybridization. Although the sp^3 fraction increases with the C^+ ion energy, thermal relaxation, which promotes $sp^3 \rightarrow sp^2$ rehybridization, becomes an important factor at high ion energy levels. Therefore, there is an optimum ion energy (typically, equal to ~120 eV [Robertson, 2002; Pharr et al., 1996]) for producing carbon films with maximum sp^3 content. Because the energy of the C^+ ions generated by discharge arcing is ~20 eV [Robertson, 2001; Robertson, 2003; Pharr et al., 1996; Chhowalla et al., 1997; Byon and Anders, 2003], a substrate bias voltage of –100 V and 25 kHz frequency was applied during FCVA deposition (figure 4.1) to increase the energy of impinging C^+ ions. Substrate biasing was applied during 70% of each pulse period (i.e., 70% duty cycle). Substrates (10×10 mm^2) cut from a p-type Si(100) wafer were first cleaned with acetone and then bombarded for 2 min by 500-eV Ar$^+$ ions at an incidence angle of 60° to remove the native oxide film. In all film depositions, the base and working pressures were less than 8×10^{-7} and 1×10^{-4} Torr, respectively, the deposition time was fixed at 30 s, and the carbon ion flux at the substrate holder was equal to ~1.48×10^{15} ions/cm^{2}s, as measured in a previous study [Zhang and Komvopoulos, 2008]. Other Details of the FCVA system can be found in Chapter 2.

4.3.2 Cross-section TEM measurements

As we are investigating the ultrathin carbon films with thickness on order of several nanometers, conventional thickness measurement methods such as mechanical stylus, ellipsometry cannot meet our requirements in terms of resolution. Thus, Cross-sections of films deposited at incidence angles in the range of 0-70˚ were examined with the high-resolution TEM (Philips CM200/FEG) to measure the film thickness. Details about the TEM sample preparation and the TEM system can be found in chapter 2.

4.3.3 T-DYN simulation of films' depth profiles

TRIM-DYNAMIC (T-DYN) is a Monte Carlo simulator based on the classical trajectory method that accounts for binary collisions during deposition. In this study, the depth profiles of deposited films were simulated with a 4.0 Version. This code developed by Biersack [Biersack et al., 1991; Biersack, 1999] can handle energetic ion bombardment and simultaneous deposition of neutral atoms at the surface. During the simulation, the information of all incidence ions, recoil atoms, primary knock-on atoms and secondary knock-on atoms were stored and updates were made based on their interactions.

To best simulate the experimental conditions, simulations were performed for ion energy equal to 120 eV, similar to that used in the film deposition experiments. The binding energy and

surface binding energy of Si were set equal to 2.32 and 4.7 eV and those of carbon to 2.27 and 7.41 eV, respectively. The ion incidence angle was varied between 0˚ and 85˚ at increments of 5˚. The accuracy of the simulated depth profiles was confirmed through comparison with the cross-section TEM measurements.

4.3.4 Film hybridization and topography measurement

The film hybridization has been characterized with XPS and the surface topography measurement has been carried out with AFM. The film topography was examined in light of 1×1 μm^2 surface area images with AFM operating in tapping mode at a drive frequency of 278.24 Hz. For statistical analysis, three different surface locations of two a-C films deposited under identical FCVA conditions were imaged with the AFM, and the obtained roughness data were assumed to follow normal distributions. Other experimental details regarding XPS and AFM can be found in chapter 2.

4.3 Results and discussion

4.3.1 Film thickness measured by TEM

Figure 4.2 shows the cross-sectional TEM images of a-C films deposited at different incidence angles. The periodic array of the substrate is illustrative of the single-crystal structure of Si(100). The structure regularity decreases near the substrate interface with the intermixing layer and finally disappears into the film, indicative of the amorphous structure of the intermixing layer and the carbon film. Fast Fourier transform analysis confirmed that the zone axis in all images is in the [110] direction of the silicon lattice due to sample titling. Structure and contrast differences in the TEM images reveal a three-layer structure consisting of crystalline Si(100) substrate, intermixing layer consisting of C, Si, and possibly SiC, and carbon film. The total thickness of intermixing layer and a-C film in Figure 4.2(a)–4.2(d) is about 19.5, 16.8, 6.64, and 5.48 nm, respectively. Contrast differences in TEM bright-field imaging are due to the occlusion and absorption of electrons into the sample. Density differences [Wan and Komvopoulos, 2004] and internal stress due to lattice misfit and/or point defects at the Si/C interface [Dulong et al., 2008; Yao and Thölen, 2000; Lu et al., 2011] may also contribute to contrast differences. Therefore, the contrast between the intermixing layer and the bulk of the a-C film suggests that the intermixing layer is at a different stress state and possesses a different chemical composition and/or density than the a-C film. Based on contrast differences, the thickness of the intermixing layer in Figure 4.2(a)–4.2(d) is estimated to be approximately 5.15, 4.05, 3.17, and 2.12 nm, respectively. Siegal et al. [2000] have reported that normal-incidence FCVA deposition of a-C films on Si produces an approximately 4-nm-thick intermixing layer, which is in fair agreement with the 5.15 nm thickness of the intermixing layer estimated from the TEM image shown in Figure 4.2(a). A comparison of the TEM images shown in Figure 4.2 indicates a significantly smaller a-C film thickness for relatively large incidence angle (i.e., θ = 60˚ and 70˚). For the largest incidence angle of 70˚, in particular, it is difficult to distinguish the three-layer structure observed with smaller incidence angles. The rough interface observed in the TEM image shown in Figure 4.2(d) suggests that the formation of an ultrathin a-C film at very large incidence angles (i.e., θ ≥ 70˚) occurred under intense sputtering plasma conditions, which is expected since sputtering theory predicts a maximum sputtering rate at an incidence angle of ~70˚ [Sigmund, 1969].

Figure 4.3 shows carbon depth profiles simulated with the T-DYN code for incidence angle between 0˚ and 75˚ and C^+ ion fluence of 0.9×10^{16}, 4.5×10^{16}, and 9.0×10^{16} ions/cm^2, with corresponding deposition time equal to 6, 30, and 60 s, i.e., ion flux fixed at 1.5×10^{15} ions/cm^{2}s, which is very close to the experimentally measured C^+ ion flux (1.48×10^{15} ions/cm^{2}s) at the sample holder [Zhang and Komvopoulos, 2008]. Short deposition time (low ion fluence) mainly yields C^+ ion implantation into the Si substrate, resulting in the formation of an intermixing layer of C and Si (Figure 4.3(a)). However, increasing the deposition time produced a three-layer structure consisting of silicon substrate, intermixing layer, and carbon film (Figure 4.3(b)). Further increasing the deposition time increased the carbon film thickness without affecting the thickness of the intermixing layer (Figure 4.3(c)). The decrease of the carbon film thickness with the ion fluence is due to the availability of fewer C^+ ions. For all deposition times (or ion fluences) and ion kinetic energy fixed at 120 eV, the depth of the carbon profile decreased with the increase of the incidence angle, evidently due to the decrease of the C^+ ion velocity normal to the substrate surface, which, in turn, decreased the depth travelled by carbon ions and atoms.

Figure 4.4 shows T-DYN simulation results of the total carbon thickness (0–100 at% C) and the intermixing layer thickness (5–85 at% C) as functions of incidence angle and ion fluence. The region of 85–100 at% C is considered to represent the carbon film. In regions with less 5 at% C, carbon ions are presumed to produce point defects in the Si lattice and, therefore, this region was neglected in the calculation of the intermixing layer thickness. For small incidence angle (i.e., $\theta < 30˚$), ion-surface interactions were localized (i.e., limited surface diffusion of carbon) due to the low in-plane velocity of impinging C^+ ions. However, the significant increase of the in-plane ion velocity for $\theta > 30˚$ promoted C–Si and C–C collisions at the surface and increased the sputtering rate. This non-local effect led to the decrease of the total carbon thickness (Figure 4.4(a)) and, in particular, the thickness of the intermixing layer (Figure 4.4(b)) with the increase of the incidence angle above 30˚. The T-DYN results show that the total carbon thickness is affected by both the incidence angle and the ion fluence (Figure 4.4(a)), while the thickness of the intermixing layer is only affected by the incidence angle (Figure 4.4(b)), for the ion fluence range examined in this study.

4.3.2 Deposition and sputtering mechanisms during film growth

Figure 4.5(a) shows simulation results of the deposition yield Y (i.e., fraction of C^+ ions deposited and/or implanted into the Si substrate) for different incidence angles. For a given incidence angle θ and C^+ ion energy E, the relative deposition yield is defined as the ratio $Y(E, \theta)/Y(E, \theta = 0)$. The minimum deposition yield is observed at $\theta_{min} = 72.8˚$, while the effect of the C^+ ion fluence on the deposition yield is secondary. Similar to ion sputtering [Sigmund, 1969; Wei et al., 2008], the deposition yield is mainly controlled by two factors – the ion fluence and the ion penetration depth. At small incidence angles, the effect of the ion fluence I is dominant, and Y decreases with the increase of θ because $I = I_0 \cos\theta$, where I_0 is the total C^+ ion fluence at zero incidence angle. However, at incidence angles above a critical θ value, the effect of the ion penetration depth becomes dominant, and the decrease of the ion penetration depth with the increase of θ decreases the sputtering rate, resulting in the increase of the sputtering yield Y (Figure 4.5(a)). According to sputtering theory [Wei et al., 2008],

$$\frac{1-Y(E,\theta)}{1-Y(E,\theta=0)} = \exp\left(\frac{\sin^2\theta}{2\cos^2\theta_{min}}\right)\cos\theta \qquad (4.1)$$

where θ_{min} is the incidence angle corresponding to the minimum deposition yield. The good agreement between simulation results and equation (4.1) confirms the weak effect of C^+ ion fluence on the deposition yield. Figure 4.5(b) shows a comparison between deposition yield results obtained from T-DYN simulations and TEM measurements. The film thickness at $\theta = 0°$ was used as a reference. From fitting the deposition yield data determined from the TEM measurements and using $\theta_{min} = 72.8°$, the yield rate at normal incidence $Y(E, \theta = 0)$ in equation (4.1) was found equal to 0.9835, which is slightly less than 0.9904 obtained from the T-DYN analysis. Figure 4.5(b) shows a good agreement between TEM and simulation results, except for large θ values. This discrepancy may be attributed to the lower true fluence of C^+ ions arriving at the sample surface for large incidence angles ($\theta > 80°$).

4.3.3 Incidence angle effect on film structure

Further insight into the incidence angle effect on film quality can be obtained from the XPS and AFM results presented below. Figure 4.6 shows typical XPS C1s core level peaks of a-C films deposited at incidence angles of 60° (Figure 4.6(a)) and 0° (Figure 4.6(b)) for deposition time fixed at 30 s, i.e., ion fluence equal to 4.5×10^{16} ions/cm^2. After performing a Shirley inelastic background subtraction, each C1s peak was fitted with five Gaussian distributions, namely C1s-1, C1s-2, and C1s-3 corresponding to sp^1, sp^2, and sp^3 C-C hybridizations, respectively, and C1s-4 and C1s-5 representing high-order C–O and C=O bonds, respectively. The binding energy of each carbon chemical state was assigned the peak energy of the corresponding Gaussian distribution. The sp^2 and sp^3 fractions are defined as the C1s-2 and C1s-3 distribution areas, respectively, divided by the sum of the C1s-2 and C1s-3 distribution areas.

Figure 4.7(a) shows XPS measurements of the binding energy of sp^3 and sp^2 carbon atom hybridizations in terms of the incidence angle. A shift in the binding energy is normally associated with the presence of an internal (intrinsic) stress, with a compressive (tensile) stress resulting in the decrease (increase) of the binding energy [Wan and Komvopoulos, 2007]. For $\theta < 45°$, the binding energies of both sp^2 and sp^3 hybridizations are close to those for $\theta = 0°$. However, the binding energy of sp^3 hybridization for $\theta = 60°$ is higher than that for $\theta = 0°$, indicating a lower compressive stress in the film. Experiments and Monte Carlo simulations have shown that sp^3 and sp^2 carbon bonds are usually under compression and tension, respectively [Robertson, 2002; Kelires, 2001]. Therefore, the lower compressive stress in the a-C film deposited at $\theta = 60°$ may be correlated to a lower sp^3 fraction. This is confirmed by the significant decrease in sp^3 fraction shown in Figure 4.7(b). Because of the strong dependence of hardness on sp^3 carbon atom hybridization and the small variation of the sp^3 fraction in the range $0° \leq \theta \leq 45°$, it may be inferred that the a-C films deposited at these incidence angles should exhibit similar hardness and wear resistance.

4.3.4 Incidence angle effects on film roughness

In addition to the mechanical properties of the a-C films, the surface roughness is also of high importance because it controls the probability of asperity-asperity interaction in low-flying-height HDDs. Higher friction and faster wear are normally encountered with increasing surfaces

roughness. For a two-dimensional surface profile y(x), the root-mean-square roughness R_q is defined as

$$R_q = \left[\frac{1}{n} \sum_{i=1}^{n} y_i^2 \right]^{1/2} \qquad (4.2)$$

where y_i represents the height of the i_{th} point of the surface profile from the mean plane (y = 0), and n is the number of height measurements. Figure 4.8 shows the a-C film roughness as a function of incidence angle. The R_q roughness of the Si(100) surface, measured after Ar$^+$ sputter cleaning, was found equal to ~0.143 nm. For small incidence angle ($\theta < 30°$), the roughness increased with the incidence angle due to the dominance of ion sputter etching resulting from the increase of the in-plane velocity of impinging C+ ions. Increasing the incidence angle above 30° led to the decrease in film roughness to a minimum value (~0.15 nm) at $\theta = 45°$, attributed to a balance between deposition and sputtering processes. For $\theta > 45°$, R_q increased with θ due to the dominance of sputtering. Despite the prevalence of different mechanisms in the three ranges of incidence angle shown in Figure 4.8, the film roughness was not affected significantly by the variation of the incidence angle.

The R_q roughness represents a statistical measurement of the average deviation of surface heights from the mean plane. Further insight into the film surface topography can be obtained by considering the higher moments of the surface height profile, such as skewness S and kurtosis K, defined as

$$S = \frac{1}{nR_q^3} \sum_{i=1}^{n} y_i^3 \qquad (4.3)$$

$$K = \frac{1}{nR_q^4} \sum_{i=1}^{n} y_i^4 \qquad (4.4)$$

Skewness is a measure of the lack of symmetry of the probability distribution of surface heights. A positive skewness implies a small fraction of asperities with heights above the mean height, whereas a negative skewness implies a surface topography dominated by valleys than asperities. Considering that the probability of asperity interaction is lower for S > 0 than for S < 0, significantly different tribological behaviors may be encountered with media surfaces possessing similar R_q but different S values. Obviously, S > 0 is preferred in ultralow-flying-height HDDs. The kurtosis is a measure of variance, i.e., it indicates how tightly the peaks (asperities) and valleys of the surface profile are relative to the mean height. For a normal distribution, S = 0 and K = 3. Figure 4.9 shows that, with the exception of $\theta = 15°$, the incidence angle did not affect the variance of the surface height distribution of the a-C films. However, the skewness results indicate that the most desirable film surface topographies were obtained for $\theta = 0°$ and 45°. Thus, considering the results shown in both Figure 4.8 and 4.9, it may be argued that, from a surface topography perspective, the optimum incidence angle in FCVA film deposition is 45°.

4.4 Conclusion

Ultrathin a-C films were deposited by the FCVA method at different incidence angles of energetic C^+ ions. Monte Carlo simulation results confirmed by TEM measurements showed that the a-C film thickness decreases with the increase of the incidence angle, while the deposition yield (rate) is independent of ion fluence, and varies with the incidence angle following a relationship derived from sputtering theory. XPS and AFM results demonstrated that the sp^3 fractions and topographies of a-C films deposited at incidence angles less than 45° were similar to those of films deposited at 0° incidence angle. Considering the incidence angle effects on the thickness, structure, and topography of the deposited a-C films, the optimum incidence angle for FCVA deposition was determined to be equal to 45°. The results of this study indicate that, depending on the C^+ ion fluence, a-C films of thickness only a few nanometers can be obtained by oblique (45° incidence angle) FCVA deposition.
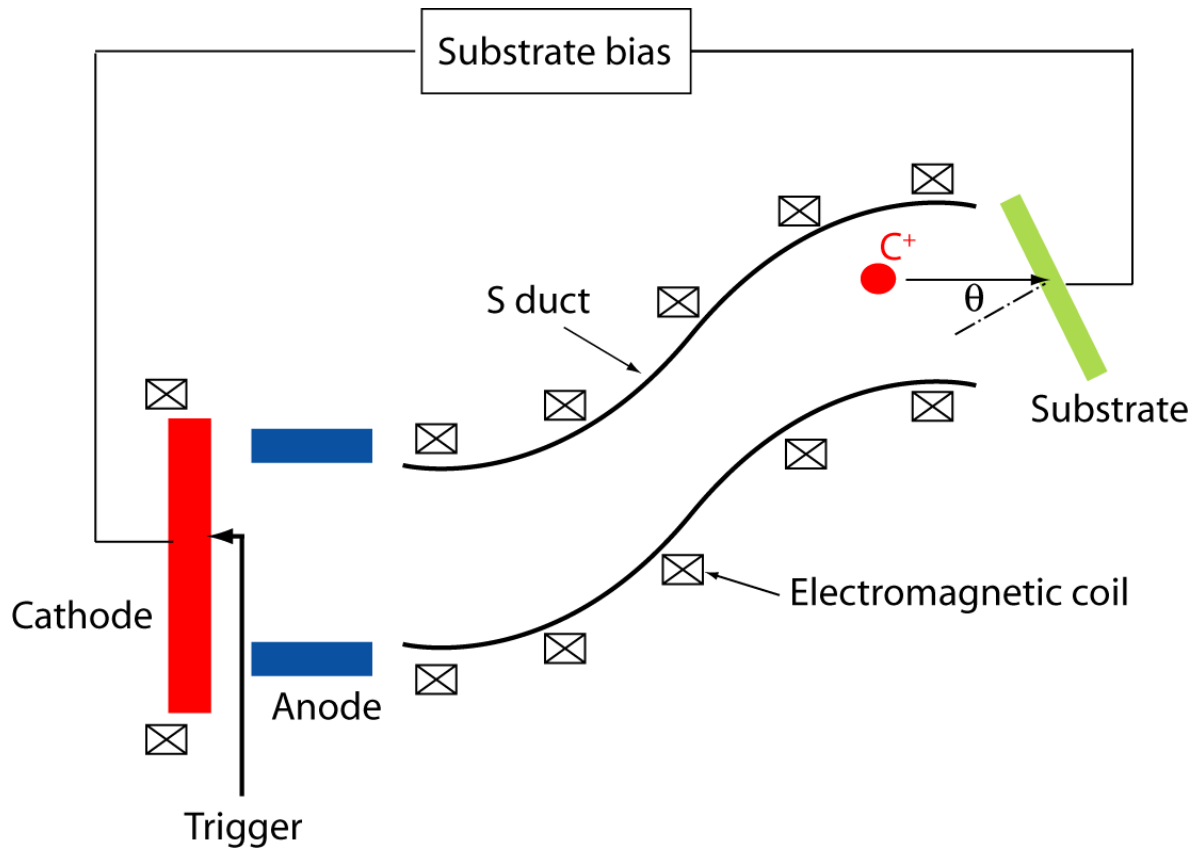
Figure 4. 1 Schematic of filtered cathodic vacuum arc (FCVA) system. The incidence angle θ of the C^+ ions impinging onto the substrate is the angle between the ion trajectory and the substrate normal.
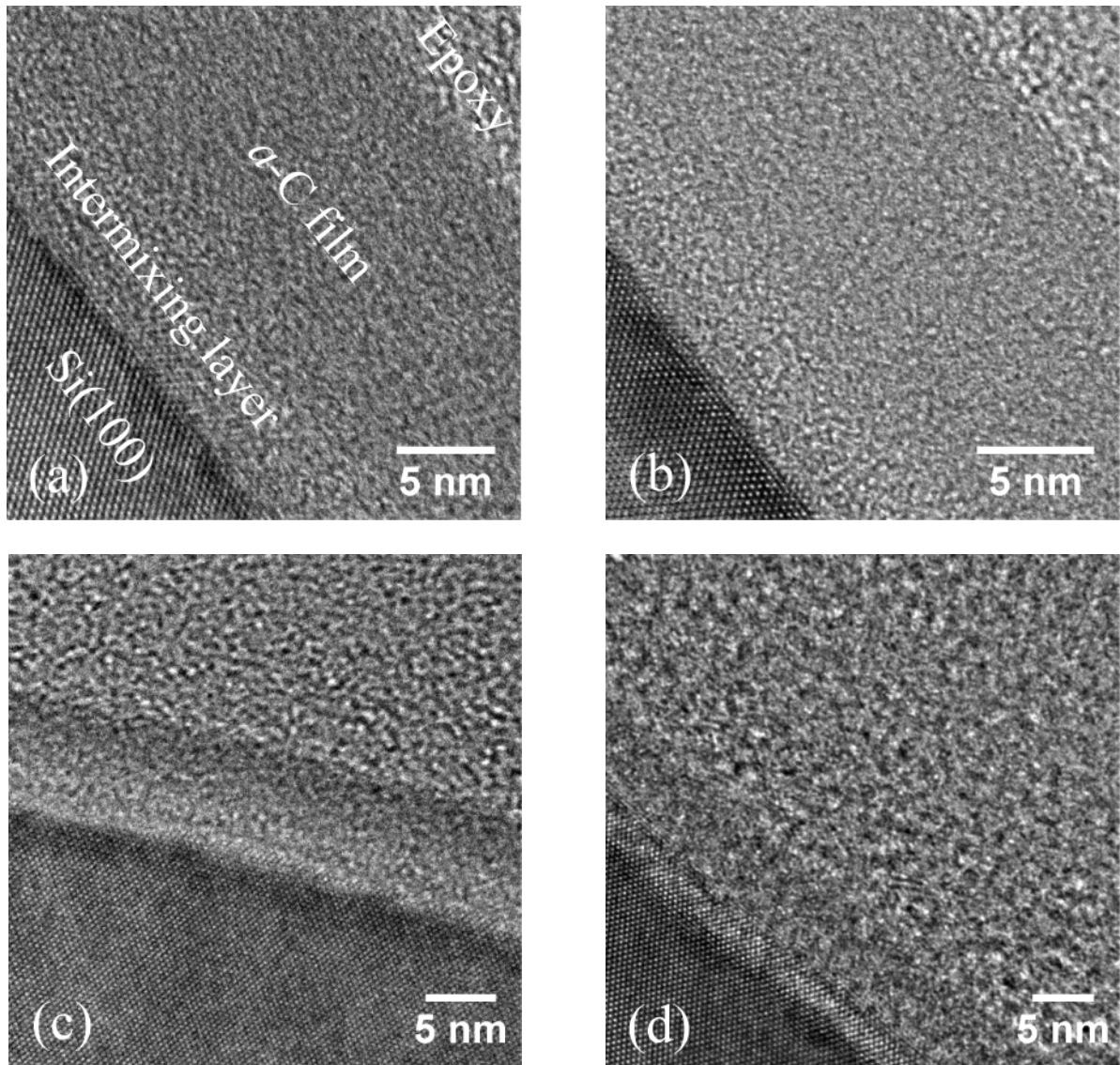
Figure 4. 2 Cross-sectional TEM images of carbon films deposited at an incidence angle equal to (a) 0°, (b) 45°, (c) 60°, and (d) 70°. Contrast and structure differences reveal the Si(100) substrate, intermixing layer, a-C film, and epoxy mounting material.
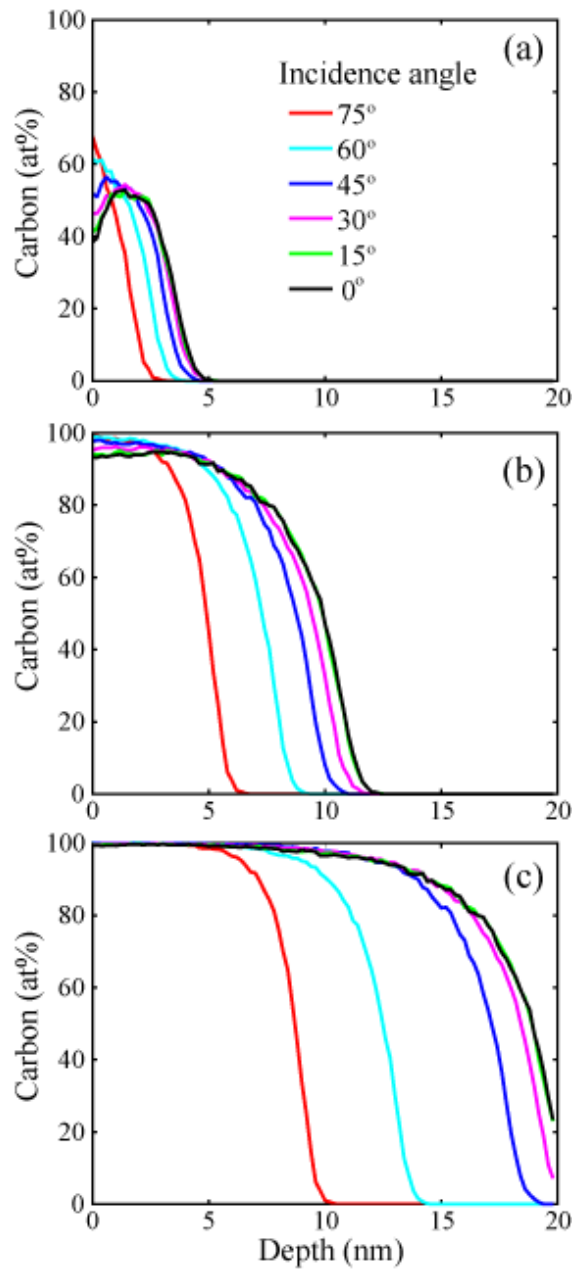
Figure 4. 3 Depth profiles of carbon films simulated with the T-DYN code for different incidence angles and C^+ ion fluence of (a) 0.9×10^{16}, (b) 4.5×10^{16}, and (c) 9.0×10^{16} ions/cm^2 and corresponding deposition time equal to 6, 30, and 60 s.
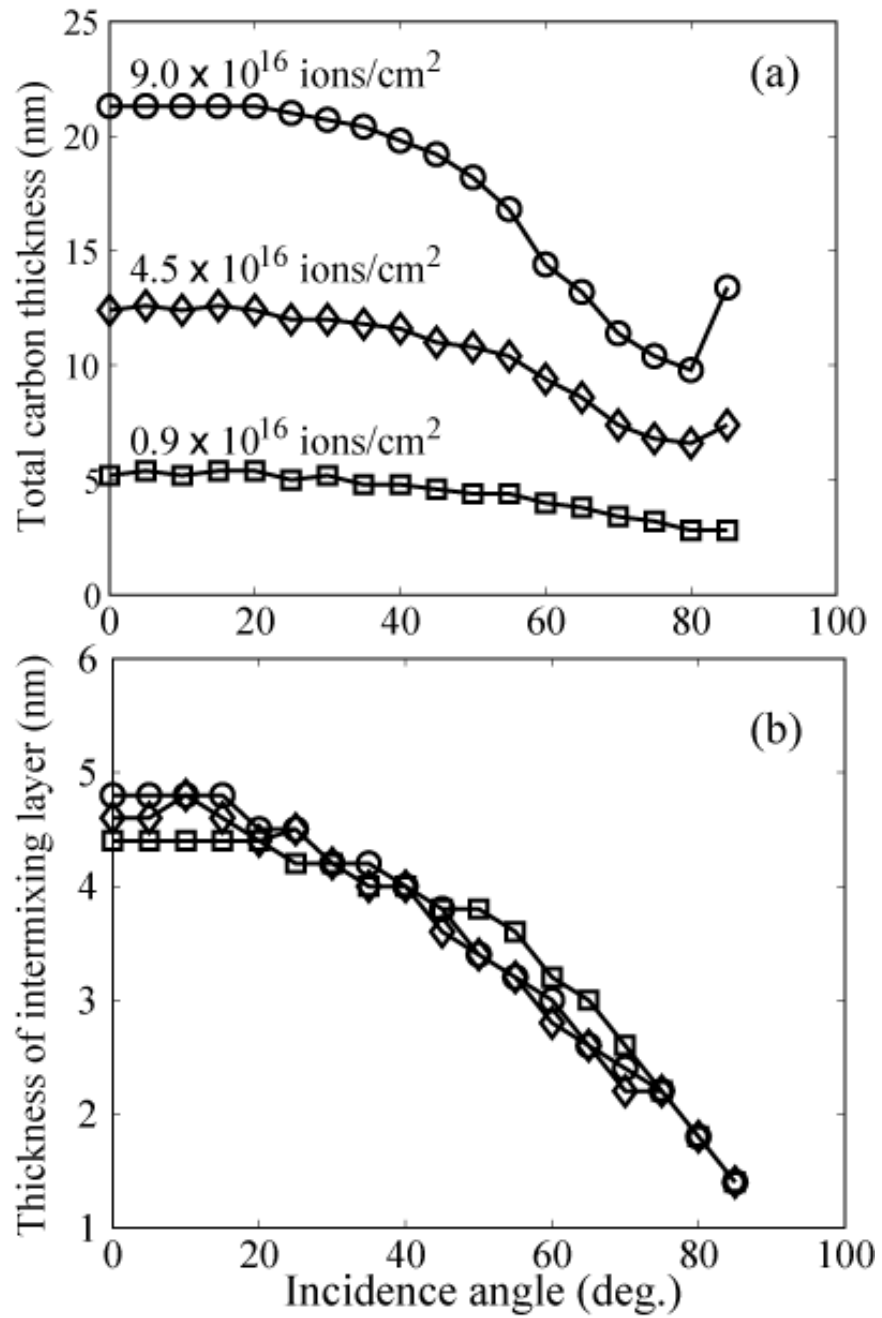
Figure 4. 4 (a) Total thicknesses of carbon and (b) thickness of intermixing layer obtained from T-DYN simulations for different incidence angles and C^+ ion fluence in the range of (0.9–9.0) × 10^{16} ions/cm².
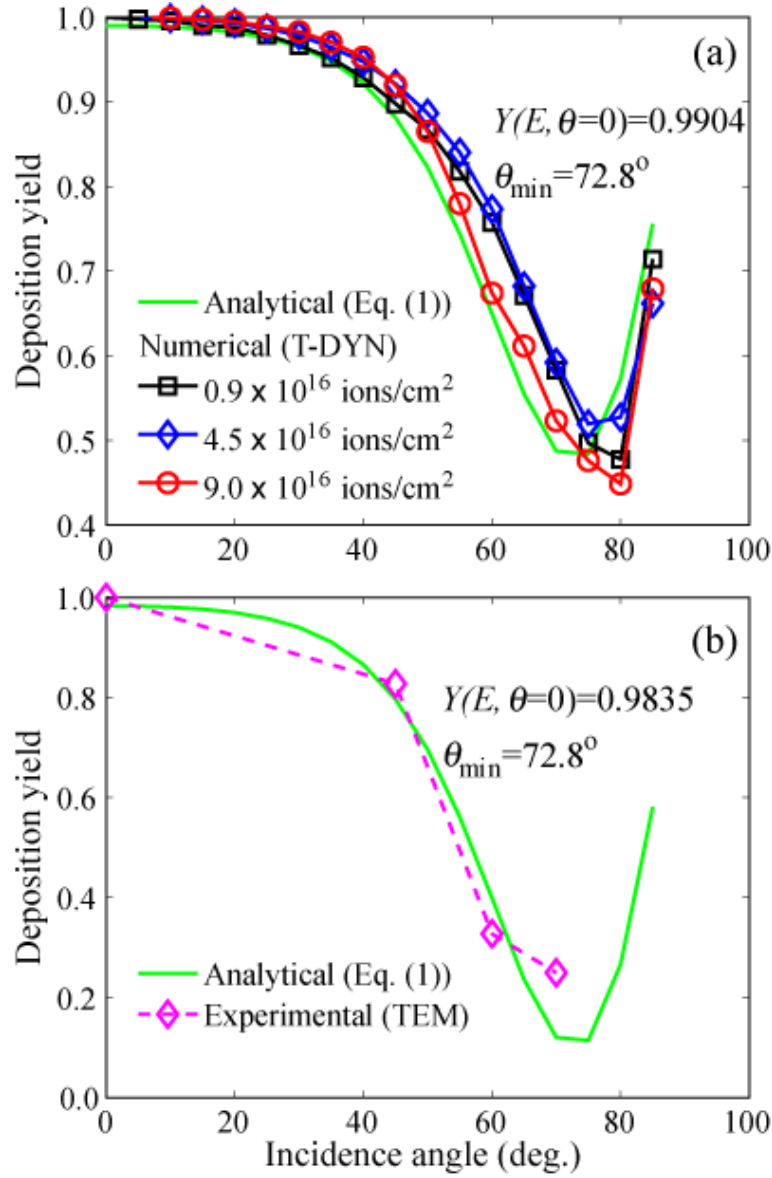
Figure 4. 5 Deposition yield versus incidence angle and ion fluence obtained from (a) T-DYN simulations and (b) TEM thickness measurements. Both simulation and experimental results are in good agreement with sputtering theory (Equation (4.1)).
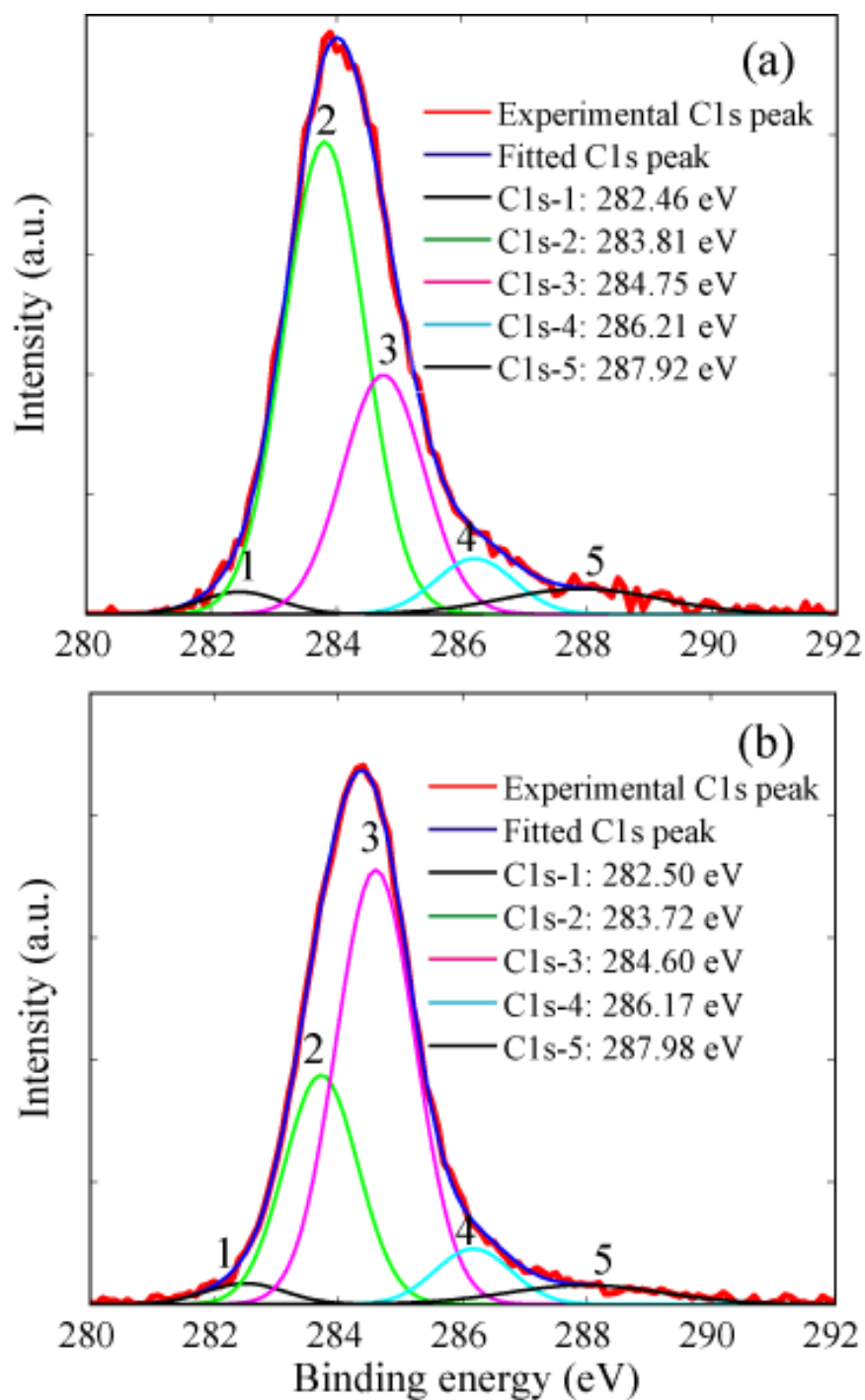
Figure 4. 6 XPS spectra of C1s core level peaks of *a*-C films for incidence angle equal to (a) 60° and (b) 0°, ion kinetic energy fixed at 120 eV (–100 V substrate bias), and deposition time equal to 30 s (ion fluence equal to 4.5×10^{16} ions/cm^2). After Shirley background subtraction, the XPS spectra were fitted with five Gaussian distributions denoted by C1s-1–C1s-5.
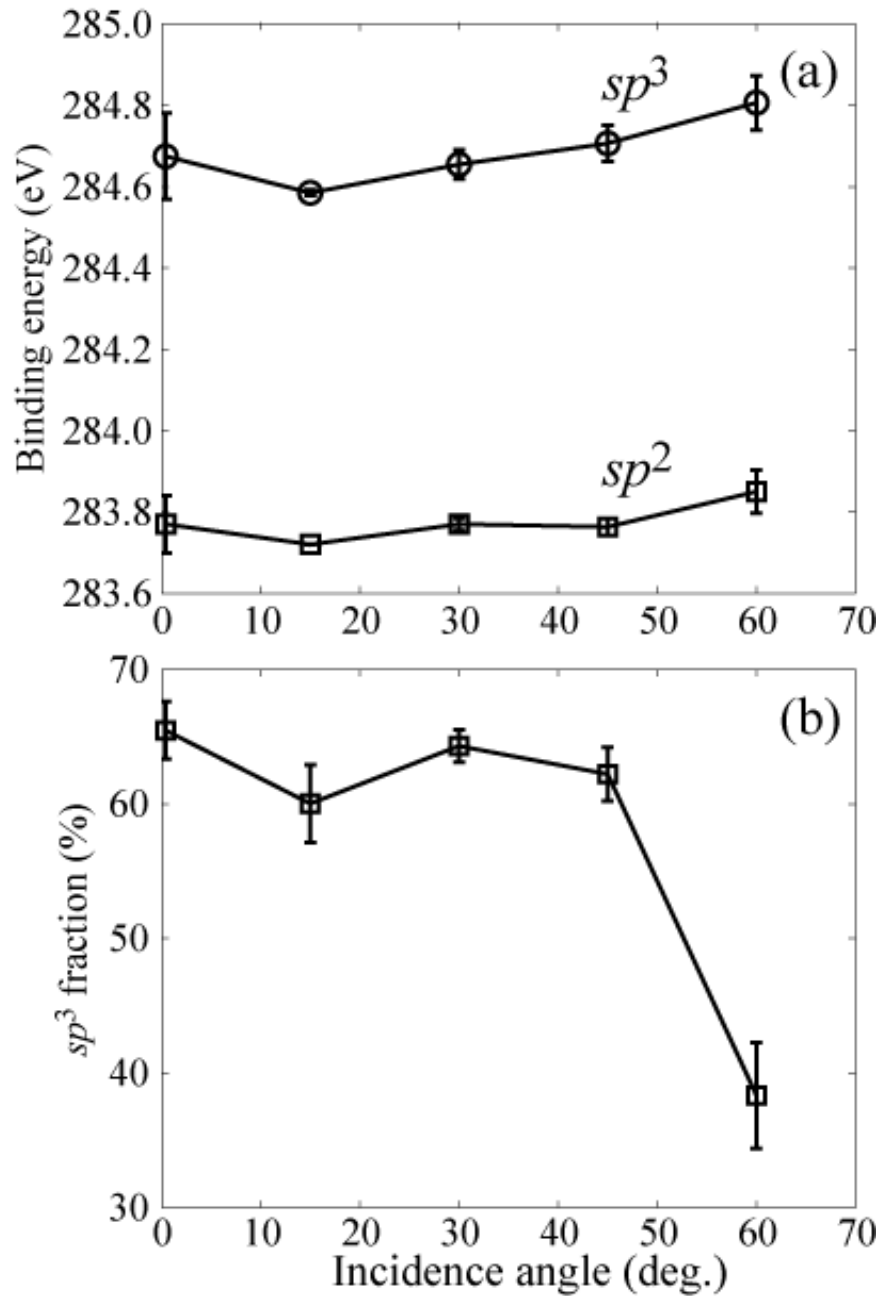
Figure 4. 7 Variation of (a) binding energy of sp^2 and sp^3 carbon atom hybridizations and (b) sp^3 fraction of a-C films with incidence angle. (The experimental conditions are the same as those in figure 4.6. Error bars indicate one standard deviation above and below the corresponding mean value.)
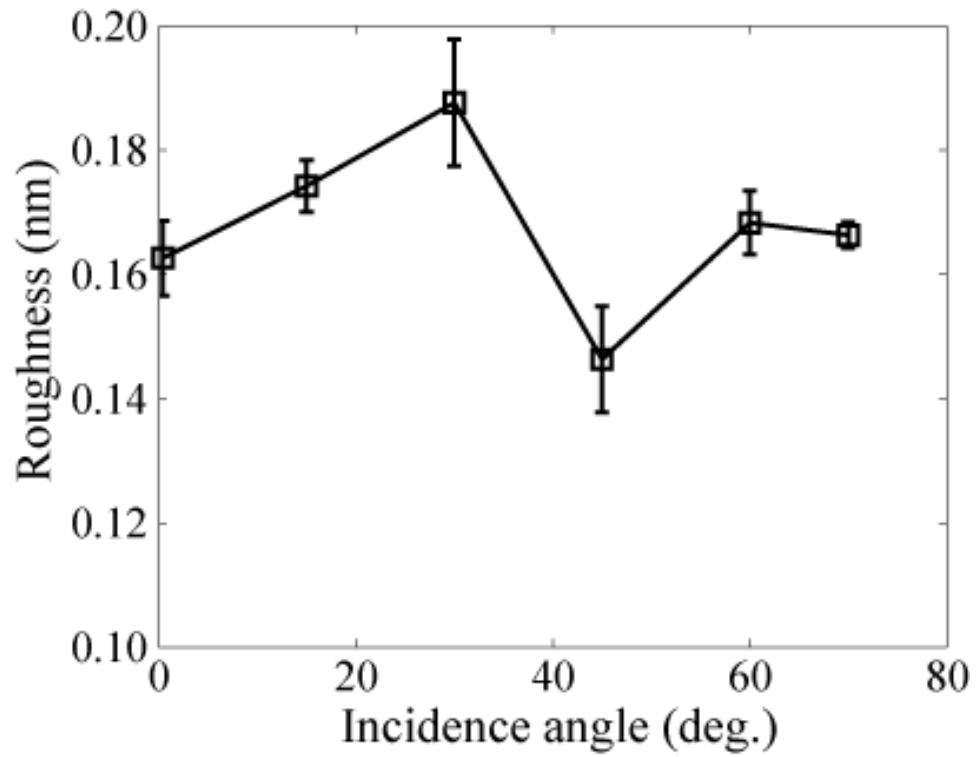
Figure 4. 8 Root-mean-square roughness versus incidence angle. (Error bars indicate one standard deviation above and below the corresponding mean value.)
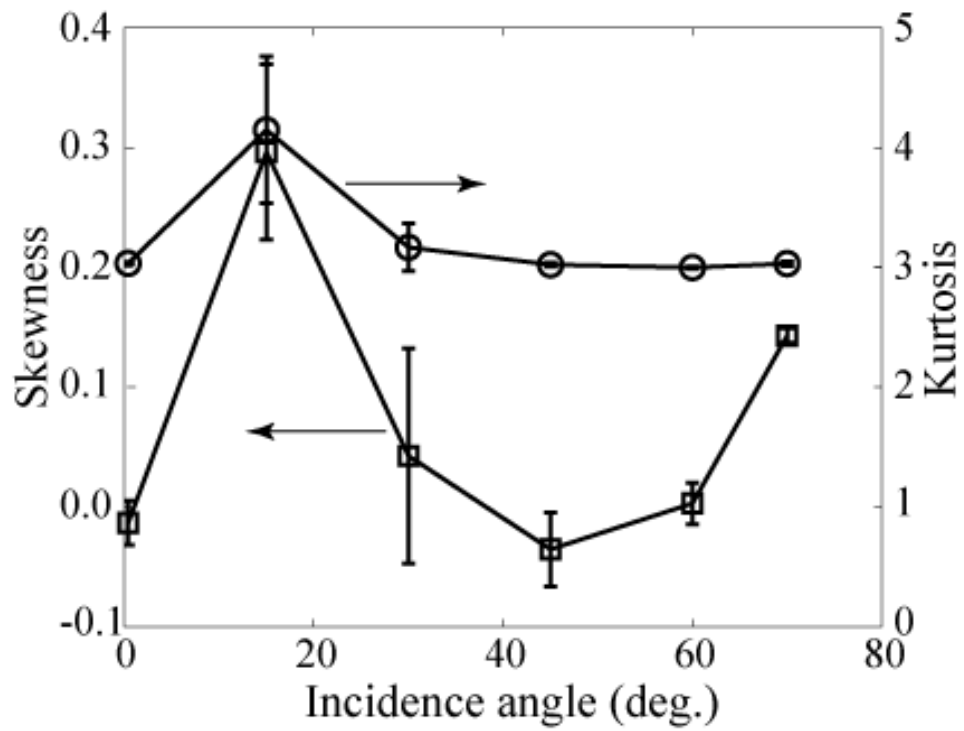
Figure 4. 9 Skewness and kurtosis versus incidence angle. (Error bars indicate one standard deviation above and below the corresponding mean value.)

Chapter 5

Thermal stability of amorphous carbon film under repetitive laser heating

5.1 introduction

Storage technology breakthroughs such as the advent of the giant magneto-resistive head and advances in thin-film deposition techniques have led to dramatic increases in the magnetic storage area density of hard-disk drives in recent years [Pan and Bogy, 2009]. Despite rapid evolutions in storage technologies, continuously increasing demands for larger storage capacities and lower production cost have raised the storage density barrier to levels on the order of 10 Tb/in^2 [Bandic and Victora, 2008]. However, such high storage densities cannot be achieved by the current storage technology due to fundamental problems associated with magnetic particle instability, signal-to-noise ratio, and read/write data rate caused by the superparamagnetic effect. Heat-assisted magnetic recording (HAMR) [Kryder et al., 2008] promises to circumvent above obstacles, which prevent extremely-high-density magnetic recording (EHDMR) to be realized. HAMR uses the optical power of a laser beam, effectively coupled with the magnetic medium of a rotating hard disk, to rapidly heat a track of the magnetic medium above its Curie temperature. The resulting instantaneous decrease in coercivity caused by the intense heat flux enables information to be stored in the form of single bits by the magnetic field of the read/write element, which is embedded at the trailing edge of the recording head.

The high magnetic anisotropy of FePt alloy [Wang, 2008] makes it a prime candidate magnetic medium for EHDMR applications. By using a near-field transducer integrated into the magnetic head, local heating of FePt above its Curie temperature can be induced by a laser beam of sub-100-nm resolution and high coupling efficiency [Challener et al., 2009; Stipe et al., 2011]. Although the Curie temperature of FePt nanoparticles depends strongly on their size and composition [Rong et al., 2007; Wang et al., 2008],the local temperature rise in the magnetic medium should be in the range of 200°C[Ikemoto et al., 2008] to 400°C [Challener et al., 2009; Rong et al., 2007] under HAMR conditions. However, despite the evidence that HAMR is an effective means of overcoming the superparamagnetic limit, the unknown effect of laser heating on the microstructure stability of the carbon overcoat is of great concern. Especially for ultra-thin *a*-C films, the effect of localized laser heating on the thermal stability of nanometer-thick carbon films is currently unknown.

Amorphous carbon (*a*-C) is the principal overcoat material of thin-film disks and magnetic heads, mainly because of its high hardness and excellent wear resistance. *a*-C films are generally characterized by varying percentages of trigonal (sp^2) and tetrahedral (sp^3) atomic carbon hybridizations. The fractions of sp^2 and sp^3 carbon–carbon bonding depend strongly on the process conditions of the particular deposition method. Elevated temperatures in HAMR may lead to stress relaxation and changes in atomic carbon hybridization [Grierson et al., 2010; Kalish et al., 1999], altering the *a*-C film composition and, in turn, degrading the corrosion and

tribological properties at the head/disk interface. Therefore, the thermal stability of *a*-C films used as overcoats in HAMR is of paramount importance.

Previous studies dealing with the thermal stability of nanometer-thick carbon overcoats were focused on the overcoat behavior under oxygen-free environments and temperatures between 350 and 1200°C. For example, rapid annealing at ~500°C in a nitrogen atmosphere of carbon films synthesized from methane by ion beam deposition resulted in hydrogen loss and graphitic recrystallization [Wu et al., 1992]. Also, *a*-C films produced by radio-frequency plasma decomposition of acetylene exhibited thermal instability at 390°C [Grill et al., 1990]. Contrary to the previous film deposition methods, tetrahedral *a*-C films deposited on Si(100) by filtered cathodic vacuum arc (FCVA) demonstrated composition stability during annealing up to 1100°C, above which, the film microstructure exhibited rapid sp^3-to-sp^2 transformation [Ferrari et al., 1999]. In addition to the composition stability, FCVA carbon films exhibit stable mechanical strength over a wide temperature range. For example, the hardness and elastic modulus of FCVA-synthesized a-C films have been reported to remain stable during thermal heating up to temperatures as high as 850°C [Tagawa and Tani, 2011]. Although the former studies indicate that FCVA produces thermally stable carbon films, laser heating in HAMR is localized and significantly more rapid (on the order of nanoseconds). This abrupt and localized heating differs significantly from uniform heating encountered in annealing studies as those mentioned above. In addition, the *a*-C film thickness in current disk-drives is equal to 3 nm or less, whereas the thickness of the *a*-C films examined in previous thermal annealing studies was larger than ~40 nm. Damage due to laser heating of 4.5-nm-thick carbon overcoats deposited by sputtering was indicated by a decrease in reflectivity, caused by a decrease in film density and surface roughening [Simone et al., 1997]; however, changes in the overcoat nanomechanical/tribological properties were not reported.

A review of the literature, including above publications, indicates that knowledge of the thermal stability of ultrathin *a*-C films under localized laser heating conditions is sparse. Therefore, the main objective of this study was to examine the effect of localized laser heating on the structural stability of ultrathin *a*-C films synthesized by chemical vapor deposition (CVD) and filtered cathodic vacuum arc (FCVA). Changes in atomic carbon hybridization and surface roughness of the films were examined by visible Raman spectroscopy and atomic force microscopy (AFM), respectively. Raman and AFM results of *a*-C films possessing different thickness synthesized by CVD and FCVA are presented below to determine which deposition process produces the most thermally stable carbon overcoats for HAMR and to elucidate the effect of film thickness on the thermal stability of FCVA *a*-C films.

5.2 Experimental procedures

5.2.1 Sample preparation

Since the focus of this study was the thermal stability of ultrathin *α*-C films for HAMR hard disks, 2.5-inch-diameter thin-film disks with glass substrates were used. The recording medium was a ~12nm FePt layer. The disks were coated with a ~4-nm-thick *a*-C film deposited by CVD and were never lubricated thereafter. CVD film deposition was performed at a temperature in the range of 90–120°C, using ethylene (C_2H_4) gas as precursor at a flow rate of 250–300 sccm. In all

of the CVD runs, the base and working pressures were fixed at ~1×10^{-7} and 2×10^{-2} Torr, respectively.

To deposit *a*-C films on the FePt magnetic medium of similar disks by the FCVA technique, hard disks coated with CVD-synthesized *a*-C films were loaded onto the substrate stage of a custom-made FCVA system [Zhang and Komvopoulos, 2008; Zhang and Komvopoulos, 2009(A); Zhang and Komvopoulos, 2009(B)], and the CVD carbon overcoat was sputter etched with a 500-eV Ar^+ ion beam produced by a 64 mm Kaufman ion source (Commonwealth Scientific, Alexandria, VA) under a working pressure of ~2.1×10^{-4} Torr. Under these sputter etching conditions, the CVD *a*-C film was completely removed after 2 min of Ar^+ ion bombardment, as evidenced by X-ray photoelectron spectroscopy full spectrum scanning. After cooling down for 5 min, the substrate holder was rotated by 90° to a position perpendicular to the carbon ion flux and *a*-C film deposition was initiated. The base pressure in the FCVA chamber was fixed at ~3×10^{-6} Torr, while the working pressure during deposition was <1×10^{-4} Torr. To ignite and maintain the arc discharge during deposition, the potential and current between the 99.99% pure graphite cathode and the anode were kept at 24 V and 89 A, respectively. A pulsed substrate bias voltage of –100 V and 25 kHz frequency was used in all FCVA depositions. These FCVA process conditions resulted in a deposition rate of ~0.3 nm/s. To achieve uniform sputter etching and deposition, the substrate holder was rotated at 60 rpm during both Ar^+ ion etching and film deposition.

Because of the thermal stability and known optical properties of silicon, p-doped Si(100) substrates coated with *a*-C films together with the exposed FePt magnetic medium of the sputtered disks were used to measure the film thickness with an ellipsometer (M-2000, J. A. Woollam Co., Lincoln, NB). The thickness of FCVA *a*-C films synthesized under identical chamber conditions and different deposition times was measured by cross-section transmission electron microscopy and was then used to calibrate the film thickness measured by ellipsometry. For comparison with the *a*-C films deposited by CVD and to examine the film thickness effect on thermal stability, *a*-C films of thickness equal to ~3.6 and ~0.9 nm were deposited on exposed FePt magnetic layers of hard disks under the above FCVA working conditions.

5.2.2 Laser thermal treatment

Each disk was mounted on a spindle rotating at 5400 rpm and was then exposed to a continuous-wave Vanadate laser beam of ~4 µm diameter and 20 W maximum power. The laser beam was traversed in the radial direction of the disks at increments of 9 µm per revolution to produce a 0.5-mm-wide annulus of partially overlapping spiral tracks. Each annulus consisting of overlapping laser-heated tracks was subjected to 610 successive heating cycles before it was examined with the Raman spectrometer. The total disk time is about 1 hour. Figure 5.1 shows the illustration of the laser heating experiment setup. Since the disk is rotating at a high speed and the laser heating spot size is very small, it is difficult to measure the in-situ temperature profile. In order to indicate the surface temperature, varying laser powers were tried to melt a Sn dot on the disk surface. Melting of the Sn dot on a disk surface at a laser power of 150 mW indicated that the surface temperature due to laser heating at this power was higher than the melting point of Sn (232°C). Thus, the laser power in this study was chosen to be in the range of 150–300 mW.

5.2.3 Microanalysis

Changes in the surface properties and roughness of the laser-heated a-C films were qualitatively examined with an optical surface analyzer (OSA) (Candela Instruments, San Jose, CA). The whole disk surface was spirally scanned, and all laser-heated tracks were marked for subsequent AFM and Raman analysis.

Surface topographies of the *a*-C films were examined with an AFM (Nanoscope III, Digital Instruments, Plainview, NY) operated in the tapping mode. AFM imaging was performed with Si tips of nominal radius of curvature <10 nm attached to microcantilevers of 5 N/m stiffness and 150 kHz resonant frequency. Images of 1×1 µm^2 areas obtained from the central region of each laser-heated annulus were used to calculate the arithmetic average roughness R_a of each film as a function of laser power. The R_a roughness of as-deposited *a*-C films was calculated from AFM images obtained from surface regions at distances equal to ~2 mm from the laser-heated annulus.

Raman spectroscopy is a standard nondestructive method for studying the carbon bonding structure. Films deposited on the FePt magnetic layer of hard disks were heated at different laser powers and their thermal stability was studied by visible (514.5 nm) Raman spectroscopy (WiRE^{TM}, Renishaw Raman Imaging Microscope, Hoffman Estate, IL) using a 514.5 nm Ar$^+$ ion laser focused to a spot of diameter <4 µm. Raman spectra were recorded in the range of 850–1950 cm^{-1} and background and noise were subtracted before fitting with two Gaussian distributions corresponding to *D* and *G* peaks, which are due to the in-plane bond-stretching vibration mode of sp^2 sites and the stretching and bending modes of sp^2 sites in aromatic rings [Robertson, 2002].

5.3 Results and discussion

5.3.1 Laser damage observed by optical method

Figure 5.2 shows OSA images of laser-heated tracks on disks with different *a*-C films. The applied laser power increases from ~150 mW at the inner track of radius equal to 13 mm to ~300 mW at the outer track of radius equal to 16 mm. The contrast intensity correlates with the extent of changes in surface properties, with higher contrast implying more significant changes. The hardly distinguishable tracks corresponding to the lowest laser power (150 mW) suggest that changes in the surface properties of the *a*-C films, if any, were marginal. Significant changes in the film surface properties occurred for laser power >150 and >250 mW in the case of the CVD film and thin (~0.9 nm) FCVA films, respectively. However, changes in the surface properties of the thick (3.6 nm) FCVA film appear to be significantly less pronounced, indicating that the thick FCVA film is more thermally stable than the thin FCVA film, which itself is more stable than the thicker CVD film.

5.3.2 Film structure changes revealed by Raman

Figure 5.3 shows typical Raman spectra of as-deposited *a*-C films, with characteristic *D* and *G* peaks centered at ~1350 and ~1550 cm^{-1}, respectively. The absence of a *D* peak from the spectrum of both FCVA films reveals the existence of a high fraction of sp^3 hybridization in these films, resulting in limited amount of π bonding from aromatic rings. Alternatively, the presence of a *D* peak in the CVD film spectrum indicates the dominance of π bonding.

Figure 5.4 shows that laser heating affected the Raman spectrum of each film differently. Increasing the laser power (heating) changed significantly the spectrum of the CVD film [Figure 5.4(*a*)]. However, the spectrum of the 3.6-nm-thick FCVA film [Figure 5.4(*b*)] shows a secondary effect of laser heating on film structure, especially for laser power ≤250 mW, indicating a much higher thermal stability of *a*-C films deposited by FCVA. The 0.9-nm-thick FCVA film [Figure 5.4(*c*)] shows significant changes at a laser power >250 mW. Since the *D* peak indicates the presence of aromatic rings and the *G* peak is mainly due to vibrations of all sp^2 sites in both chain and ring configurations, the increase in the *D* peak intensity is indicative of an increase in the sp^2 sites in the film [Ferrari and Robertson, 2002]. Therefore, the ratio of the intensity of the *D* peak to that of the *G* peak, $I(D)/I(G)$, can be used to obtain approximate estimates of the sp^3 fraction in the films.

The large shift of the *D* peak in the spectra of the *a*-C films deposited by CVD is associated with the conversion of sp^2 carbon configurations to less ordered aromatic rings. It is well-known that visible Raman of laser wavelength equal to 514.5 nm is 50–200 times more sensitive to sp^2 than sp^3 hybridization due to the resonance effect of visible photons and sp^2 sites [Gupta et al., 2003]. Therefore, the signal strength can be correlated with the amount of sp^2 hybridization. Consequently, the marked changes in the Raman spectra of the CVD film for laser power >150 mW and the thinner FCVA film for laser power >250 mW can be attributed to the evolution of sp^3-to-sp^2 transformation.

Figure 5.5(*a*) shows the effect of laser power (heating) on $I(D)/I(G)$, which may be presumed as indicative of the degree of carbon disorder in the film. As mentioned above, the *D* and *G* peaks were determined by curve fitting the Raman spectra with Gaussian distributions [Tai et al., 2009]. Because the presence of C–H bonding in the CVD film complicates the interpretation based on $I(D)/I(G)$, a comparison is made only for FCVA films. The higher $I(D)/I(G)$ of the as-deposited thin FCVA film indicates a relatively low sp^3 fraction. The sharp increase in $I(D)/I(G)$ of the CVD film for laser power >150 mW indicates a significant increase in the amount of disordered carbon, which could be related to carbon clustering. A correlation between *D*-peak intensity and degree of disordered carbon has been determined from *ab initio* Raman simulations [Castiglioni et al., 2001]. The trend for $I(D)/I(G)$ to increase in the high laser power range is much less pronounced for both FCVA films. Thus, the Raman results shown in Figure 5.5(*a*) indicate that FCVA-synthesized *a*-C films exhibit much higher thermal stability. In the case of the thin FCVA film, $I(D)/I(G)$ remains nearly constant for laser power >250 mW. This can be explained by considering the limited sp^3 bonding in the thin film and the existence of less carbon atoms, which saturated the conversion to sp^2 bonding. From the comparison of Raman results of the two FCVA films, it follows that the thermal stability decreases with the film thickness. A plausible explanation for this trend is that, for a given laser power, the energy absorbed per carbon atom increases with the decrease of the film thickness.

Figure 5.5(*b*) shows the effect of laser heating on the *G*-peak position of CVD and FCVA films. It has been reported that the decrease in the sp^3 fraction and the residual compressive stress correlate with the upward shift of the *G* peak [Chung et al., 2007; Shin et al., 2001]. In this study, the *G* peak of the CVD film shows significant red-shifting, whereas that of the thicker FCVA film shows marginal variation as a result of laser heating. The slight changes in both $I(D)/I(G)$ and *G* peak position of the FCVA films are attributed to carbon bond stretching effects due to the relieve of the residual compressive stress in the films. The temperature rise in the

laser-heated film enhances the carbon atom mobility, resulting in vigorous stretching of the atomic bonds that promotes residual stress relaxation and red-shifting of the G peak. Consequently, secondary changes in both $I(D)/I(G)$ and G peak position may be attributed to restricted bond stretching. The Raman results indicate that laser heating altered the structure of the CVD and thin FCVA films through sp^3-to-sp^2 transformation and sp^2 clustering. Thus, laser heating at a power >150 mW affected significantly the structure of the CVD film, contrary to the FCVA films, which exhibited much higher thermal stability over the entire laser power range examined in this study (250 and >300 mW for 0.9- and 3.6-nm-thick FCVA films, respectively).

5.3.3 Film surface topography

The evolution of the film surface topography (roughness) during laser heating provides another means of exploring the thermal stability of a-C films deposited by the two methods. Figure 5.6 shows the R_a roughness of CVD and FCVA films as a function of laser power. Figure 5.7 shows the topography evolution of CVD and FCVA films under different laser power treatment conditions. The thick FCVA film did not show any discernible changes in roughness and topography, contrary to the CVD and thin FCVA films which were both roughened as a result of laser heating, especially for laser power above a threshold level of 150 and 200 mW, respectively. The volume increase due to extensive sp^3-to-sp^2 transformation [Lucas et al., 1991] in the laser-heated CVD and thin FCVA films was restricted by the bulky FePt substrate, resulting in a compressive residual stress in these films. Thus, the significant roughening of the CVD film for laser power >150 mW is attributed to clustering induced by compressive stresses produced from atomic carbon rehybridization. The increased roughness of these a-C films enhances the likelihood of intimate contact of the head with the hard-disk surface and, in turn, the loss of data due to surface damage. The results shown in Figures 2–7 indicate that a-C films deposited by the CVD method are limited to HAMR heating conditions of laser power ≥150 mW.

5.4 Conclusion

The thermal stability of ultrathin a-C films synthesized by the CVD and FCVA methods was investigated by repetitively heating the films under different laser powers. Visible Raman spectroscopy showed that FCVA films possess superior thermal stability. CVD films exhibited atomic carbon rehybridization and structural change at laser powers >150 mW, whereas the thermal stability of FCVA films of similar thickness was not affected by laser heating even for the maximum laser power (300 mW) used in this study. Laser heating at powers >150 mW induced significant roughening of the CVD films, suggesting that a-C films synthesized by CVD are limited to HAMR conditions of relatively low laser power heating. FCVA films demonstrated a decrease in thermal stability with decreasing film thickness, which can be attributed to the higher thermal energy absorbed per atom. The high thermal stability of a-C films synthesized by FCVA suggests that these films are prime overcoat candidates for HAMR hard disks.

Table 5. 1 Laser repetitive heating experimental setup

Band	Start/Stop Radii (mm)	Power (mW)	Circumferential Pitch (µm)	Spinning velocity (rpm)	# of cycles
1	13-13.5	150	68	5391	610
2	14-14.5	200	73	5380	610
3	15-15.5	250	78	5372	610
4	16-16.5	300	84	5430	610
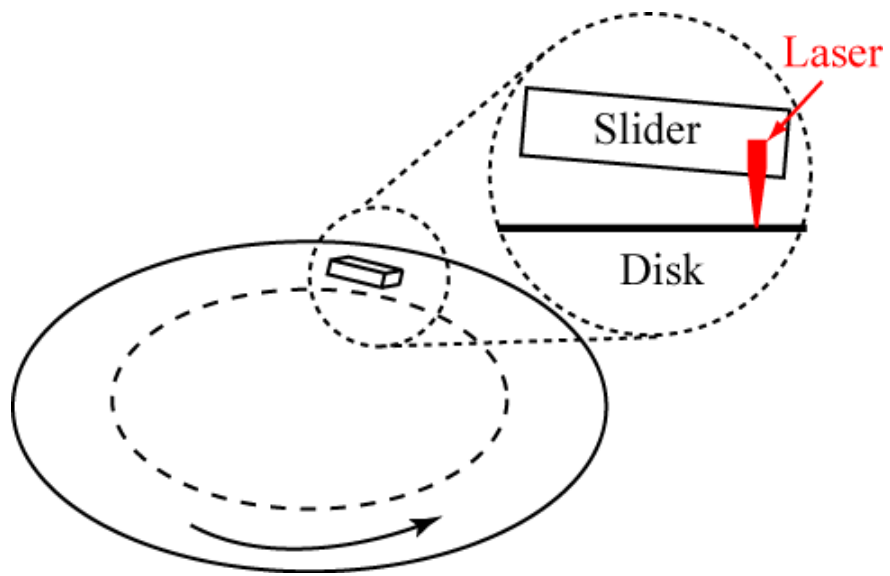
Figure 5. 1 Illustration of the experimental setup of laser heating.

150 mW —
200 mW —
250 mW —
300 mW —

(*a*) CVD film (3.6 nm)

150 mW —
200 mW —
250 mW —
300 mW —

(*b*) FCVA film (3.6 nm)

150 mW —
200 mW —
250 mW —
300 mW —

(*c*) FCVA film (0.9 nm)
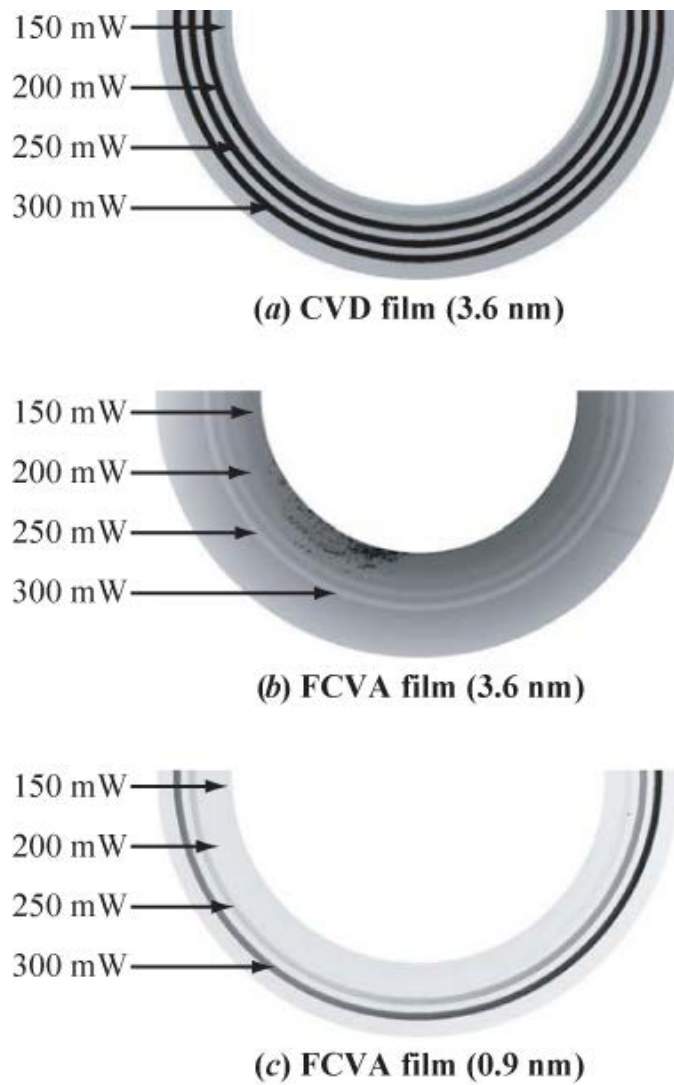
Figure 5. 2 Optical surface analyzer measurements of repetitively heated tracks on *a*-C film surfaces for different laser powers: (*a*) 3.6-nm-thick CVD, and (*b*) 3.6-nm-thick FCVA, and (*c*) 0.9-nm-thick FCVA *a*-C films.
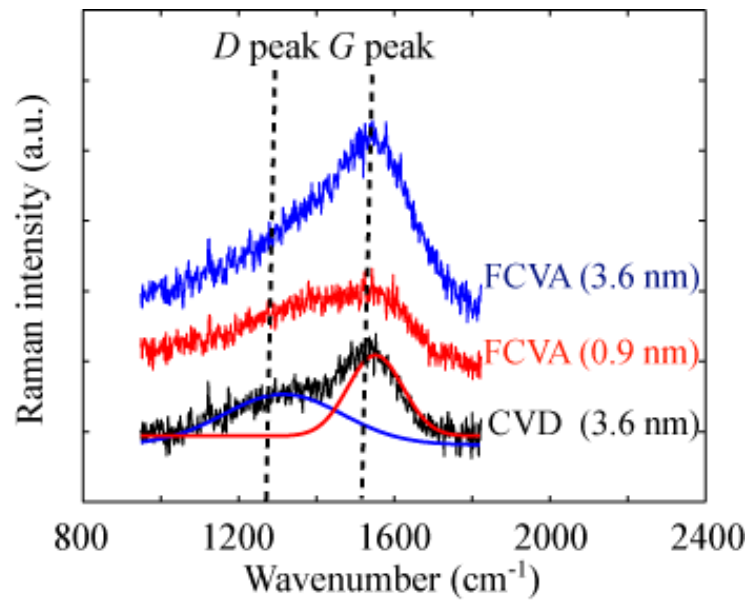
Figure 5. 3 Visible Raman spectra of as-deposited CVD and FCVA *a*-C films. (The spectra have been shifted upward for clarity. The two Guassian curves for fitting the spectrum of CVD film are given in thin solid lines)
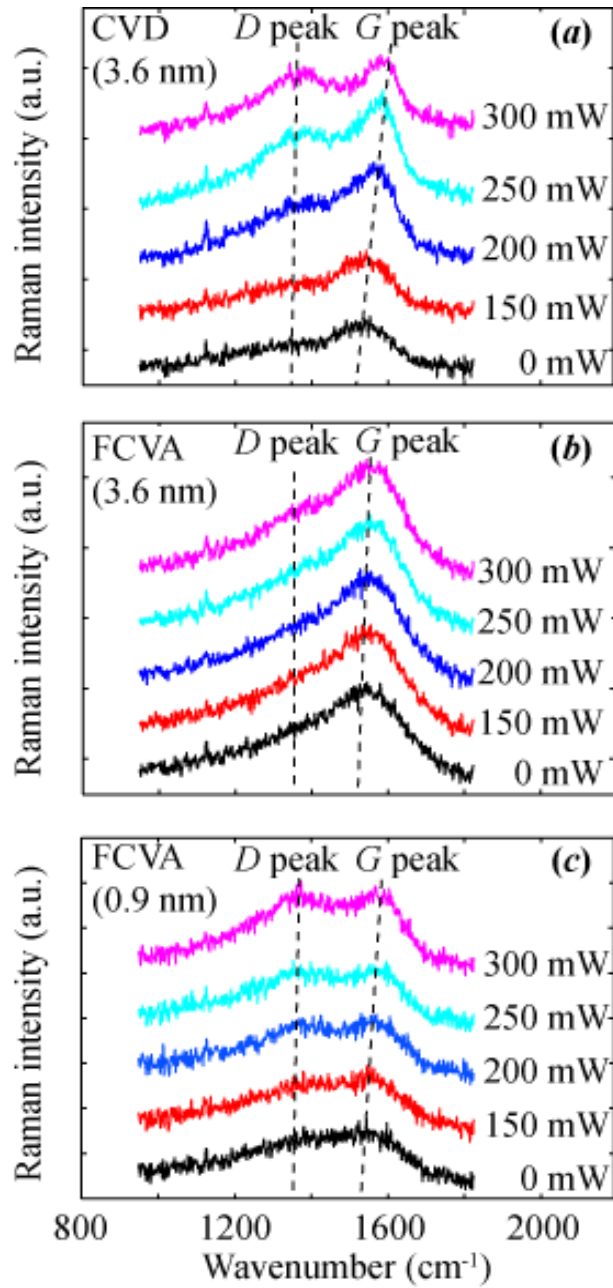
Figure 5. 4 Visible Raman spectra of *a*-C films obtained before and after heating at different laser powers: (*a*) 3.6-nm-thick CVD film, and (*b*) 3.6-nm-thick FCVA film, and (*c*) 0.9-nm-thick FCVA film. (The spectra have been shifted upward for clarity.)
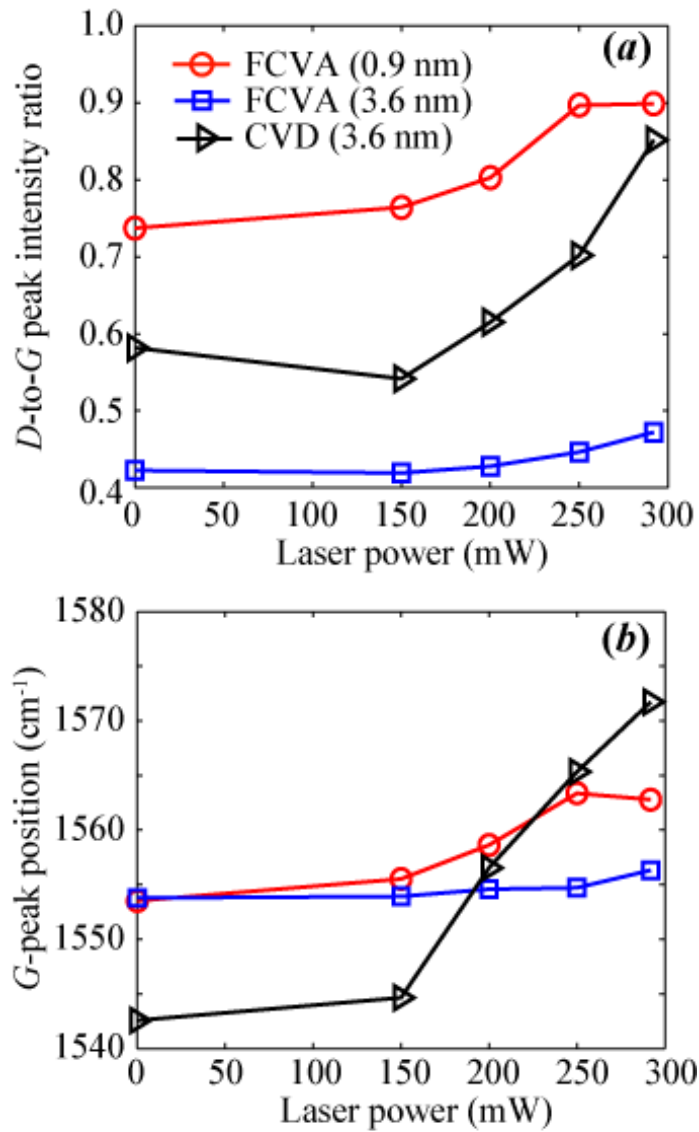
Figure 5. 5 (a) *D*-to-*G* peak intensity ratio and (b) *G* peak position of *a*-C films synthesized by CVD and FCVA versus laser power. (The error bars were not shown for clarity. The typical error range for D-to-G peak intensity ratio is 1.51% and for G peak position is 0.52%)
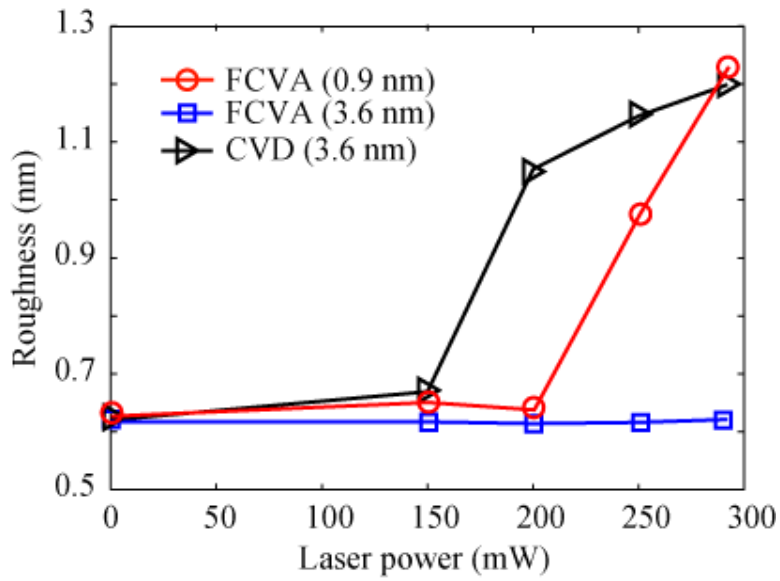
Figure 5. 6 Surface roughness of CVD and FCVA *a*-C films measured with an AFM after heating at different laser powers.
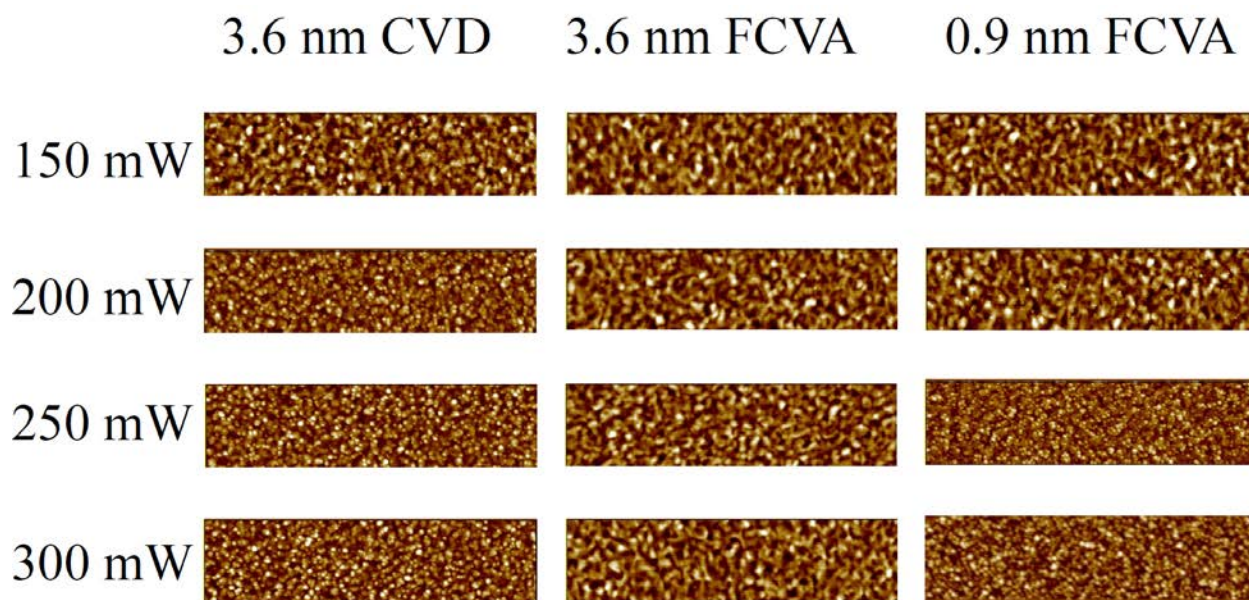
Figure 5. 7 AFM images of topography evolution of CVD and FCVA a-C films after heating at different laser powers.

Chapter 6

Thermal stability of hydrogenated amorphous carbon film investigated by rapid thermal annealing

6.1 Introduction

Thin films of amorphous carbon (a-C) are used in various technologies as protective overcoats because they exhibit chemical inertness, low friction, and high wear resistance [Tsai and Bogy, 1987; Grill, 1997; Robertson, 2002; Zhong et al., 2009]. In particular, ultrathin a-C films protect the magnetic medium of hard-disk drives (HDDs) against corrosion and mechanical wear caused by intermittent surface contact. Motivated by increasing demands for even higher storage densities, new deposition techniques such as filtered cathodic vacuum arc (FCVA) [Zhang and Komvopoulos, 2009(A); Zhang and Komvopoulos, 2009(B); Samad et al., 2011], pulsed laser ablation (PLD) [Chen et al., 2002], and magnetron sputtering [Li et al., 2002], which can produce continuous, ultrathin a-C overcoats were introduced in magnetic recording. Among the various factors affecting magnetic storage density such as improved technology of read heads, better servo-control mechanisms, and smaller magnetic spacing (thinner head and disk carbon overcoats), the development of fine-grained magnetic media has played a critical role in the remarkable increase of the storage capacity of HDDs. However, data storage in very small magnetic grains (bits) is inhibited by thermal fluctuations that can easily change the magnetization direction in each bit, resulting in permanent loss of information. Although this undesirable phenomenon (known as the superparamagnetic limit) can be offset by using highly anisotropic magnetic media, the increase of the magnetic anisotropy increases the magnetic field for bit polarization above applicable levels. A promising solution to this problem is heat-assisted magnetic recording (HAMR) [Bandic and Victora, 2008; Kryder et al., 2008; Challener et al., 2009; Stipe et al., 2010], which uses a tightly focused laser beam to heat and temporarily reduce the coercivity of magnetic nanodomains below that of the magnetic field applied by the head. Impulsive laser heating (typically <1 ns) [Challener et al., 2009] raises the temperature in the magnetic medium above its Curie temperature, i.e., the temperature above which the coercivity of the magnetic medium decreases significantly, thus enabling rapid data encoding by the magnetic field of the head. However, the intensive heating and rapid cooling raise a concern about the thermal stability of the protective carbon overcoat of HAMR disks. Therefore, knowledge of the effect of such rapidly applied thermal loadings on the integrity of the a-C overcoat is of great importance to the advancement of HAMR technology.

Our Previous study has shown that laser heating could cause degradation of the ultrathin a-C overcoats of current hard disks [Wang and Komvopoulos, 2011]. However, because of the very small laser spot (<100 nm in diameter when using a near-filed transducer) and short heating time in HAMR, it is difficult, if not impossible, to directly and accurately measure the temperature rise in the carbon film due to laser heating. Thus, temperature profiles for different laser heating conditions (e.g., laser power, laser spot size, heating time, and surface reflectivity) can only been obtained from numerical studies [Ding et al., 2011]. However, accurate estimation of the critical

temperature for *a*-C film degradation is critical to the success of HAMR, because it determines the maximum laser power for a given magnetic medium. While a high laser power is necessary for heating a highly anisotropic magnetic material above its Curie temperature, it is critical that the laser power does not induce thermal degradation of the *a*-C overcoat.

Thermal annealing is a common method for studying the thermal stability of *a*-C films. Numerous thermal annealing studies have been carried out with *a*-C films deposited by different methods [Kulikovsky et al., 2003; Takabayashi et al., 2008; Grierson et al., 2010; Akkerman et al., 1996; Grill et al., 1990; Ferrari et al., 1999; Diaz et al., 1996; Anders et al., 1997]. However, the films examined in these studies were significantly thicker than those used in current HDDs and the annealing time was on the order of several minutes. Initiation of hydrogen depletion and only sp^2 hybridization in radio-frequency sputtered 100-nm-thick *a*-C films annealed in vacuum have been reported to commence at a temperature of ~390 and 590 °C, respectively [Grill et al., 1990]. Tetrahedral amorphous carbon (*ta*-C) films of 70 nm thickness deposited by the FCVA method demonstrated stress relaxation and graphitization after annealing in vacuum at 600–700 °C and 1100 °C, respectively [Ferrari et al., 1999]. A dependence of the thermal stability of carbon films on the method of deposition, i.e., film composition and structure, has been observed in several studies [Kulikovsky et al., 2003; Grierson et al., 2010; Grill et al., 1990; Diaz et al., 1996]. In general, hydrogen-free *ta*-C films deposited by PLD [Grierson et al., 2010; Diaz et al., 1996] and FCVA [Anders et al., 1997; Chhowalla et al., 2000] exhibit higher thermal stability than other carbon films. While hydrogen-free *ta*-C films undergo graphitization during annealing in the temperature range of 700–900 °C [Ferrari et al., 1999; Diaz et al., 1996; Anders et al., 1997], hydrogenated amorphous carbon (*a*-C:H) films graphitize at a lower annealing temperature of ~600 °C [Grill et al., 1990] and are less stable because hydrogen depletion commences at about 300–500 °C [Grill et al., 1990; Conway et al., 1998; Wesner et al., 1983].

For a laser heating cycle of ~1 ns [Challener et al., 2009], the heating rate in HAMR is estimated to be higher than 10^{11} K/s. Although rapid thermal annealing (RTA) yields heating rates significantly lower than that encountered in HAMR, the total heating time of a given spot during a disk mean lifetime of ~ 10^6 hours [Schroeder and Gibson, 2007] is estimated to be on the order of seconds [Ma et al., 2012]. Thus, the RTA time is comparable to the total heating time of a given surface spot over the entire lifetime of the disk. Therefore, it may be inferred that if the *a*-C film does not undergo structural changes during RTA, its structural stability should be preserved under the HAMR laser heating conditions.

Consequently, the objective of the study in this chapter was to perform RTA experiments to elucidate the thermal stability of ultrathin *a*-C:H films used as protective overcoats in current HDDs. To apply rapid heating typical of HAMR, *a*-C:H films deposited by plasma-enhanced chemical vapor deposition (PECVD) were subjected to thermal annealing for <1 s, which is the minimum time achievable with the RTA equipment used in this study. Changes in the structure, carbon atom hybridization, thickness, and conductivity of the annealed *a*-C:H films were examined by visible Raman spectroscopy, x-ray photoelectron spectroscopy (XPS), x-ray reflectivity (XRR), and conductive atomic force microscopy (CAFM), respectively. Possible factors affecting the thermal stability of nanometer-thick *a*-C:H films deposited by PECVD are interpreted in the context of Raman, XPS, XRR, and CAFM results.

6.2 Experimental procedures

Ultrathin *a*-C:H films were deposited on both sides of 2.5-inch-diamter glass disks coated with a 96-nm-thick NiTa adhesive layer by the PECVD method using acetylene (C_2H_2) as a precursor. The density of the deposited films (obtained with the standard procedure used to determine the density from XRR measurements) was found to be ~2.1 g/cm^3, while the hydrogen content was estimated by the manufacturer to be ~40%. The *a*-C:H films were exposed to various temperatures in a thermal annealing equipment, which was purged with a gas mixture of 8000 sccm N_2 and 2000 sccm O_2 to simulate atmospheric conditions.

6.2.1 Rapid thermal annealing experiments

RTA experiments were performed in a heating chamber interfaced with an integrated computer control system (RTP-600xp, Modular Process Technology). The sample holder was supported by three cantilevers with a pin at their free end. Two symmetric rows of tungsten-halogen lamps (one above and one below the sample holder) were used to heat the sample. The chamber walls were covered by a reflective coating that reduces thermal loss and enhances the temperature uniformity in the chamber during annealing. The temperature at the sample surface was measured by a thermocouple placed in contact with the backside of the sample holder. The accuracy of the temperature measurement was within 2 °C. The heating rate during RTA was set at 105 ± 8.5 °C/s. To minimize the annealing time, the time to reach a certain maximum annealing temperature was kept as short as possible. Because of the short duration of heating, the set temperature slightly differed from the real temperature measured by the thermocouple. Figure 6.1(a) shows a typical temperature profile during RTA obtained from thermocouple measurements. Figure 6.1(b) shows the difference between set and measured temperature as a function of the set temperature. Hereafter, the temperature will always refer to that measured by the thermocouple.

6.2.2 X-ray photoelectron spectroscopy and X-ray reflectivity

Because of limitations in the XPS signal intensity and XRR thickness resolution (1 Å), 9.5-nm-thick *a*-C:H films were used in the graphitization and oxidation studies. Graphitization of *a*-C films deposited by different methods commences at a temperature between 590 °C [Grill et al., 1990] and 1100 °C [Ferrari et al., 1999]. However, as mentioned earlier, this information has been derived from long-term annealing studies. It is unclear if short-time annealing can also lead to graphitization. Therefore, to examine the carbon bonding configurations and detect graphitization, multiplex narrow-scan XPS spectra of the C1s core-level peak were obtained at an incident angle of 89º, measured from the sample surface. The XPS system (PHI Quantum 2000, Physical Electronics) used in this study is equipped with a monochromatic Al-Kα X-ray beam of 1486.6 eV energy and 5.7 eV work function. The energy resolution of the XPS system is 0.45 eV. XPS spectra were collected in the binding energy range of 280–295 eV under a vacuum of $<2 \times 10^{-8}$ Torr. After Shirley background subtraction, the broad C1s peaks were deconvoluted by five Gaussian distributions corresponding to sp^1, sp^2, and sp^3 hybridizations and high-order C–O and C=O bonds, respectively [Wan and Komvopoulos, 2007]. Binding energies of the Gaussian distributions corresponding to sp^2 and sp^3 hybridizations were set equal to 284.3 ± 0.2 and 285.2 ± 0.2 eV, respectively. The sp^3 fraction was obtained as the ratio of the distribution

area corresponding to sp^3 hybridization divided by the sum of the distribution areas corresponding to sp^2 and sp^3 hybridizations.

Film oxidation under the RTA conditions of this study was examined by comparing XRR film thickness measurements obtained before and after annealing. Specular XRR data were acquired with a diffractometer (X'Pert PRO, PANalytical) equipped with a 1.8-kW, fine-focus Co ceramic x-ray tube and a graded multilayer parabolic x-ray mirror, producing an ~100-µm-wide monochromatic Co-Ka beam having a divergence of <0.04°. The experimental data were analyzed with a commercial software [Wormington et al., 1999], which yields the density, roughness, and thickness of a layered structure by finding a best fit of the experimental data based on the method proposed by Parratt [Parratt, 1954] and Névot and Croce [Névot and Croce, 1980]. The uncertainty in the XRR thickness measurements was estimated to be about ±1 Å.

6.2.3 Raman spectroscopy

Changes in the film structure due to RTA were studied with a Raman spectroscopy system (InVia, Renishaw) equipped with an Ar laser of a wavelength equal to 514.5 nm. Raman spectra were recorded in the range of 950–1825 cm^{-1}. After substrate background noise subtraction, the spectra were first smoothed by a five-point Savitzky-Golay filter and then deconvoluted by two Gaussian distributions corresponding to the D and G peaks. For statistical analysis, Raman spectra were collected from at least three different surface locations of each film before and after RTA treatment.

6.2.4 Conductive atomic force microscopy

Current images of 3.4-nm-thick a-C:H films were obtained before and after annealing at 660 °C with a conductive AFM system (Dimension Icon, Veeco Instruments) equipped with a tunneling module for amplifying the current signal. Film conductivity measurements were obtained by applying a bias voltage of 0, 0.2, and 1 V to the sample surface through a contacting solid platinum tip (RMN-12PT400, Bruker) with a spring constant of 0.3 N/m and resonance frequency of 5 kHz. The deflection set point during imaging was set at 0.5 V.

6.3 Results and discussion

6.3.1 Carbon film graphitization and oxidation

At an elevated temperature, carbon films may exhibit graphitization due to transformation of sp^3 carbon atom hybridization to the thermodynamically more favorable sp^2 hybridization [Takabayashi et al., 2008; Grierson et al., 2010; Diaz et al., 1996]. This rehybridization decreases the film hardness and, in turn, its wear resistance. As stated earlier, previous studies dealing with the thermal stability of thick carbon films subjected to long-term thermal annealing have shown that graphitization occurs in the temperature range of 600–900 °C [Kulikovsky et al., 2003; Grierson et al., 2010; Grill et al., 1990; Gerrari et al., 1999; Diaz et al., 1996; Anders et al., 1997], depending on the type of carbon (deposition process). To examine whether graphitization occurred under the current RTA conditions, C1s core-level XPS spectra of 9.5-nm-thick a-C:H films were obtained before and after annealing at 660 °C. The similar C1s spectra of the as-deposited and annealed a-C:H films, shown in Figure 6.2, indicate a secondary effect of the RTA treatment. The sp^3 fraction before and after RTA treatment was found equal to about 8.45% and

10.15%, respectively. Because this small difference is within the error range of the curve fitting procedure, it may be inferred that RTA did not cause film graphitization.

To determine if carbon oxidation occurred during the RTA treatment, XRR measurements of the a-C:H film thickness were obtained before and after annealing at 660 °C. The average film thickness before and after annealing was found equal to 9.4 and 9.6 nm, respectively. Because this very small difference in film thickness is in the range of the experimental measurement error, it is concluded that RTA did not result in film oxidation. This is attributed to the very short duration of the RTA treatment, which limited oxygen diffusion and, in turn, chemical reaction between carbon and oxygen [Alam and Sun, 1993].

6.3.2 Changes in the carbon film structure

Raman spectroscopy is more sensitive to detect structural changes than XPS and XRR. In visible Raman spectroscopy, the photons preferentially excite the π states existing only in sp^2 hybridizations. Consequently, this technique can indirectly yield information about the sp^3 fraction. Figure 6.3 shows visible Raman spectra of 3.4-nm-thick a-C:H films obtained before (25 °C) and after (190–658 °C) RTA treatment. For clarity, the spectra shown in Figure 6.3 have been upwards shifted and the fitted Gaussian distributions corresponding to the D and G peaks are only shown for the as-deposited (untreated) film. In the Raman spectrum of the untreated a-C:H film, the D peak centered at 1347.5 cm^{-1} is assigned to the breathing modes of the sp^2 bonds of the aromatic rings, while the G peak centered at 1540.7 cm^{-1} is assigned to bond stretching of all carbon atom pairs in the sp^2 bonds of both aromatic rings and linear chains. Thus, the presence of the D peak in the Raman spectrum can be related to aromatic ring structures.

In visible Raman spectra, both the position and the intensity of the D and G peaks are affected by several factors, including the sp^2 cluster size, bond-length/angle disorder, sp^2 bonds in rings and chains, and sp^2/sp^3 ratio. The stretching modes of the C–H bonds are between 2800 and 3100 cm^{-1}, which is outside the range of Raman analysis. The bending modes of various hydrogen configurations are between 1300 and 1600 cm^{-1} and are superimposed to carbon-carbon bonds. Because visible Raman spectroscopy does not induce resonance of the bending modes, the effect of these modes is usually neglected in the analysis of the Raman spectra [Ferrari and Robertson, 2004; Ferrari and Robertson, 2000].

All of the visible Raman spectra shown in Figure 6.3 possess similar distributions, which is expected given the very short time of RTA conditions (<1 s at the maximum annealing temperature).The only obvious difference is the slight red-shifting of the G peak with the increase of the peak temperature of annealing. This shift may be attributed to $sp^3 \rightarrow sp^2$ rehybridization, the increase of the sp^2 cluster size, and the enhancement of sp^2 ordering in the rings [Ferrari and Robertson, 2004]. However, as shown by the XPS results (Figure 6.2), the RTA treatment did not affect the sp^3 content of the films. Thus, the shift of the G peak to higher wavenumbers may be attributed to the increase of the sp^2 cluster size and the sp^2 ordering in the rings.

Figure 6.4 shows the position and the full width at half maximum (FWHM) intensity of the G peak and the D-to-G peak intensity ratio I(D)/I(G) versus the peak temperature of annealing. All plots indicate the existence of a critical temperature of about 400–450 °C, above which

significant structural changes occurred in the films. As shown in Figure 6.4(a), red-shifting of the G peak was greatly enhanced by the increase of the peak temperature of annealing above ~450 °C, suggesting a significant increase of the sp^2 fraction, sp^2 cluster size, chain length, and sp^2 bond ordering in the rings [Ferrari and Robertson, 2004; Ferrari and Robertson, 2000]. However, because the XPS results (Figure 6.2) do not reveal any discernible changes in the sp^3 fraction after annealing, the significant red-shifting of the G peak above the critical temperature of annealing may be attributed to the increase of the sp^2 cluster size and the sp^2 bond ordering in the rings.

A continuous decrease of the FWHM of the G peak with increasing bond ordering has been observed in previous studies [Ferrari and Robertson, 2004; Ferrari et al., 2003]. The FWHM of the G peak can also be correlated with the sp^2 cluster size. In particular, for visible excitation and cluster sizes less than 100 nm, the FWHM decreases almost linearly with increasing sp^2 cluster size [Ferrari et al., 2003]. Figure 6.4(b) shows that the FWHM of the G peak decreases almost linearly with the annealing temperature above ~450 °C, suggesting an increase in sp^2 cluster size and the occurrence of carbon atom ordering in the film.

The I(D)/I(G) ratio also correlates with the sp^2 cluster size [Orwa et al., 2004]. For example, the relationship I(D)/I(G) = 44/L_a, where L_a is the in-plane crystallite size (in Ångstroms), has been reported to hold in the range of 25 Å < L_a < 3000 Å [Knight and White, 1989]. For much smaller cluster sizes, such as those in the present a-C:H films, I(D)/I(G) is proportional to the probability of a six-fold ring existing in a cluster [Ferrari and Robertson, 2004], i.e., proportional to the cluster area L_a^2. Consequently, the increase of the I(D)/I(G) ratio with the annealing temperature, shown in Figure 6.4(c), may be attributed to the increase of the sp^2 cluster size during RTA treatment at elevated temperatures (>450 °C).

A possible reason for the increase of the sp^2 cluster size during annealing is the depletion of hydrogen. Annealing of hydrogenated ta-C films in vacuum causes hydrogen depletion via the formation of molecular H_2 at local interstitial sites, rather than hydrogen diffusion through the film, followed by H_2 effusion to the film surface [Conway et al., 1998]. Hydrogen depletion from plasma-deposited a-C:H films commences at a relatively low temperature (~390 °C) [Grill et al., 1990]. The low density and extremely small thickness (3.4 nm) of the a-C:H films examined in this study were conducive to H_2 effusion to the surface. Hydrogen depletion may lead to carbon-carbon bond restructuring, accompanied by an increase of the sp^2 cluster size [Ferrari and Robertson, 2004]. Although C–H modes do not affect the position and intensity of the D and G peaks, carbon structure changes due to variations in the hydrogen content can be captured by visible Raman spectroscopy.

The G-peak positions may be affected by mechanical strain or stress relaxation in the annealed films. However, under the present RTA conditions, the a-C:H films were uniformly heated for a very short time without being constraint. In addition, contrary to other film deposition methods (e.g., FCVA and PLD) using energetic carbon ions or atoms as film precursors, the residual stress in a-C films deposited by PECVD is relatively low [Bhushan, 1999]. Considering the aforementioned factors and the extremely small thickness of the studied a-C:H films, it may be inferred that intrinsic (residual) stress effects on the G-peak position (Figure 6.3 and 6.4) were insignificant.

6.3.3 Carbon film conductivity

AFM measurements of the film conductivity provided further insight into the thermal stability of the *a*-C:H films. Figure 6.5 shows 500 × 500 nm CAFM images of 3.4-nm-thick *a*-C:H films obtained before (left column) and after (right column) annealing at a peak temperature of 660 °C. During CAFM imaging, the sample was grounded and the tip was biased by a voltage of 0. 0.2., and 1.0 V. Material property differences between the AFM tip and the *a*-C:H film yield an electric potential difference even in the absence of a bias voltage [Figs. 5(a) and 5(d)]. Thus, zero-voltage CAFM imaging provides a reference for images obtained for a bias voltage of 0.2 V [Figure 6.5(b) and 6.5(e)] and 1.0 V [Figure 6.5(c) and 6.5(f)]. The relatively low voltage allows for the identification of the highly conductive domains in the film. Table 6.1 shows the root-mean-square current versus applied bias voltage for as-deposited and annealed 3.4-nm-thick *a*-C:H films. For a given bias voltage, the CAFM images shown in Figure 6.5 and the data given in Table 6.1 show that the annealed *a*-C:H films produced relatively lower current intensities than the as-deposited films, indicating a detrimental effect of RTA on film conductivity. The electrical conductivity of the *a*-C films can be described by a conducting electron channel model [Liu and Benstetter, 2005]. Thus, the reduced electrical conductivity of the annealed *a*-C:H films may be attributed to breakdown of the conductive channels through the film thickness due to the depletion of hydrogen.

Variations in the electron conduction intensity may be attributed to conductive sp^2 nanoclusters (bright spots) distributed in a nonconductive sp^3 network (dark domains). The bright spots in the CAFM images of the annealed films [Figure 6.5(d)–6.5(f)] are larger than those in the CAFM images of the as-deposited films [Figure 6.5(a)–6.5(c)]. Since electron conduction occurs via sp^2 carbon bond configurations, the larger conducting spots observed in the CAFM images of the annealed *a*-C:H films reveal the presence of larger sp^2 clusters, which is consistent with the Raman spectroscopy results.

6.4 Conclusion

Ultrathin *a*-C:H films deposited by PECVD were subjected to rapid (<1 s) thermal annealing to peak temperatures up to 660 °C in atmospheres of 80% N_2 and 20% O_2 to simulate the ambient environment in HAMR. Raman spectra demonstrated significant structural changes in 3.4-nm-thick *a*-C:H films above a critical peak annealing temperature of ~400–450 °C. XRR and XPS measurements did not reveal discernible changes in the film thickness and the sp^3 content due to RTA, indicating that oxidization and graphitization of the *a*-C:H films was either secondary or negligible during RTA.

Red-shifting and the decrease of the FWHM of the G peak with the increase of the maximum annealing temperature above 450 °C suggested that hydrogen depletion, the increase of the sp^2 cluster size, and the enhancement of carbon network ordering are the most likely factors affecting the structural stability of the *a*-C:H films. Although it is extremely difficult to quantify changes in the mechanical properties of such ultrathin films, the structural changes observed in this study yield indirect insight into the impact of RTA on the mechanical integrity of these films. For instance, an increase in the sp^2 cluster size may be interpreted as an increase in the film heterogeneity and, presumably, porosity, which are detrimental factors to the wear resistance of the *a*-C:H films.

The duration of a heating cycle in HAMR is on the order of a few nanoseconds. This implies that the RTA treatment used in the present study was more severe than that in HAMR. Consequently, it may be argued that the structural stability of a-C:H films deposited on current hard disks by PECVD should be preserved, provided they are not heated to temperatures above ~400 °C during the read/write operation process of HAMR disk drives.

Table 6. 1 Current versus bias voltage applied to the AFM tip for as-deposited and annealed 3.4-nm-thick a-C:H films.

Tip bias voltage (V)	Root-mean-square current (pA)	
	as-deposited film	annealed film (660 $^{\circ}$C)
0.0	0.648	0.512
0.2	93.7	71.8
1.0	1434	1249
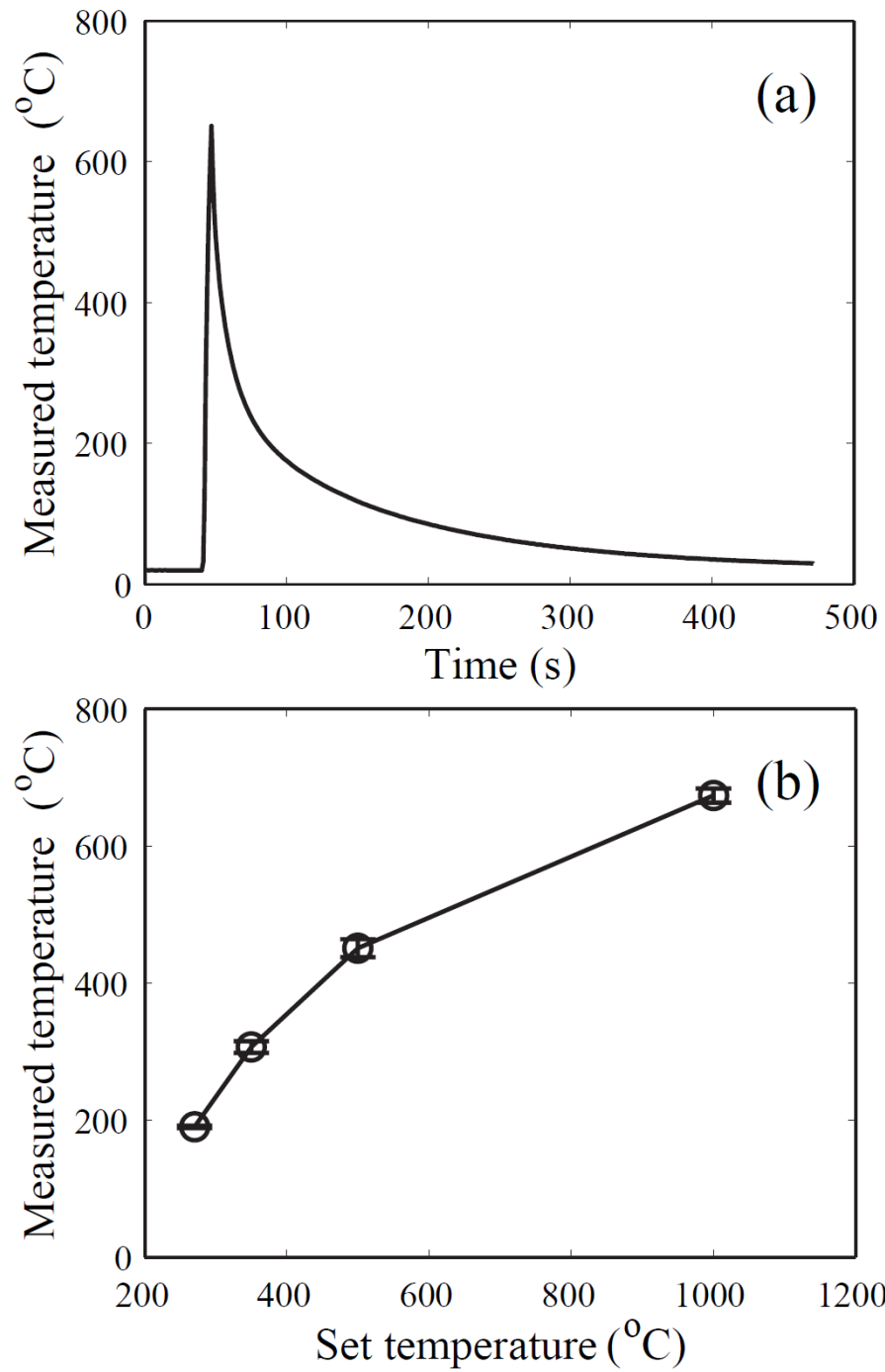
Figure 6. 1 (a) Typical temperature profile of the RTA treatment used in the present study and (b) measured versus set (maximum) RTA temperature.
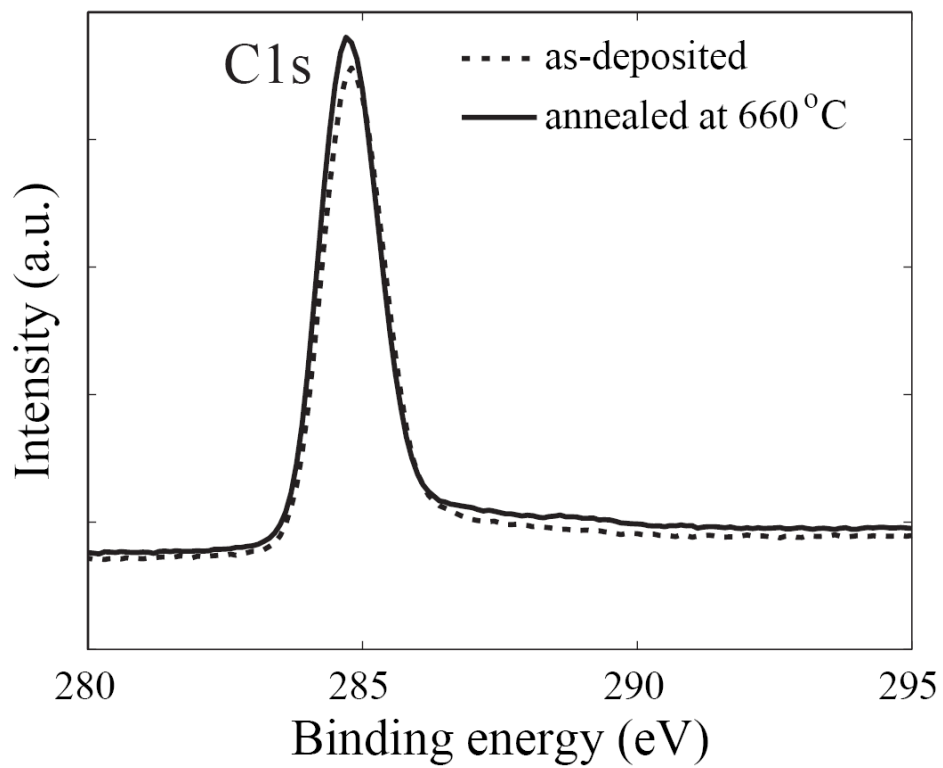
Figure 6. 2 XPS C1s core-level peak of 9.5-nm-thick *a*-C:H films obtained before and after RTA treatment at a maximum temperature of 660 °C.
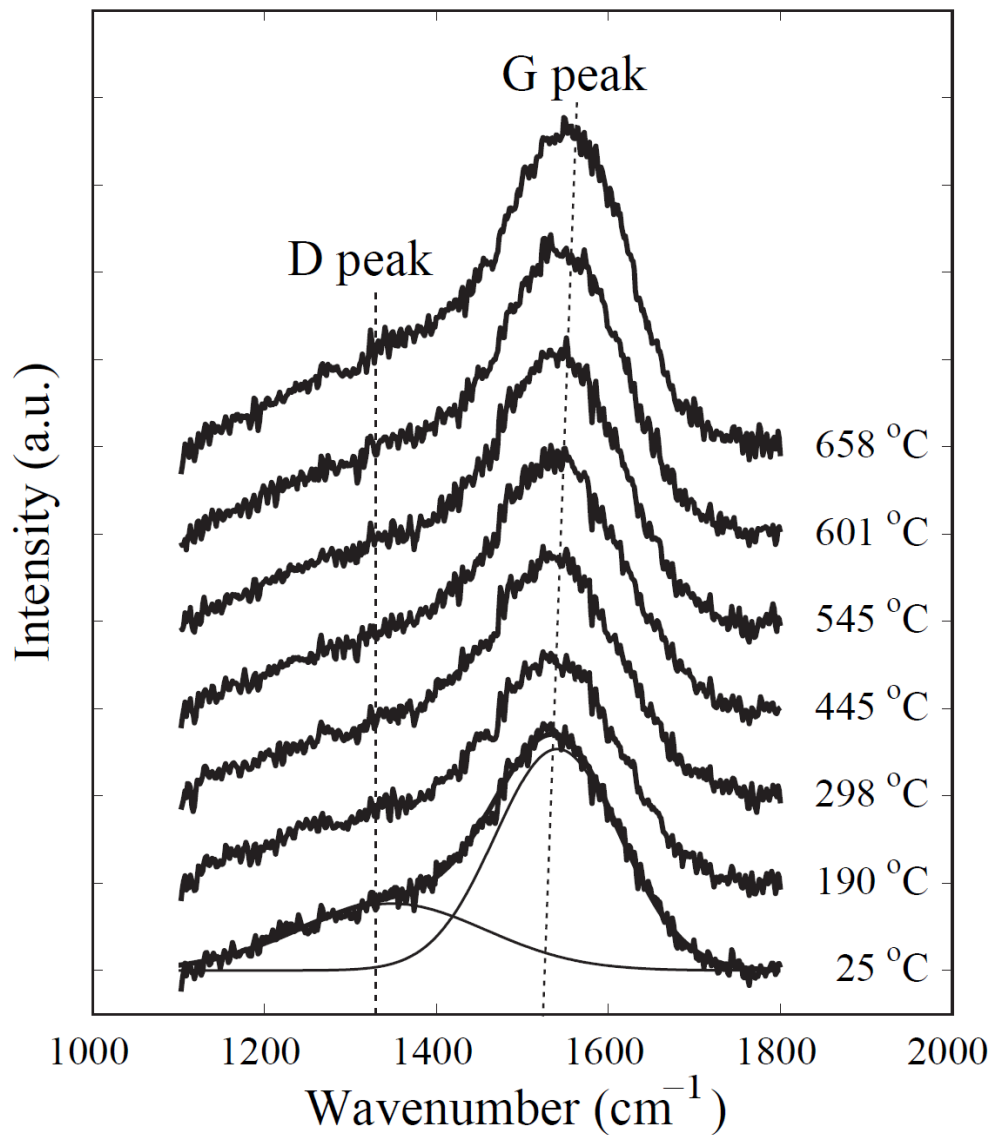
Figure 6. 3 Visible Raman spectra of 3.4-nm-thick *a*-C:H films obtained before (25 °C) and after RTA treatment at a maximum temperature in the range of 190–658 °C. (For clarity, the spectra have been shifted upwards and the fitted Gaussian distributions corresponding to the D and G peaks are only shown for the 25 °C spectrum.)
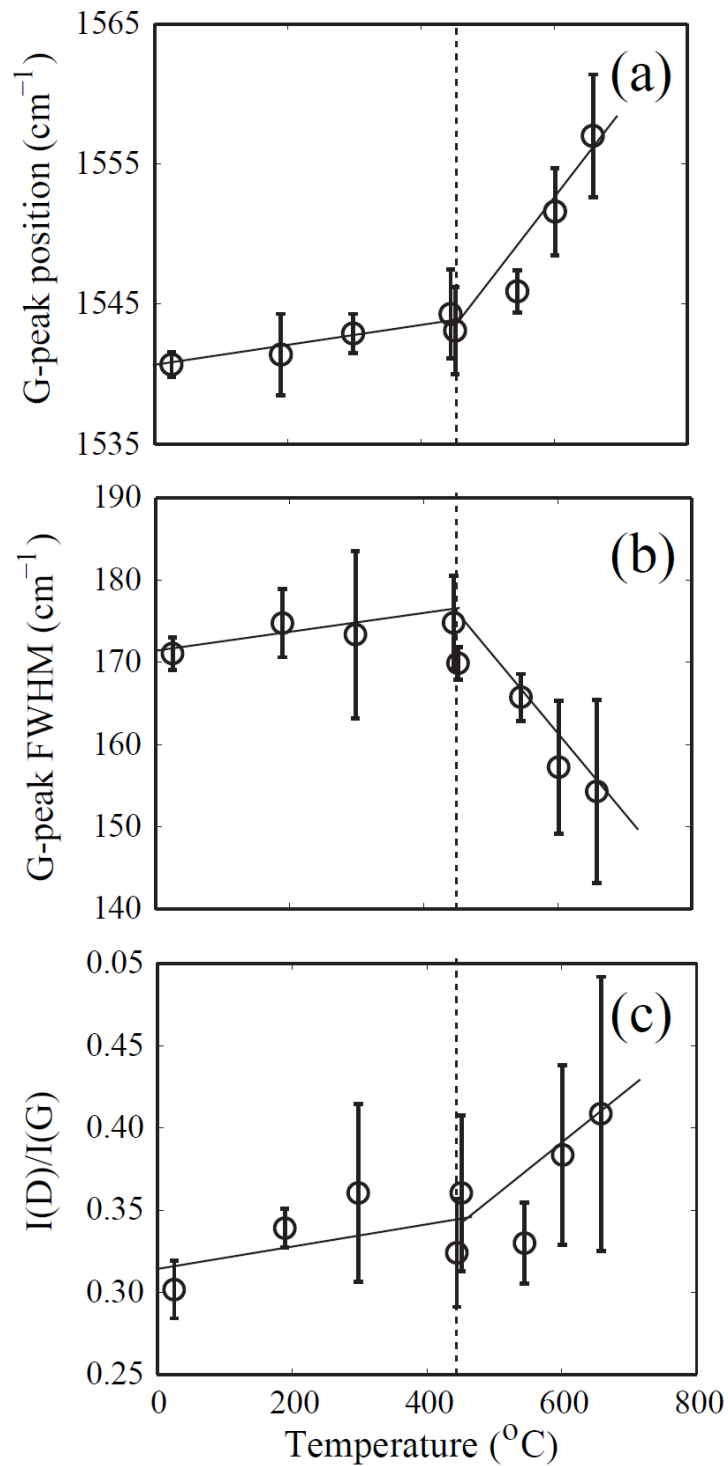
Figure 6. 4 Visible Raman results of the (a) G-peak position, (b) full width at half maximum (FWHM) of the G peak, and (c) D-to-G peak intensity ratio I(D)/I(G) versus maximum temperature of RTA treatment for 3.4-nm-thick *a*-C:H films.

As-deposited   Annealed at 660 °C

1.5 pA   375.0 fA

(a)   (d)

0.0 V

100 nm

-750.0 fA   -375.0 fA

402.0 pA   358.5 pA

(b)   (e)

0.2 V

-80.6 pA   -72.0 pA

6.6 nA   6.6 nA

(c)   (f)

1.0 V

-1.1 nA   -1.2 nA
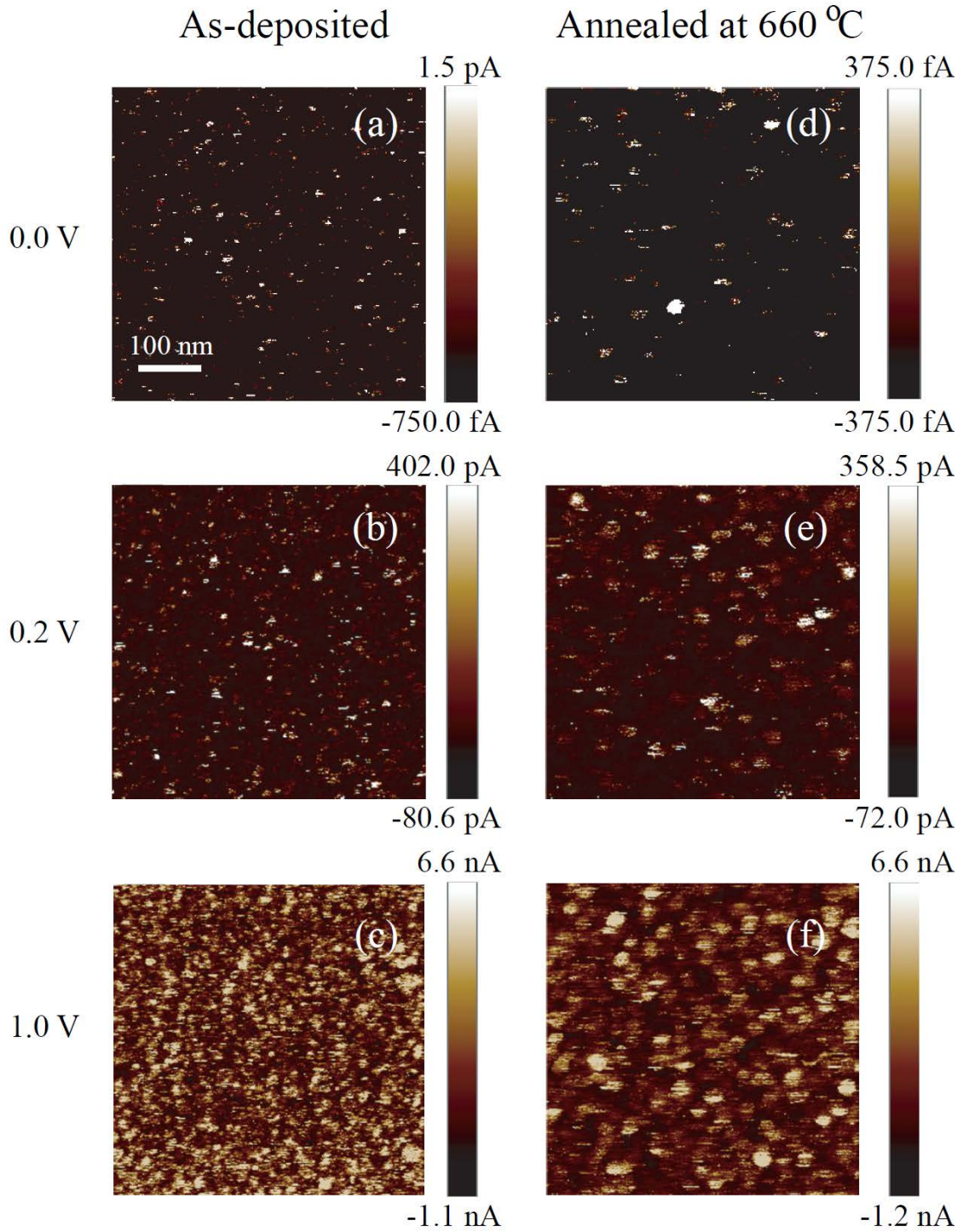
Figure 6. 5 Current images of 3.4-nm-thick *a*-C:H films obtained with an AFM before (left column) and after (right column) RTA tretament at a maximum temperature of 660 °C for a bias voltage applied to the AFM tip equal to (a,d) 0, (b,c) 0.2, and (e,f) 1.0 V.

Chapter 7

The effect of deposition energy on the growth and structure of ultrathin amorphous carbon films synthesized by energetic atoms deposition examined by molecular dynamics simulations

7.1 Introduction

Amorphous carbon (*a*-C) films with high sp^3 fractions demonstrate unique characteristics, such as high hardness, low friction, good wear resistance, and high chemical inertness [Robertson, 2002; Fung et al., 2000; Hauert, 2004; Erdemir and Donnet, 2006; Brown, 1998; Voevodin and Donley, 1996]. Many efforts have been made to enhance the quality of *a*-C films by varying the deposition method and process parameters [Zhang and Komvopoulos, 2008; Wang and Komvopoulos, 2012]. Although traditional deposition techniques, such as plasma-enhanced chemical vapor deposition and sputtering, have been used to deposit *a*-C films with unique physical properties, energetic deposition methods, in particular, filtered cathodic vacuum arc (FCVA) deposition, has captured significant research attention in recent years interest because the highly ionized plasma, intrinsic of FCVA, results in the formation of hard, dense, continuous, and smooth ultrathin carbon films [Brown, 1998; Anders et al., 2001; Anders, 2002].

The ion energy effect on the properties of *a*-C films deposited by the FCVA method has been the main objective of several studies [Robertson, 2002; Fallon et al., 1993; Pharr et al, 1996; Chhowalla, 1997; Byon and Anders, 2003]. The formation of *a*-C films with a high content of sp^3 hybridization can be explained by the subplantation model [Lifshitz et al, 1990], which postulates that energetic ions penetrating the surface of the bombarded material introduce local compressive stresses that promote sp^3 formation. Because of the subplantation effect, FCVA-deposited films exhibit multilayer structure [Wang and Komvopoulos, 2013; Davis et al., 1998; Davis et al. 1995]. However, limitations in the signal-to-noise ratio of characterization methods present an obstacle in understanding the formation of nanometer-thick films.

Molecular dynamics (MD) provides an alternative method for studying ultrathin film growth. MD provides an atomistic perspective of the material behavior and a statistical description of material response. Kaukonen and Nieminen [Karukonen and Nieminen, 1992] used the Tersoff potential [Tersoff, 1988; Tersoff, 1989] to simulate diamondlike (dlc) carbon film growth for carbon atom energy in the range of 1–70 eV and observed dense film formation for carbon atom energies between 40 and 70 eV. Marks et al. [Marks et al., 1996] used the Stillinger and Weber potential [Stillinger and Weber, 1985] to perform two-dimensional MD simulations and reported a transition from tensile to compressive residual stress with increasing deposition energy E_d, and a maximum compressive stress for a $E_d \approx 30$ eV, which is less than what has been observed in experimental studies [Fallon et al., 1993; Pharr et al, 1996; Chhowalla,

1997; Byon and Anders, 2003]. Jager and Albe [Jager and Albe, 2000] compared the Tersoff and reactive empirical bond order (REBO) potential [Brenner, 1990; Brenner, 1992; Brenner et al., 2002] by simulating ion-beam deposition of dlc films and proposed a modified REBO potential for simulating the film deposition process, which was used in MD simulations of Ma et al. [Ma et al., 2007] to study the microstructure and internal stress of ultrathin a-C films. Results from the latter study revealed that incident carbon atoms caused reconstruction of the substrate surface, leading to the formation of a three-layer structure comprising the substrate, an intermixing layer, and the deposited film, in agreement with the subplantation model.

Similar to other amorphous structures, a-C lacks long-range order. While the majority of previous studies have focused on a-C short-range order (e.g., sp^3 and sp^2 hybridization) [Kaukonen and Nieminen, 1992; Marks et al., 1996; Jager and Albe, 2000; Ma et al., 2007; Wang and Komvopoulos, 2011], insight into intermediate-range order (i.e., length scale of one to two times the average bond length) is limited. Intermediate-range order is considered to control the mechanical, optical, and electrical properties of amorphous materials [Martin et al., 2002; Kohara et al., 2011]. Although some experimental measurements, such as Raman shift, may provide information about intermediate-range order (e.g., clustering), MD simulations can provide much more detailed information, which is cumbersome or impossible to experimentally deduce [Rino et al., 2004; Guthrie et al., 2004]. The main objective of this study is to elucidate the dependence of short- and intermediate-range order in a-C films on incidence atom energy. Because previous studies [Fallon et al., 1993; Pharr et al, 1996; Chhowalla, 1997; Byon and Anders, 2003] have shown that the optimal incidence energy for a-C film deposition is ~80–100 eV, MD simulation results are presented for E_d in the range of 1–120 eV.

7.2 Modeling and numerical procedures

7.2.1 Molecular dynamics simulations

MD analysis relies on Newton's second law to simulate the motion of atoms. Essential to this method is the interaction force between atoms, represented by an interaction potential in MD studies [Allen and Tildesley, 1989]. The second-generation REBO potential [Brenner, 1990; Brenner, 1992; Brenner et al., 2002; Stuart et al., 2002] is adopted in this study because it is the most often used and acclaimed potential for hydrocarbon-related studies. The velocity-Verlet method [Levesque and Verlet, 1993] is used to integrate Newton's second law in the present MD analysis, which uses the large-scale atomic/molecular massively parallel simulator (LAMMPS) [Plimpton, 1995].

The origin of the second-generation REBO potential can be traced back to the Tersoff potential [Tersoff, 1988; Tersoff, 1999], which is applicable to systems of atoms interacting with each other through covalent bonds, such as carbon and silicon atoms. The potential energy associated with each bond consists of two parts representing attractive and repulsive energy terms. The influence of a third atom on a given bond is taken into account through a correction factor. The Tersoff potential energy of a system E is expressed as

$$E = \frac{1}{2} \sum_i \sum_{j \neq i} V_{ij} \tag{7.1}$$

where V_{ij} is the potential energy associated with the bond between two atoms i and j, given by

$$V_{ij} = f_C(r_{ij})[f_R(r_{ij}) - B_{ij}f_A(r_{ij})] \tag{7.2}$$

where f_R and f_A represent repulsive and attractive potentials, respectively, given by $f_R(r) = A\exp(-\lambda_1 r)$ and $f_A(r) = \bar{A}\exp(-\lambda_2 r)$ [Tersoff, 1988; Tersoff, 1999], and B_{ij} represents the effect of a third atom close to atom i. Because a covalent bond can only form when two atoms are close to each other and the bond also prevents the two atoms from approaching each other beyond a certain distance, the distance r between the two atoms (bond length) is in a narrow distance range. To account for this effect, a cut-off distance function $f_c(r)$ is included the interatomic potential V_{ij}, which is given by [Tersoff, 1988; Tersoff, 1999]:

$$f_C(r) = \begin{cases} 1 & r < R_1 \\ \dfrac{1}{2}\left[1 - \cos\left(\dfrac{\pi(r - R_1)}{R_2 - R_1}\right)\right] & R_1 < r < R_2 \\ 0 & r > R_2 \end{cases} \tag{7.3}$$

Coefficient B_{ij} is expressed as [Tersoff, 1988; Tersoff, 1999]

$$B_{ij} = \left[1 + \beta^n \varsigma_{ij}^n\right]^{-1/(2n)}$$

where

$$\varsigma_{ij} = \sum_{k \neq i,j} f_C(r_{ik})g(\theta_{ijk})\exp[\lambda_3^m(r_{ij} - r_{ik})^m] \tag{7.4}$$

$$g(\theta) = \gamma_{ijk}\left(1 + \frac{c^2}{d^2} - \frac{c^2}{[d^2 + (\cos\theta - \cos\theta_0)^2]}\right)$$

Parameters R_1, R_2, A, $\bar{A}$, β, λ_1, λ_2, λ_3, m, n, c, d, γ_{ijk}, and θ_0 included in equations are quoted from the literature [Tersoff, 1989].

Although the Tersoff potential can be used to describe single, double, and triple bonds, it cannot be used to describe π and conjugated bonds. To overcome this limitation, Brenner [Brenner, 1990; Brenner, 1992] modified the Tersoff potential to include the conjugation effect, introducing the so-called first-generation REBO potential. The main difference between the Tersoff potential and the first-generation REBO potential is that the latter accounts for the effect of nearby atoms on the bond of atoms i and j, which is represented by coefficient b_{ij}. In addition to the effect of atoms near atom i, the effect of atoms close to atom j is also included in the first-generation REBO potential. The conjugation function B_{ij} is given by [Brenner, 1990]

$$B_{ij} = \frac{1}{2}(b_{ij} + b_{ji}) + F_{ij}(N_i^t, N_j^t, N_{ij}^{conj}) \qquad (7.5)$$

where

$$b_{ij} = \left[1 + H_{ij}(N_i^h, N_i^c) + \sum_{k \neq i,j} f_C(r_{ik}) g(\theta_{ijk}) \exp[\alpha_{ijk}[(r_{ij} - R_{ij}^e) - (r_{ik} - R_{ij}^e)]] \right]^{-\delta_i} \qquad (7.6)$$

Where N_i^h, N_i^c, and N_i^t are the number of hydrogen atoms, the number of carbon atoms, and the total number of atoms bonded to the atom i. H_{ij} and F_{ij} are obtained from bicubic and tricubic splines of known values for integer numbers of N_i^h, N_i^c, N_i^t, whereas N_i^{conj}, α_{ij}, R_{ij}^e, and δ_i are fitting parameters obtained from previous studies [Brenner, 1990; Brenner, 1992].

The first-generation REBO potential has been widely used to model hydrocarbon systems [Jager and Albe, 2000; Ma et al., 2007]. However, because the repulsive and attractive potentials are too restrictive for modeling energetic atomic collisions, Brenner [Brenner et al., 2002] modified this potential to overcome this problem, introducing a new potential known as the second-generation REBO potential. This potential also increased the accuracy of H_{ij} and F_{ij} through the use of more accurate values for the integer numbers N_i^h, N_i^c, N_i^t and N_i^{conj}. The estimate of the correction factor B_{ij} was also improved by using more accurate values to fit H_{ij} and F_{ij}. The second-generation REBO potential is used in this study to describe the interaction between carbon atoms.

Jager et al. [Jager and Albe, 2000] used the first-generation REBO potential to perform MD simulations of the deposition of a carbon film, but although they obtained a film density close to that of diamond, the sp^2 content was ~90%, which is close to that of graphite. Thus, to simulate the formation of a carbon film with a high sp^3 content, they increased the cut-off distance R_1, and R_2 in Eq. (7.4) from 1.7 and 2.0 Å to 1.95 and 2.25 Å, respectively. While this resulted in the simulation of a carbon film with an extremely high sp^3 content (>85%), these changes in the cut-off distance also led to the formation of non-physical structures.[38] In the present study, the second-generation REBO potential and the LAMMPS code[37] were used to study the film deposition process. A total of 1400 carbon atom depositions were simulated sequentially to simulate the formation of a carbon film.

The film stress is calculated from a per-atom tensor S_{ab}, which includes kinetic, pairwise, and bond energy contributions (therefore, has units of stress × volume), defined as

$$S_{ab} = -[m v_a v_b + \frac{1}{2}\sum_{n=1}^{N_p} (r_{1a}F_{1b} + r_{2a}F_{2b}) + \frac{1}{2}\sum_{n=1}^{N_b} (r_{1a}F_{1b} + r_{2a}F_{2b})] \qquad (7.7)$$

where the first term represents the contribution of kinetic energy, the second term is a pairwise energy contribution with a total number of loops over its neighbors of N_p, the third term is a bond energy contribution of a total number of bonds equal to N_b, and indexes a and b represent coordinates x, y, and z.

The hydrostatic (mean) stress σ_h and in-plane stress σ_i can then be expressed as

$$\sigma_h = \frac{(S_{xx} + S_{yy} + S_{zz})}{3V} \tag{7.8}$$

$$\sigma_i = \frac{(S_{xx} + S_{yy})}{2V} \tag{7.9}$$

with positive and negative values denoting tensile and compressive stresses, respectively, and V representing the volume of a given domain (a slice in the present analysis).

7.2.2 Deposition process model

Carbon film formation was simulated by a single-atom deposition process. Carbon atoms were generated randomly at an x-y plane above the substrate surface at a distance of 55 Å from the fixed bottom surface of the diamond substrate. To simulate the normal incidence at the diamond surface, each carbon atom was assigned a velocity in the negative z-direction and magnitude commensurate to certain energy, typical of FCVA film deposition process. In all MD simulations, the time step was set at 0.5 fs. Figure 7.1 shows the MD model used to simulate film formation by a single-atom deposition method. The bottom three planes of atoms of the diamond (100) substrate were fixed to mimic a semi-infinite half-space. Atoms in the next four planes on top of the fixed atoms were assigned to an external heat bath via a Berendsen thermostat [Berendsen et al., 1984]. To minimize the effect of the thermostat on the deposition process, the remaining carbon atoms were divided into two groups. For each carbon atom generated in the simulation, all substrate atoms within a cylinder surrounding the arriving carbon atom were allowed to move freely, whereas all other remaining substrate atoms were connected to the thermostat. With this technique, atoms connected to the heat bath were updated during the deposition of each atom, and the effect of the thermostat on the interaction between deposited carbon atoms and substrate atoms was significantly reduced.

Between the deposition of two carbon atoms, the system was allowed to relax for 2 ps and then to be equilibrated by the heat bath. The relaxation time was chosen according to a study [Marks, 1997] showing a thermal spike lifetime less than 0.5 ps for ion energy less than 100 eV. Atoms sputtered off from the substrate were removed from the system before injecting a new carbon atom.

7.2.3 Substrate model

Figure 7.1 shows the diamond substrate used in the present study with coordinates x[011], y[0$\bar{1}$1], and z[100]. Periodic boundary conditions were applied to the x- and y-directions. The diamond surface in the z-direction was not constrained to allow for film growth. In each simulation, the model was first relaxed to minimize its energy such that the difference in total energy between two consecutive time steps is less than 10^{-10} eV. The dimensions of the relaxed structure are $20.17 \times 20.17 \times 60$ Å. The original substrate surface is used as the reference plane ($z = 0$), while film growth occurs in the positive z-direction. Without relaxation, an internal stress was produced in the diamond substrate due to the surface tension effect of the free surface [Figure 7.2(a)]. To reduce the internal stress, the diamond substrate was subjected to thermal

relaxation by increasing the temperature from 300 to 800 K, keeping it at 800 K for 5 ps, decreasing it to 330 K, and finally allowing the system to relax for 5 ps. This thermal relaxation process reduced the internal stress [Figure 7.2(b)], while the resulting atomic rearrangement at the diamond surface yielded 95% sp^2 instead of 100% sp^1 of the initial diamond surface.

7.2.4 Ring size statistical analysis

Ring statistics was performed with the interactive structure analysis of amorphous and crystalline systems (ISAACS) program [Roux and Jund, 2010]. Rings of sizes up to 40 were analyzed with the ISAACS program.

7.3 Results and discussion

7.3.1 Film structure

Figure 7.3 shows a-C film configurations for different deposition energies. Low-energy (i.e., 1 eV) deposition produced a porous film structure dominated by sp^2 hybridization without damaging the diamond substrate [Figure 7.3(a)]. The formation of this film structure is attributed to the dominance of surface adsorption. The increase of E_d resulted in significantly denser film structures dominated by sp^3 hybridization and the formation of an intermixing layer of progressively increased thickness [Figures 7.3(b)–3(c)].

Figures 7.4(a)–7.4(d) show the initial stage of a-C film growth for $E_d = 1$ eV. Impinging carbon atoms first attach to surface atoms (adsorption) and as soon as these surface sites are saturated [Figure 7.4(a)] they begin to form chain-like structures of an average bond length equal to 1.3322 ± 0.0115 Å [Figure 7.4 (b)], which is close to the double-bond length of ethylene (1.339 Å). Because this double bond is reactive, it tends to capture other carbon atoms to form a more stable single bond. Thus, deposition of more carbon atoms does not increase the chain length but causes the formation of ring-like structures [Figure 7.4 (c) and Figure 7.4 (d)]. The average bond length between sp^1 and sp^2 sites increases from 1.3322 ± 0.0115 Å to 1.3778 ± 0.0129 Å. Because of their low energy, impinging carbon atoms cannot break existing carbon bonds to penetrate into the substrate and the resulting a-C film structure is dominated by sp^2 and sp^1 hybridizations. Increasing E_d above 20 eV resulted in the formation of significantly denser films without any voids. Figures 7.4(e)–7.4(h) show the initial stage of a-C film growth for relatively high $E_d = 80$ eV. Unlike the porous film structure produced with low-energy atoms, high-deposition energy significantly not only enhanced the film density but also greatly increased the sp^3 content of the film. However, sp^2 and sp^1 hybridizations remained as the dominant types of carbon bonding at the surface. This finding suggests that the formation of sp^3 structures is mainly a consequence of the implantation mechanism that dominates the subplantation process. A comparison of simulation results for E_d in the range of 1–120 eV showed that the film surface roughness increased with E_d. This roughening effect observed at high deposition energies can be attributed to sputtering of the film by the highly energetic carbon atoms.

7.3.2 Film density and atom coordination

Two important film properties are examined in this section – film density and atom coordination. Atom coordination is calculated as the number of neighboring atoms within a

87

distance of 1.85 Å from the reference atom. The coordination number is an important parameter characterizing the composition of the a-C film. Atoms with a coordination number of 4 are usually referred to as tetrahedrally (sp^3) hybridized (diamond-like), whereas atoms with a coordination number of 3 are referred to as trigonally (sp^2) hybridized (graphite-like). Because the deposited films are not uniform in the z-direction, the properties as a function of z are calculated as averages of 0.85-Å-thick slices, which is the distance between two layers of atoms in the diamond [100] direction.

Figure 7.5 shows the relative density (i.e., the film density normalized by the density of the diamond substrate) and the carbon coordination fraction versus deposition energy E_d. The sp^3 content sharply increases with the increase of E_d in the range of 1–20 eV and less significantly in the range of 20–80 eV, respectively. In the 20–80 eV energy range, the energetic carbon atoms can penetrate the film surface and become adsorbed in the bulk of the forming carbon film. This mechanism is known as subplantation and usually results in sp^3 hybridization. In the 80–120 eV energy range, the sp^3 content decreases with the increase of E_d because carbon atom rebounding onto the carbon film decreases sp^3 hybridization in the bulk of the carbon film. Thus, the optimum energy for obtaining the highest sp^3 content in the a-C film is ~80 eV, which is in agreement with experimental observations [Fallon et al., 1993; Pharr et al., 1996; Chhowalla et al., 1997; Byon and Anders, 2003]. The variation of the sp^3 fraction with E_d is similar to that of the film density, suggesting that denser a-C films are also characterized by a higher sp^3 fraction.

Considering that the bond length in sp^3 hybridization is longer than that in sp^2 hybridization, a-C films with higher sp^3 hybridization should also exhibit longer average bond length. Figure 7.6 shows the effect of the deposition energy E_d on the radial distribution function Ψ_r. The first peak (corresponding to the average bond length) slightly shifts to the right with the increase of E_d from 1 eV [Figure 7.6(a)] to 80 eV [Figure 7.6(b)], revealing an increase in the average bond length, which is consistent with the increase of sp^3 hybridization. However, the first peak shifts to the left with the further increase of E_d from 80 eV [Figure 7.6(c)] to 120 eV [Figure 7.6(d)], implying a decrease in average bond length and, in turn, sp^3 hybridization.

Changes in sp^3 hybridization due to the variation of E_d are also due to the variation of the bond angle distribution in the a-C film. For purely sp^3 hybridization (e.g., diamond), the bond angle is ~109 $^{\circ}$, whereas for sp^2 hybridization (e.g., graphite) it is equal to 120°. Thus, higher sp^3 hybridization implies smaller bond angle. Figure 7.7 shows the dependence of the bond angle distribution Φ_b on the deposition energy E_d. The left shift of Φ_b with the increase of E_d from 1 eV [Figure 7.7(a)] to 80 eV [Figure 7.7(c)] indicates a decrease of sp^2 hybridization and the simultaneous increase of sp^3 hybridization. However, the further increase of E_d to 120 eV [Figure 7.7(d)] leads to a right shift of Φ_b, implying an increase in sp^2 hybridization and a decrease in sp^3 hybridization. Different from other Φ_b other distributions, Φ_b for $E_d = 1$ eV contains a small peak at ~60° and a significant fraction of bond angles in the range of 140°–180°, presumably due to the high fraction of sp^1 hybridization in the film synthesized under deposition conditions of $E_d = 1$ eV. With the increase of E_d above 20 eV, the fraction of sp^1 hybridization decreases to almost zero. The high sp^1 hybridization in the film deposited under $E_d = 1$ eV also affects the Ψ_r distribution (Figure 7.6), i.e., all Ψ_r distributions contain a small peak at 2 nm except the distribution for $E_d = 1$ eV.

Figure 7.8 shows the effect of E_d on the depth distribution of the relative density and carbon atom hybridization of a-C films. The film density is normalized to that of diamond. Both low- and high-energy deposition cases reveal the existence of a three-layer structure consisting of film/substrate interface layer, bulk film, and surface layer. The interface layer is an intermixing layer of deposited carbon atoms and atoms of the diamond substrate. The thickness of the intermixing layer is defined as the distance from the original surface of the diamond substrate to the location where the relative density is equal to 0.9. The intermixing layer may be interpreted as the surface layer of the diamond substrate that is damaged by the bombarding carbon atoms [Wang and Komvopoulos, 2013]. The bulk of the film is the region of nearly constant density and atom hybridization, whereas the film surface is defined as the region where the density and/or sp^3 fraction sharply decrease. Low-energy deposition produces relatively thicker a-C films with negligible intermixing with the substrate and dominated by sp^1 and sp^2 hybridization, whereas high-energy deposition produces thinner a-C films integrated with the substrate via an intermixing layer and with much higher sp^3 content.

Table 7.1 shows the effect of E_d on the thickness and density of the intermixing layer, bulk film, and surface layer. All cases show the formation of a three-layer film structure. For low-energy (1 eV) deposition, the impinging carbon atoms do not damage the diamond substrate and the thickness of the intermixing layer is negligibly small. The increase of E_d enhances the penetration of the diamond surface by carbon atoms, resulting in the formation of a thicker intermixing layer. For $E_d = 80$ eV, the intermixing layer thickness is estimated to be 5.35 Å, which is larger than one lattice distance in the z-direction. The increase of the intermixing layer thickness with E_d suggests that more energetic atoms cause more damage to the substrate. Conversely to the intermixing layer, the bulk film thickness decreases with the increase of E_d because highly energetic atom bombardment leads to significant carbon atom implantation. The enhancement of the bombarding intensity of carbon atoms induced by the increase of E_d also has a profound effect on the bulk film density; however, the effect on the surface layer is marginal, evidently due to the significantly less bombarding carbon atoms. For relatively low E_d (< 20 eV), the mobility of incident carbon atoms is limited, resulting in a thick surface layer, whereas for intermediate E_d (i.e., 20–80 eV), carbon atoms are more energetic and, therefore, can diffuse to minimum-energy sites, producing a thinner and smoother surface layer. However, at relatively high deposition energies (i.e., 120 eV), carbon atom deposition significantly exceeds atom diffusion, leading to the formation of a thicker and rougher surface layer. Among the simulation cases listed in Table 7.1, the film with the highest bulk density (3.3 g/cm^3) corresponds to $E_d = 80$ eV. This is in agreement with experimental results showing that high-density a-C films can be obtained for E_d in the range of 80–100 eV [Robertson, 2002].

7.3.3 Film stress

Figure 7.9 shows the variation of the hydrostatic stress σ_h [Eq. (7.8)] and the in-plane stresses σ_i [Eq. (7.9)] with the deposition energy E_d. The hydrostatic stress is the average of all the stresses parallel and perpendicular to the film surface. Because stresses parallel to the film surface are much higher than the out-of-plane stress, σ_h is always less than σ_i. While low-energy (1 eV) deposition produces a mild tensile stress, increasing E_d leads to the development of high compressive stresses in the film. This trend is in agreement with the increase of the sp^3 fraction (Figure 7.5) and bulk film density (Table 7.1) with E_d.

Figure 7.10 shows through-thickness distributions of hydrostatic and in-plane stress for $E_d =$ 1 and 80 eV. Low-energy deposition produces relatively low and mainly tensile film stress [Figure 7.10(a)], attributed to the stretching effect of excess sp^1 dangling bonds at the surface, which are less constrained because they have fewer neighboring atoms. Because a tensile stress is not conducive to sp^3 hybridization, the sp^3 fraction in the film synthesized under low-energy (1 eV) deposition conditions is less than 5% [Figures 7.5 and 7.8(a)]. However, relatively high-energy (80 eV) deposition produces a compressive film stress between –17 and –22 GPa, which is in fair agreement with experimentally measured compressive stresses varying between –11 and –15 GPa [Fallon et al., 1993; Polo et al., 2000; Ferrari et al., 2002]. The discrepancy between MD results and experimental measurements may be due to the periodic boundary condition applied to the x- and y-directions and errors introduced in the experimental measurements of the film stress (e.g., errors in the measurement of the very sample curvature induced by the stress in very thin films). In both simulation cases, both σ_h and σ_i the decrease close to zero at the surface, providing validation to the method used to calculate the film stresses (section IIB).

7.3.4 Intermediate range order: ring size statistics

Intermediate-range order refers to the order of the atomic structure at length scales larger than one or two times the average bond length and correlates to the mechanical, optical, and electric properties of amorphous materials [Martin et al., 2002; Kohara et al., 2011]. The most widely used approach for studying intermediate-range order, especially in numerical simulations, is the ring size statistics originated from graph theory [King, 1967; Franzblan, 1991; Guttman, 1990]. A ring is defined as a closed loop consisting of atoms connected to each other by bonds. The ring size is defined as the number of atoms in the ring. To calculate the number of rings and the connectivity of the rings, it is necessary to identify first those rings that are relevant to intermediate-range order. Primitive rings (i.e., rings that cannot be divided into smaller rings), which are closely related to intermediate-range order, are considered in the present study [Yuan and Cormack, 2002; Roux and Jund, 2010]. Carbon atoms within a distance range in the z-direction of 15–30 Å are considered in the present ring statistics. Since the initial thickness of the diamond substrate is equal to ~14 Å, atoms within a depth distance of 15–30 Å provide a good representation of the atomic structure of the a-C film.

Figure 7.11 shows the ring size distribution Φ_r (defined as the ratio of the number of rings to the total number of atoms in the system) as a function of ring size d (expressed in number of atoms) for $E_d =$ 1–120 eV. The cut-off ring size is equal to 3 because the smallest ring contains three atoms. Low-energy deposition produces a wide Φ_r distribution in the range $3 < d < 40$ [Figure 7.11(a)]; however, the increase of E_d to 20 eV yields a tighter Φ_r distribution in the range $3 < d < 16$ and the average d is equal to ~8 [Figure 7.11(b)], indicating a carbon atom network of increased order. Even tighter Φ_r distribution is shown for $E_d =$ 80 eV and average d decreases to 6 [Figure 7.11(c)]. Thus, a further order increase of the atomic network is encountered in the intermediate range of E_d. Because both diamond (pure sp^3 hybridization) and graphite (pure sp^2 hybridization) have $d =$ 6, the shift of Φ_r to the left may be interpreted as an increase of both sp^2 and sp^3 hybridizations. The increase of E_d from 80 to 120 eV leads to a decrease in intermediate-range order, as evidenced by the wider Φ_r distribution and the increase of average d to 7 [Figure 7.11(d)].

Figure 7.12 shows the atom distribution Φ_a (defined as the number of atoms contributing to the formation of rings of a given size divided by the total number of atoms in the system) as a function of ring size d for E_d = 1–120 eV. Atoms shared by two or more rings of the same size are only counted once. The wide Φ_a distribution obtained for E_d = 1 eV [Figure 7.12(a)] is consistent with that shown in Figure 7.11(a). For E_d = 20 and 80 eV [Figure 7.12(b) and 7.12(c), respectively], Φ_a is centered in the range $6 < d < 9$, whereas for E_d = 120 eV [Figure 7.12(d)], Φ_a is wider than the distributions obtained for E_d = 20 and 80 eV. The effect of E_d on the number of atoms shared by rings of a given size may be interpreted in the context of the results shown in Figures 7.11 and 7.12. If rings of a given size do not share any atoms, the atoms involved in the formation of the rings of the given size should be equal to the ring size times the number of rings, and, accordingly, larger Φ_r should have larger Φ_a. A larger Φ_r with a smaller Φ_a thus implies strong atom sharing for the rings of a given size. Comparison of Figures 7.11 and 7.12 reveals that Φ_a for d = 6 is similar for E_d = 20 eV and E_d = 80 eV whereas the corresponding Φ_r is larger for E_d = 80, implying that more rings with d = 6 share atoms in the a-C films deposited under E_d = 80 eV than E_d = 20 eV. A similar observation can be made for d = 7. If we only focus on E_d = 80 eV, Figure 7.11 (b) shows that Φ_r is larger for d = 9 than for d = 6 or 7, however, Figure 7.12 (b) shows that Φ_a is similar for d = 6, 7, and 9, indicating that rings with d = 9 share more atoms with each other than rings with d = 6 or 7.

Further insight into intermediate-range ordering can be obtained by considering the normalized atom distribution Φ_a^*, defined as Φ_a for a given d to the maximum value of Φ_a, denoted by $\Phi_{a,max}$, calculated from the ring size distribution Φ_r (Figure 7.11). Assuming that there are no rings of a given size d' sharing n atoms, $\Phi_{a,max} = n\Phi_r(d')$. Figure 7.13 shows the normalized atom distribution Φ_a^* as a function of ring size d. Φ_a^* = 1 implies no atom sharing among rings of the same size, whereas low Φ_a^* values indicate the existence of a significant number of atoms that are shared among rings of the same size. For E_d = 1 eV, atom sharing is insignificant for almost all rings of a given size [Figure 7.13(a)], while for E_d = 20 eV, atom sharing is mainly observed for rings with sizes in the range $5 < d < 14$ [Figure 7.13(b)]. More atom sharing among rings of a given size is observed with the increase of E_d to 80 eV [Figure 7.13(c)]; however, the overall Φ_a^* distribution is similar to that for E_d = 20 eV. Atom sharing among rings with sizes in the range $5 < d < 10$, where the majority of rings exist for E_d = 20, 80, and 120 eV (Figure 7.11), is similar for E_d = 20 and 80 and less for E_d = 120 eV [Figure 7.13(d)].

Further insight into intermediate-range atom ordering can be obtained by considering the normalized maximum and minimum atom distributions $\Phi_{a,max}^*$ and $\Phi_{a,min}^*$, representing the fraction of atoms in rings of a given size that are also involved in rings having the given ring size as maximum or minimum among all atoms involved in the formation of rings of the given size. For example, assume n atoms participate in the formation of all the rings of a given size d^*. Some of these atoms may also be involved in the formation of rings of other sizes. Among these atoms, assume k atoms are present in rings with maximum size d^*, then $\Phi_{a,max}^* = k/n$. Similarly, if among these n atoms there are m atoms present in rings with minimum size d^*, then $\Phi_{a,min}^* = m/n$. Figure 7.14 shows the effect of the deposition energy E_d on $\Phi_{a,max}^*$ and $\Phi_{a,min}^*$. High $\Phi_{a,max}^*$ implies less atoms of rings of a given size shared with larger rings, whereas high $\Phi_{a,min}^*$ implies less atoms of rings of a given size shared with smaller rings. For E_d = 1 eV, $\Phi_{a,max}^*$ assumes low values in the range $3 < d < 8$ [Figure 7.14(a)], indicating a high connectivity with $d > 8$, whereas

$\Phi^*_{a,min}$ assumes high values in the same range [Figure 7.14(*e*)], indicating a low connectivity among rings with $3 \leq d \leq 8$. In addition, the decreasing trend of $\Phi^*_{a,min}$ for $d > 10$ implies a sharply increasing connectivity among rings with $d > 10$ and $3 \leq d \leq 10$. For $E_d = 20$ and 80 eV, $\Phi^*_{a,max}$ obtains higher values in the relatively large-ring range $13 \leq d \leq 16$ [Figures 7.14(*b*) and 7.14(*c*)], whereas $\Phi^*_{a,min}$ assumes relatively smaller values in the small-ring range $3 \leq d \leq 10$ [Figures 7.14(*f*) and 7.14(*g*)], implying weak and strong connectivity for relatively large and small rings, respectively. Also, the very low $\Phi^*_{a,max}$ values and very high $\Phi^*_{a,min}$ values in the range $3 \leq d \leq 6$ indicate a strong connectivity between small and large rings in the *a*-C films deposited for $E_d = 20$ and 80 eV. Although $\Phi^*_{a,max}$ and $\Phi^*_{a,min}$ for $E_d = 20$ and 80 eV are similar, a comparison of Figures 7.14(*b*), 7.14(*c*), 7.14(*f*), and 7.14(*g*) indicates slightly stronger connectivity of small rings for $E_d = 80$ eV than 20 eV. Compared to the rings corresponding to $E_d = 1$ eV, both 20 and 80 eV have tighter ring size distributions and stronger connectivity among small rings and among small and large rings are obtained for $E_d = 20$ and 80 eV compared to 1 eV. Considering that the majority of the rings for $E_d = 20$ and 80 eV [Figures 7.12(*b*) and 7.12(*c*)] are smaller than those for $E_d = 1$ eV [Figure 7.12(*a*)], it may be inferred that connectivity was significantly enhanced by the increase of the deposition energy. Although the connectivity of small rings ($3 \leq d \leq 6$) for $E_d = 120$ eV [Figures 7.14(*d*) and 7.14(*h*)] is only slightly worse than those for $E_d = 80$ eV [Figures 7.14(*c*) and 7.14(*g*)], the *a*-C film contains large rings ($d > 16$) connected to small and large rings; however, connectivity for $E_d = 120$ eV is better than that for $E_d = 1$ eV, as indicated by the small range of $\Phi^*_{a,min}$ [Figure 7.14(*h*)].

7.4 Conclusion

The structure, properties, and internal stress of ultrathin *a*-C films synthesized by energetic atoms deposition were examined in the context of MD simulation results. Atom-atom interaction was described by the second-generation REBO potential. All simulations revealed the formation of three-layer structure consisting of intermixing layer, bulk film, and surface layer. The film structure (atom hybridization), density, and residual stress showed a strong dependence on the energy of impinging carbon atoms (deposition energy E_d). Film density, residual stress, and sp^3 content increased with E_d, in agreement with experimental results. Relatively high E_d (e.g., 120 eV) caused damage to the substrate surface and led to the formation of a thicker surface layer dominated by sp^2 and sp^1 hybridizations and free dangling bonds. For the range of E_d examined (1–120 eV), optimum film properties, i.e., maximum density, thinnest intermixing and surface layers, and highest sp^3 fraction, were obtained for $E_d = 80$ eV, also in agreement with experimental findings.

Atom collision during deposition led to the development of an internal stress in the film. Low-energy ($E_d = 1$ eV) deposition produced a tensile film stress, in agreement with the dominant presence of sp^1 and sp^2 hybridizations at the film surface, which are reactive and tend to induce stretching of the film. High-energy ($E_d > 20$ eV) deposition resulted in a compressive state in the films, with a hydrostatic stress between –11 and –13 GPa. Because a local compressive environment is conducive to sp^3 hybridization and the compressive stress in the film increased with E_d, *a*-C films with high sp^3 content were produced with highly energetic carbon atoms.

The structure and properties of a-C films synthesized by energetic atoms deposition methods, such as FCVA, strongly depend on the intensity that impinging carbon atoms interact with substrate atoms. Low-energy carbon atoms are mainly adsorbed at the surface of the growing film, resulting in sp^2 and sp^1 hybridization. However, high-energy carbon atoms penetrate the film surface, inducing subsurface interactions that favor sp^3 hybridization. High-energy carbon atoms may also rebound from the surface or sputter off atoms adsorbed onto the surface of the growing film.

Ring-size statistics provided insight into the effect of energetic atom impingement on intermediate-range atomic ordering. Low-energy ($E_d = 1$ eV) deposition produced a-C films with the widest ring size distribution and lowest ring connectivity. Increasing E_d to 20 and 80 eV resulted in tighter ring size distributions and increased ring connectivity. However, a further increase of E_d to 120 eV resulted in broader ring size distribution and decreased connectivity of small rings.

The MD results of this study are in good qualitative agreement with experimental results of the optimum deposition energy and internal stress of a-C films deposited by energetic atoms deposition methods. The findings of this investigation are also complementary to experimental studies because they provide insight into the formation of a three-layer film structure, the evolution of damage at the substrate surface, and the intermediate-range order for different deposition energies, which is cumbersome to identify by experimental methods.

Table 7. 1 Effect of deposition energy on the thickness and density of intermixing layer, bulk film, and surface layer.

Deposition energy (eV)	Thickness (Å)			Density (g/cm^3)	
	Intermixing layer	Bulk film	Surface layer	Bulk film	Surface layer
1	0.1	35	6.6	1.68	0.97
20	2.68	20.52	2.7	3.13	0.98
80	5.35	15.17	9.33	3.30	1.79
120	6.14	14.28	11.41	3.19	1.58
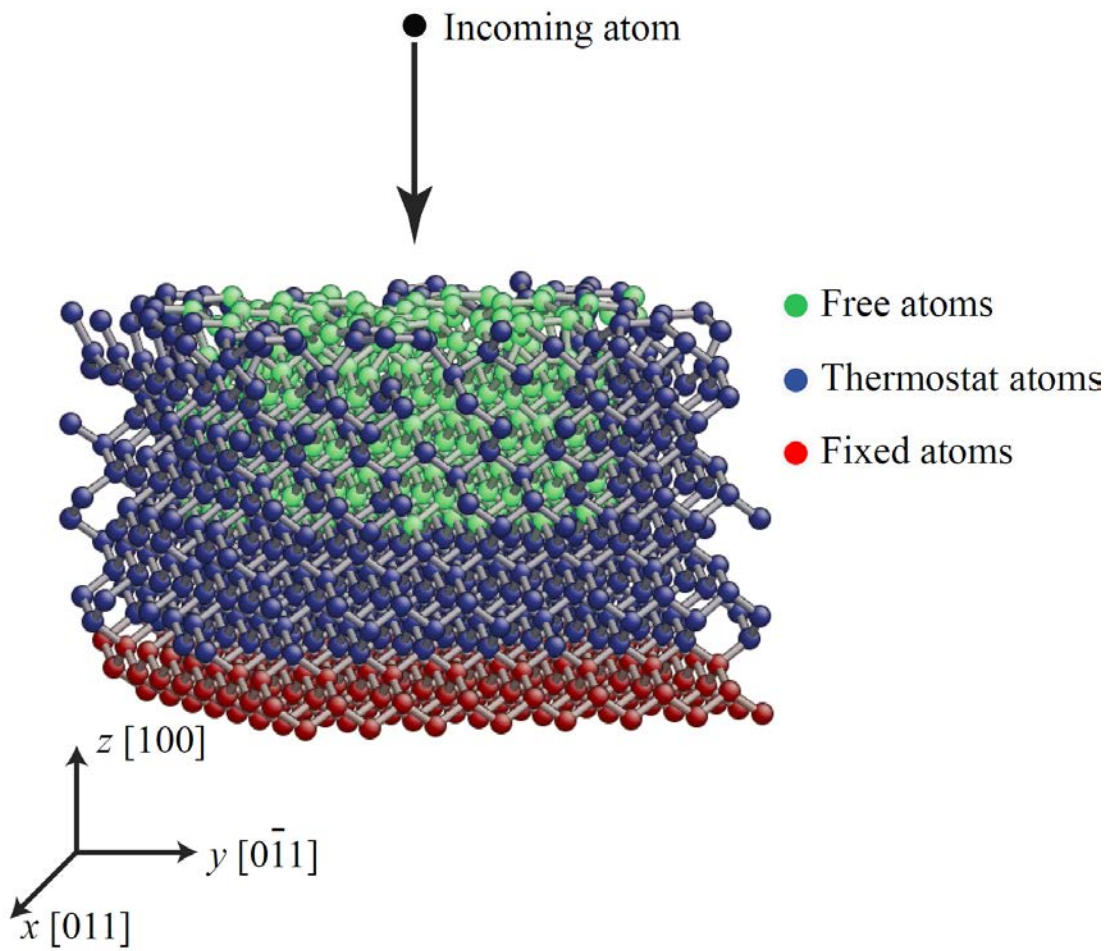
Figure 7. 1 Molecular dynamics model of film deposition by energetic atoms.
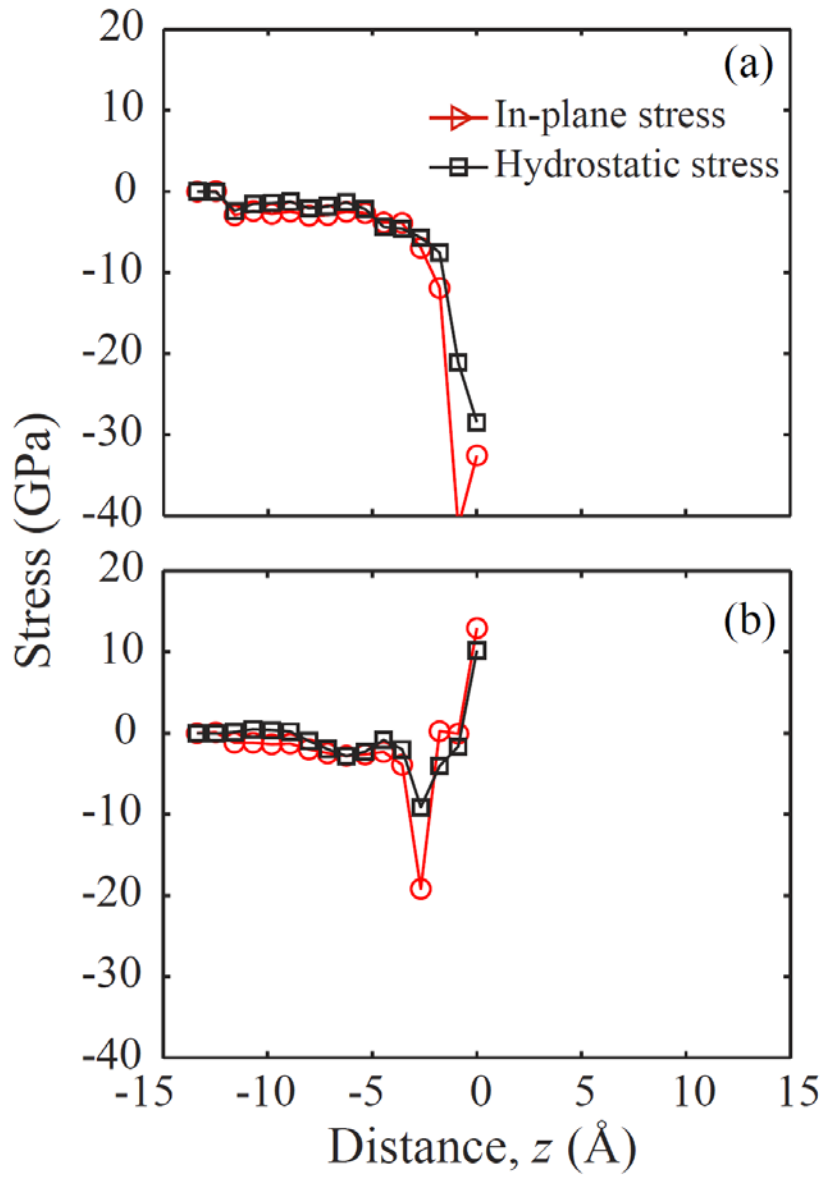
Figure 7. 2 Depth profiles of hydrostatic stress σ_h and in-plane stress σ_i in the diamond substrate (*a*) before and (*b*) after thermal relaxation.
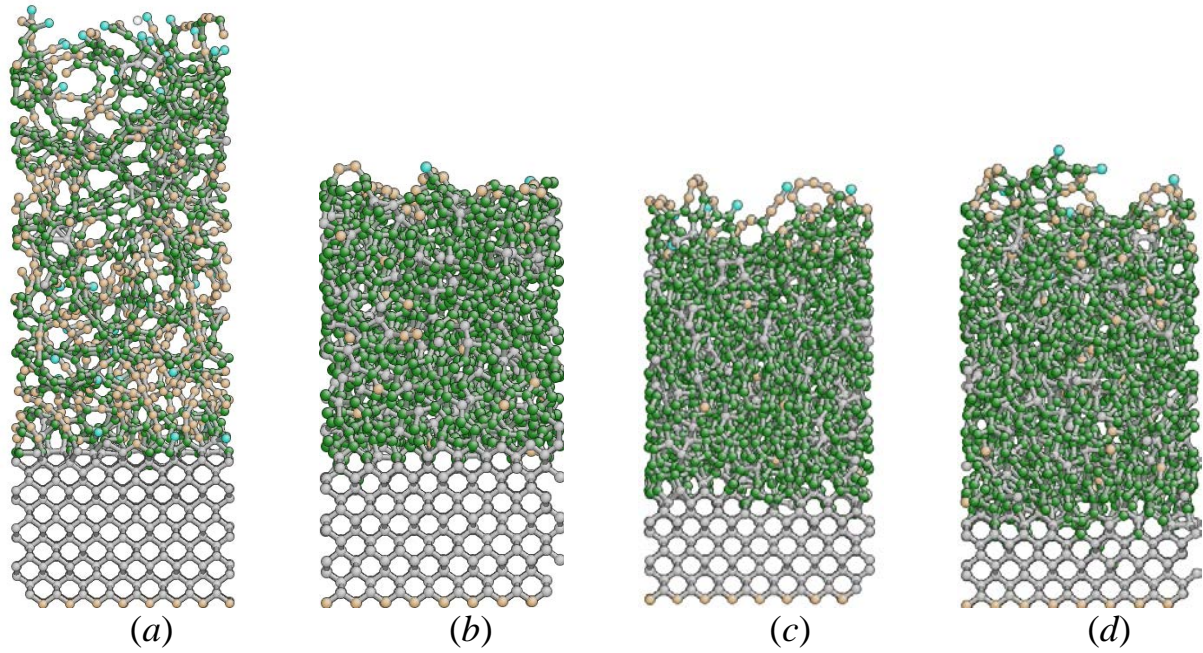
Figure 7. 3 Film structure for deposition energy E_d equal to (*a*) 1, (*b*) 20, (*c*) 80, and (*d*) 120 eV. Atoms with a different coordination number are shown in different color (gray: sp^3, green: sp^2, yellow: sp^1, and blue: sp).

	1 atom	50 atoms	157 atoms	324 atoms
1 eV	(*a*)	(*b*)	(*c*)	(*d*)
80 eV	(*e*)	(*f*)	(*g*)	(*h*)
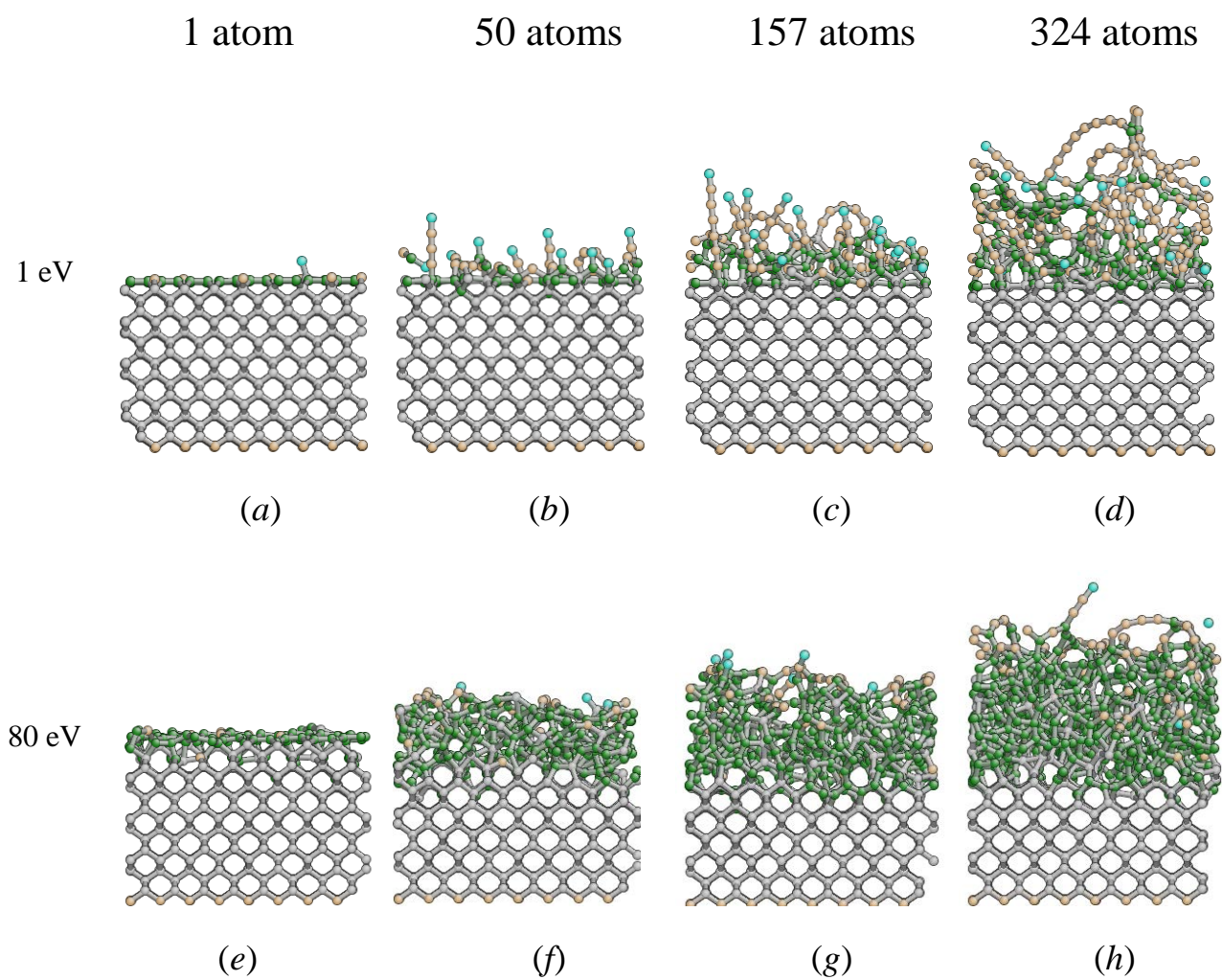
Figure 7. 4 Initial stage of film growth for deposition energy E_d equal to 1 eV (first row) and 80 eV (second row).
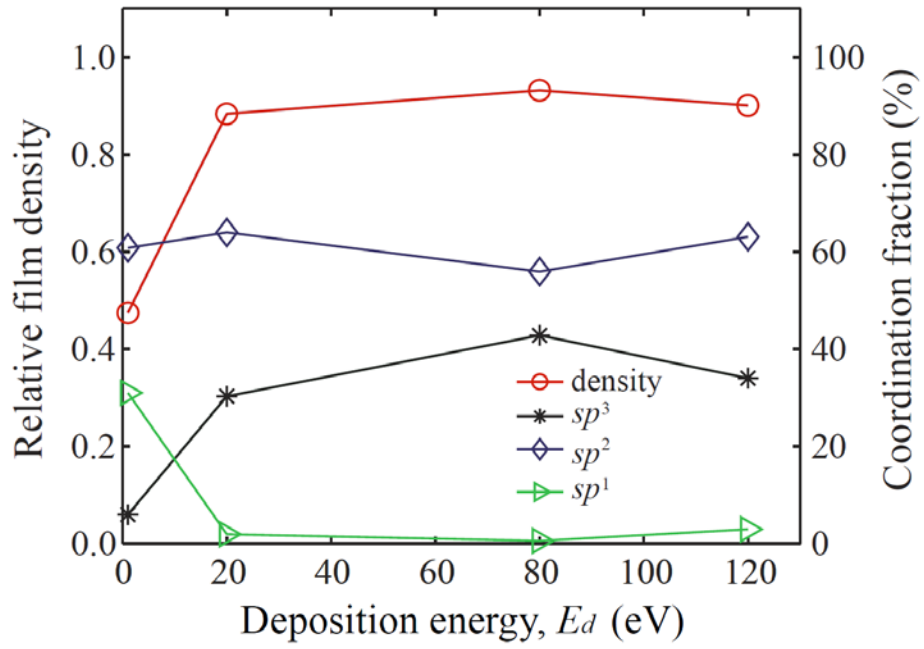
Figure 7. 5 Relative film density and carbon atom hybridization versus deposition energy E_d. The film density was normalized by the density of the diamond substrate.
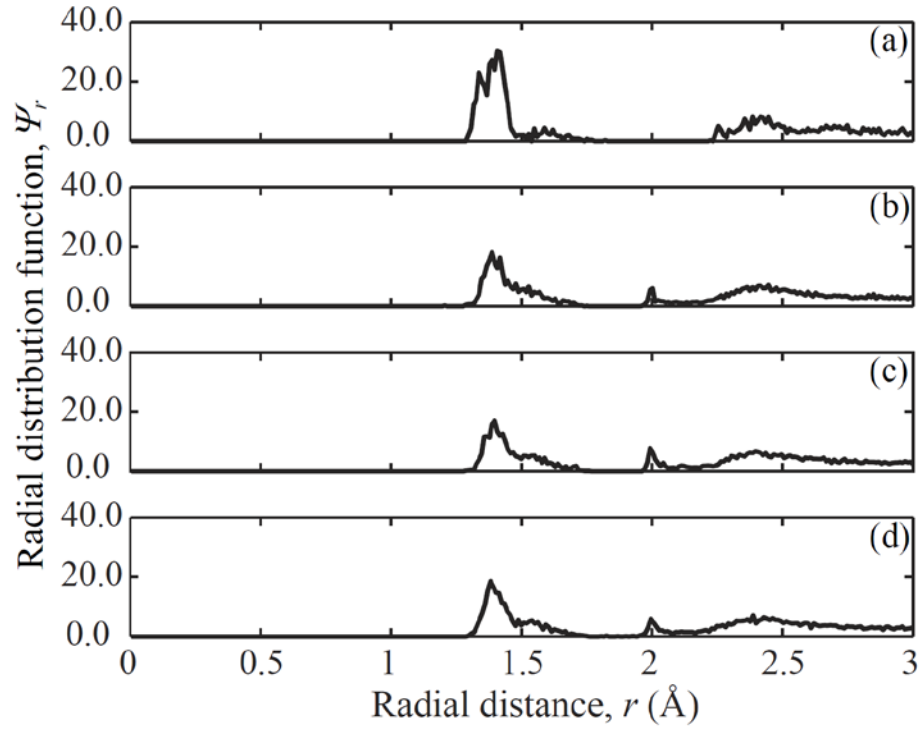
Figure 7. 6 Radial distribution function Ψ_r for deposition energy E_d equal to (*a*) 1, (*b*) 20, (*c*) 80, and (*d*) 120 eV.
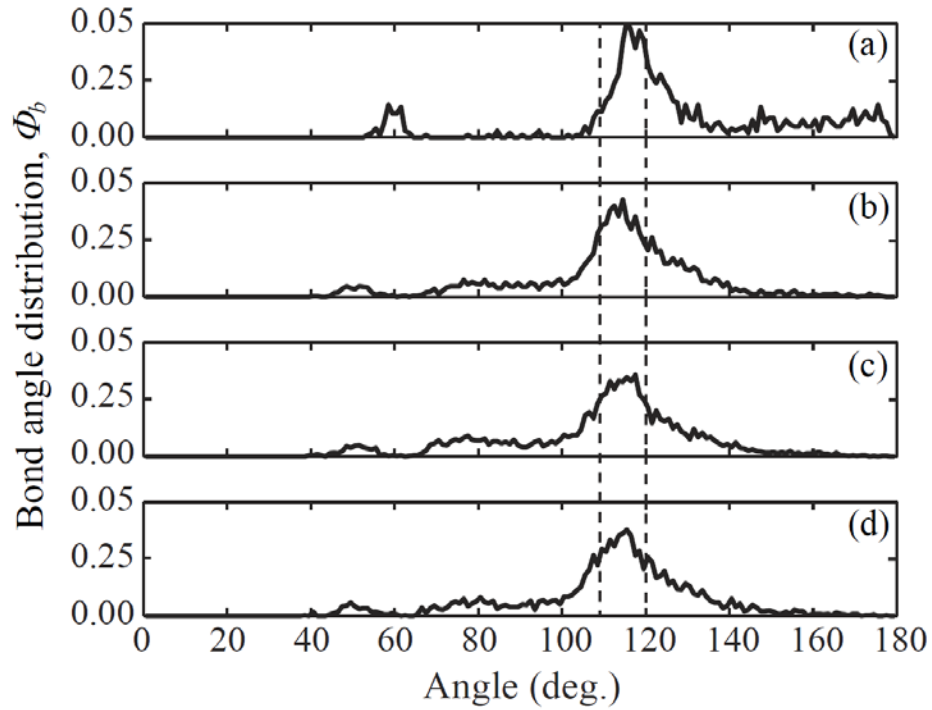
Figure 7. 7 Bond angle distribution Φ_b for deposition energy E_d equal to (*a*) 1, (*b*) 20, (*c*) 80, and (*d*) 120 eV. Bond angles of 109° (pure sp^3 hybridization) and 120° (pure sp^2 hybridization) corresponding to diamond and graphite, respectively, are marked by dashed lines.
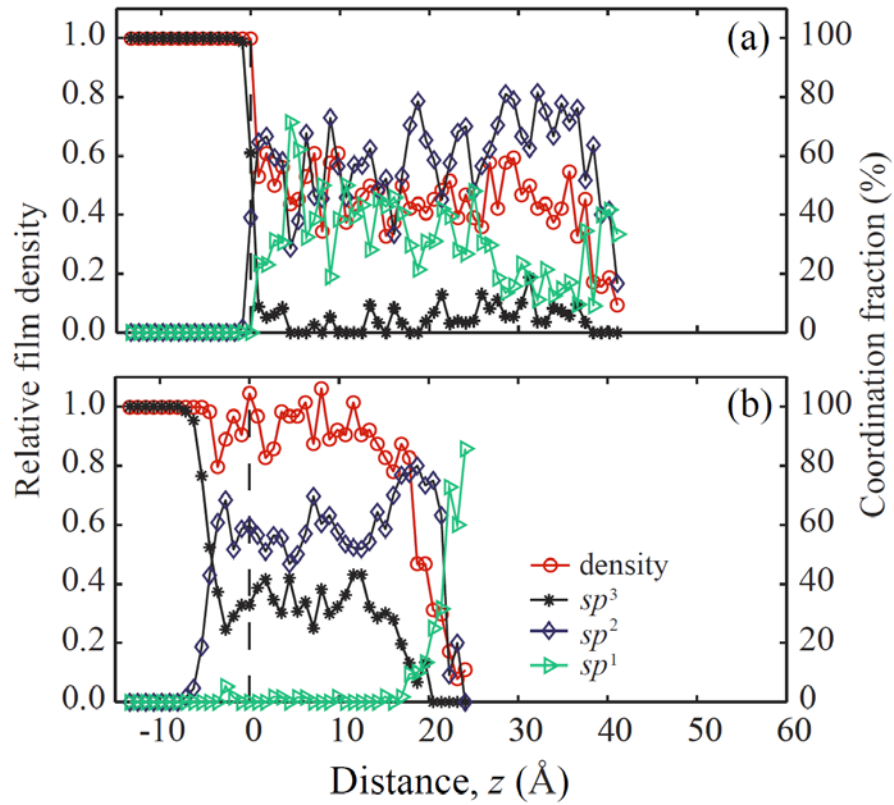
Figure 7. 8 Depth profiles of relative film density and carbon atom hybridization for deposition energy E_d equal to (*a*) 1 and (*b*) 80 eV. The film density was normalized by the density of the diamond substrate.
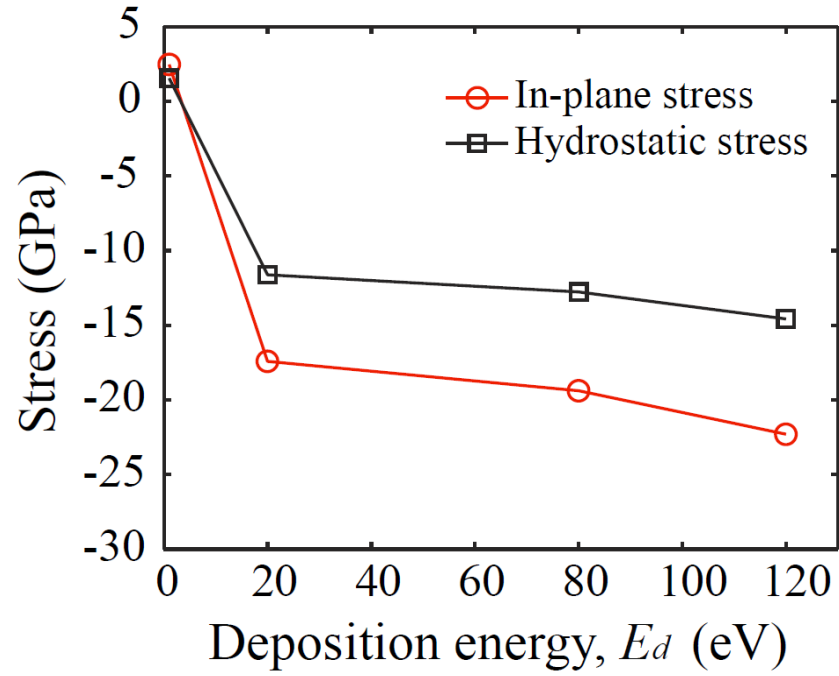
Figure 7. 9 Hydrostatic stress σ_h and in-plane stress σ_i versus deposition energy E_d.
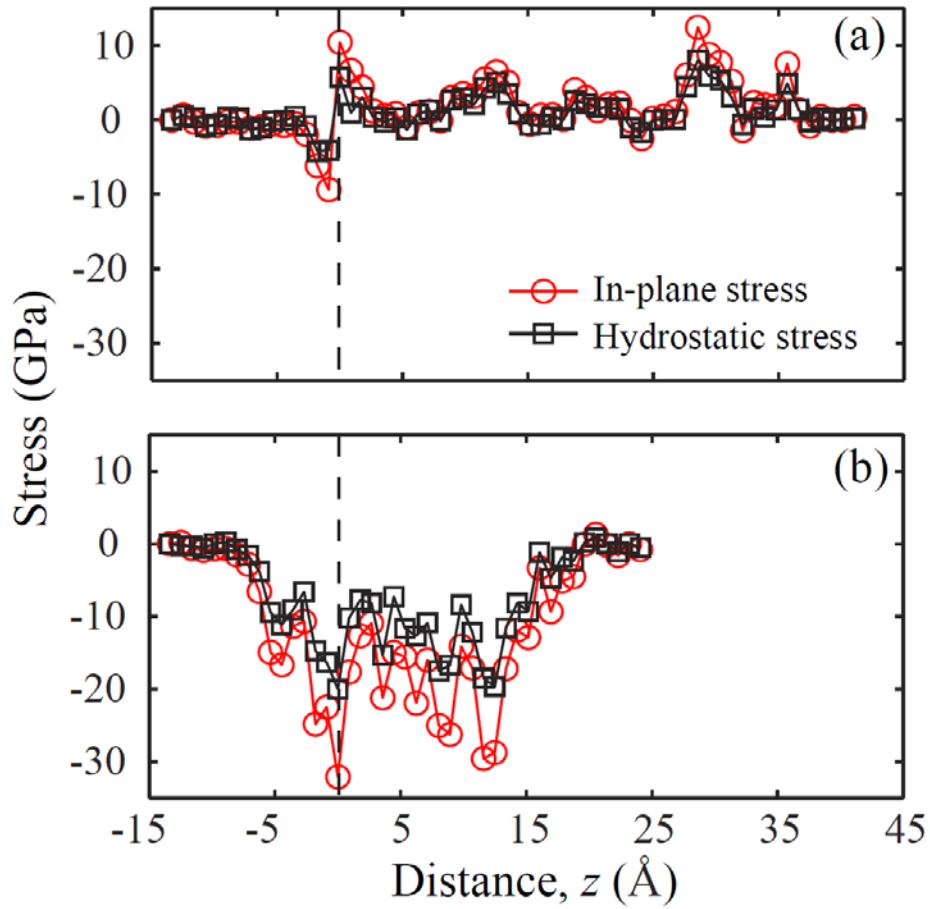
Figure 7. 10 Depth profiles of hydrostatic stress σ_h and in-plane stress σ_i for deposition energy E_d equal to (*a*) 1 and (*b*) 80 eV. The vertical dashed line indicates the original substrate surface.
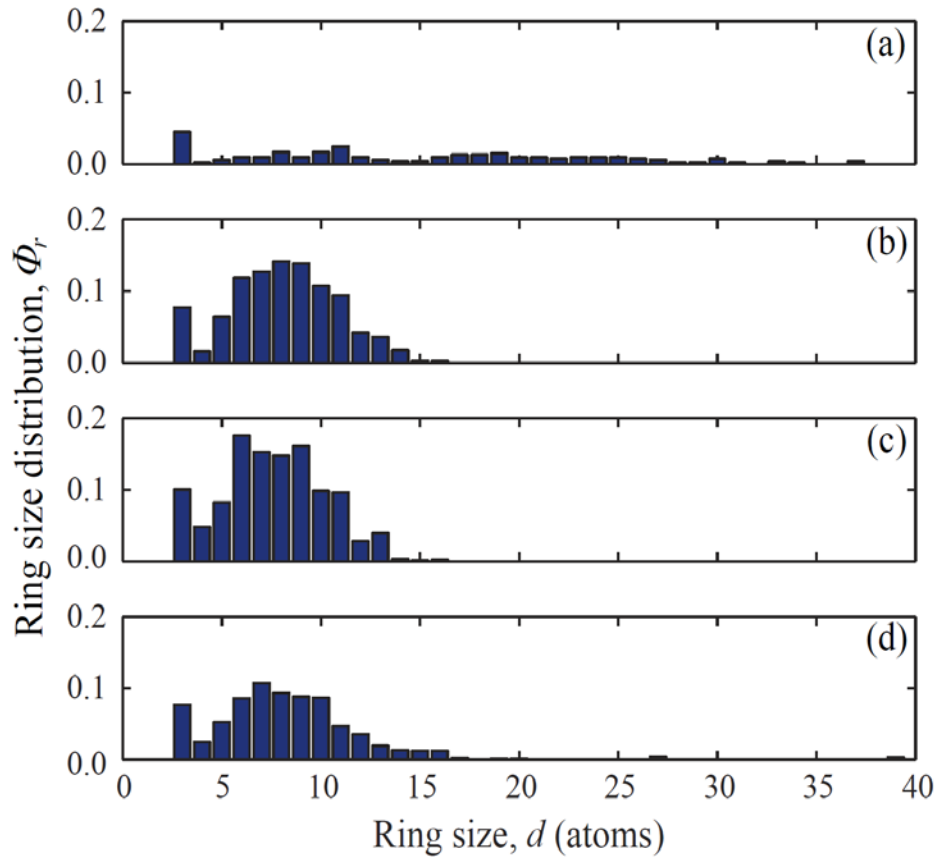
Figure 7. 11 Ring size distribution Φ_r for deposition energy E_d equal to (*a*) 1, (*b*) 20, (*c*) 80, and (*d*) 120 eV.
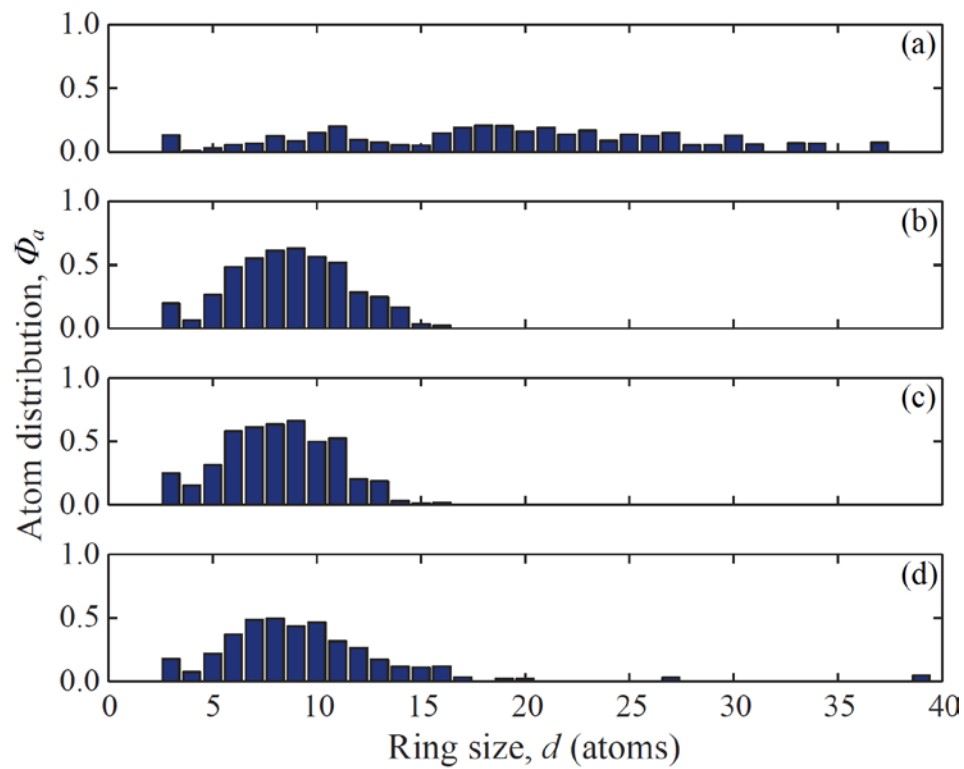
Figure 7. 12 Atom distribution Φ_a for deposition energy E_d equal to (*a*) 1, (*b*) 20, (*c*) 80, and (*d*) 120 eV.
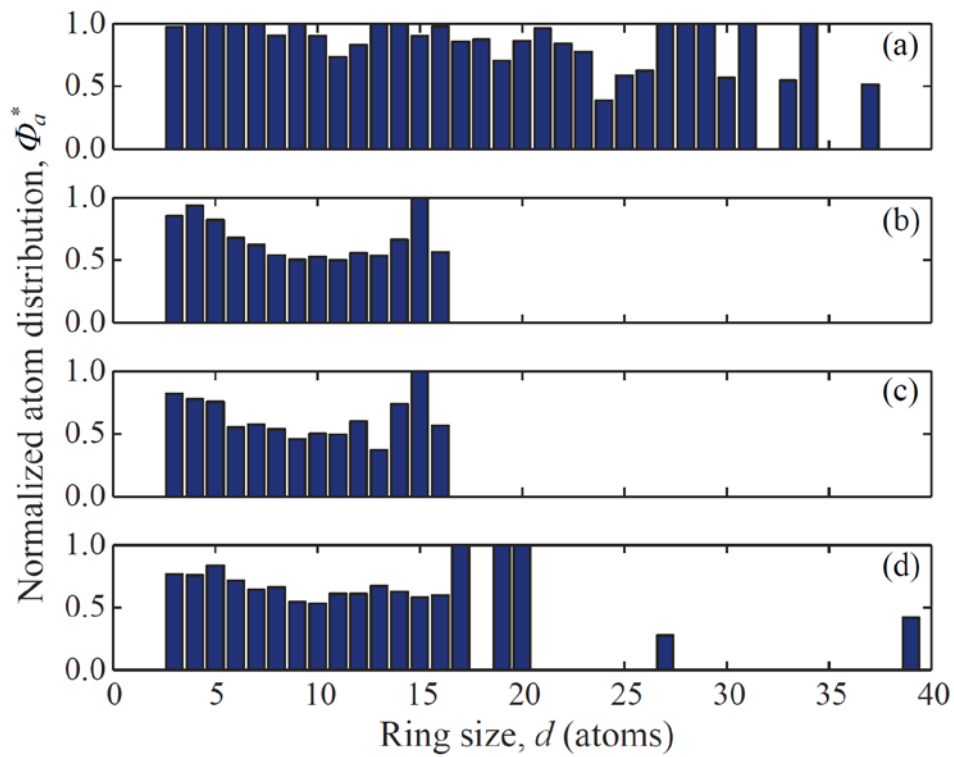
Figure 7. 13 Normalized atom distribution Φ_a^* for deposition energy E_d equal to (*a*) 1, (*b*) 20, (*c*) 80, and (*d*) 120 eV.
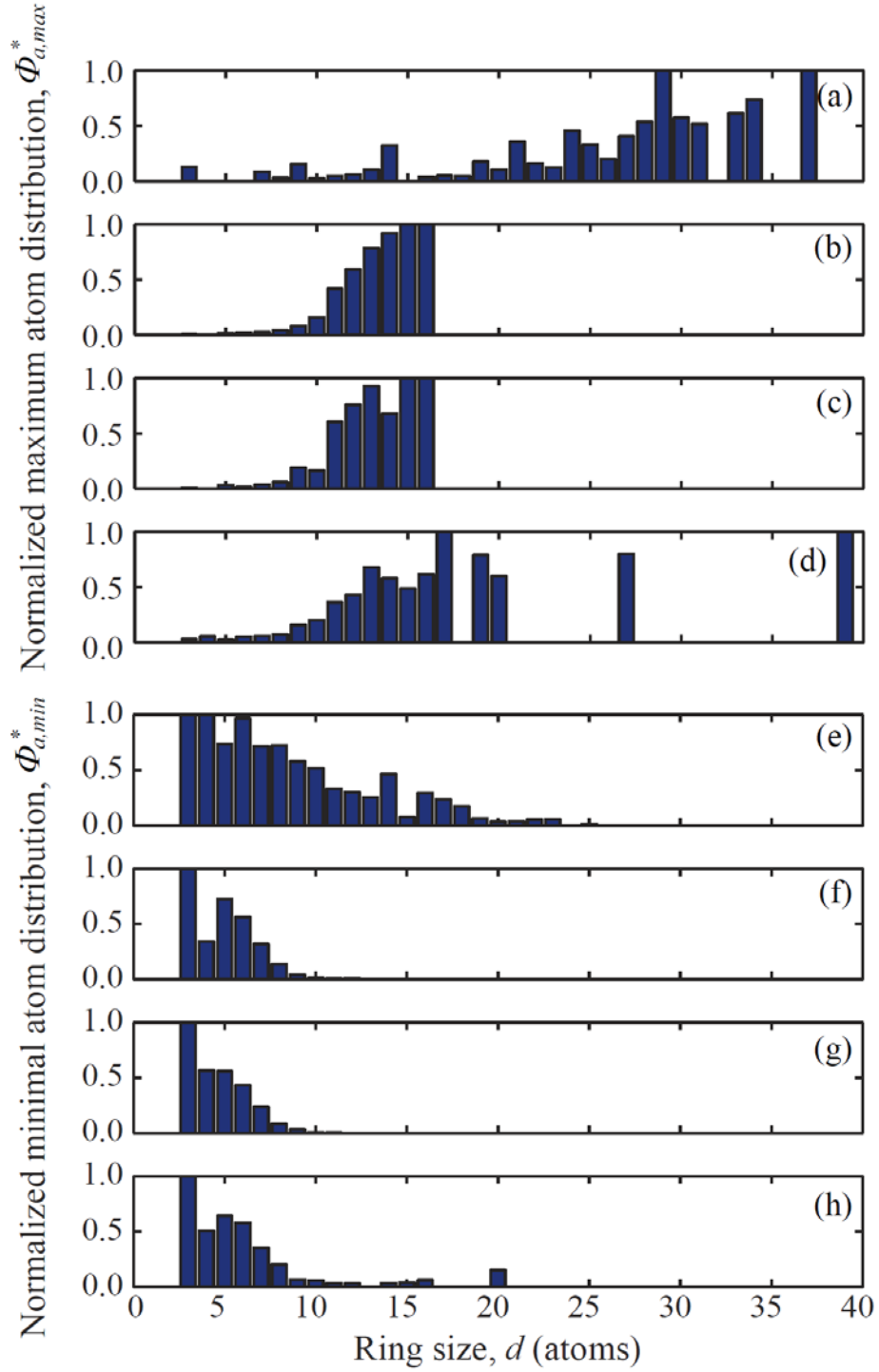
Figure 7. 14   Normalized maximum and minimum atom distributions $\Phi^*_{a,max}$ and $\Phi^*_{a,min}$, respectively, for deposition energy E_d equal to (a,e) 1, (b,f) 20, (c,g) 80, and (d,h) 120 eV.

Chapter 8
Conclusions

In-depth studies of the structure, properties, and stability of ultrathin a-C films used as protective overcoats in HDDs were performed in this dissertation. The carbon film structure was studied by different analytical methods, such as AFM, XPS, Raman spectroscopy, TEM, STEM-EELS, and simulation techniques, such as Monte Carlo and MD methods. Process parameters of FCVA deposition were optimized to minimize the a-C film thickness while maintaining the protective film properties. The thermal stability of both CVD- and FCVA-deposited carbon overcoats was evaluated by both laser exposure and rapid thermal annealing. The main conclusions derived from work included in this dissertation can be summarized as following:

Because of subplantation of energetic C^+ ions during FCVA deposition, a-C films produced by this method demonstrate a multilayer structure. Depth profiles of carbon atom concentration and sp^3 carbon hybridization obtained from the analysis of high-energy-loss spectra of ~20 nm carbon film deposited on silicon show that the film structure consists of a ~4.5-nm-thick interface (intermixing) layer (a mixture of C, Si, and, possibly, SiC), a ~2-nm-thick buffer layer of pure carbon with outward increasing sp^3 fraction, a ~12.5-nm-thick bulk film of constant and high sp^3 fraction (~74%), and a ~1.5-nm-thick surface layer of high sp^2 content. XPS confirms the sp^3 fraction calculated from the C K-edge EELS spectrum. The buffer and surface layers possess similar thicknesses, which depends on the C^+ ion penetration depth controlled by the kinetic energy of the bombarding C^+ ions. It was shown that the minimum thickness of a-C films deposited under FCVA conditions of optimum substrate bias (–100 V) is equal to 3–3.5 nm, which is the total thickness of the buffer and surface layers.

The thickness of FCVA-deposited a-C films can be further reduced by optimizing the deposition angle. Monte Carlo simulation results confirmed by TEM measurements showed a decrease of the a-C film thickness with the increase of the incidence angle and deposition yield (rate) independent of ion fluence but varying with incidence angle according to a relationship derived from sputtering theory. XPS and AFM results demonstrated that sp^3 fractions and topographies of a-C films for incidence angle $<45^o$ are similar to those of films for 0° incidence angle. Considering the incidence angle effect on the thickness, structure, and topography of FCVA-deposited a-C films, the optimum incidence angle for FCVA deposition is predicted to be equal to 45°. Thus, it may be inferred that depending on the C^+ ion fluence, a-C films of only a few nanometers thickness can be obtained by oblique (45° incidence angle) FCVA deposition.

FCVA-deposited a-C films demonstrated higher thermal stability than CVD-deposited a-C:H films. a-C film thermal stability decreased with film thickness. When repetitively heated with a laser, CVD films exhibited atomic carbon re-hybridization and structural changes for laser power >150 mW, whereas the thermal stability of FCVA films of similar thickness was not affected by laser heating even for the maximum laser power (300 mW) used in this study. Laser heating at powers >150 mW induced significant roughening of the CVD films, suggesting that a-C films synthesized by CVD are limited to HAMR conditions of relatively low laser power

heating. The high thermal stability of *a*-C films synthesized by FCVA suggests that these films are prime overcoat candidates for HAMR hard disks.

Rapid thermal annealing experiments on PECVD-deposited *a*-C:H films showed significant structural changes in 3.4-nm-thick *a*-C:H films above a critical peak annealing temperature in the range of ~400–450 ^{o}C. Red-shifting and reduced FWHM of the G peak with increasing maximum annealing temperature above 450 ^{o}C suggested that hydrogen depletion, increase of sp^2 cluster size, and enhancement of carbon network ordering are the most likely factors affecting the structural stability of the *a*-C:H films. XRR and XPS measurements did not reveal discernible changes in film thickness and sp^3 content due to RTA, indicating that oxidization and graphitization of the *a*-C:H films were either secondary or negligible during RTA. Although the RTA treatment used in the present study is more severe than that in HAMR, it suggests that the structural stability of *a*-C:H films deposited on current hard disks by PECVD can be preserved, provided laser heating does not generate temperatures >400 ^{o}C during the read/write operation process of the HAMR disk drives.

MD simulations showed that the properties of ultrathin *a*-C films synthesized by energetic carbon atom deposition strongly depend on the energy of the impinging carbon atoms (deposition energy). Atom collision during deposition led to the development of internal stresses in the film. The highest film density and sp^3 fraction was obtained for deposition energy equal to 80 eV, which produced *a*-C films demonstrating a tight ring size distribution range.

References

Aisenberg, S. and Chabot, R., 1971, "Ionbeam deposition o thin films of diamondlike carbon," J. Appl. Phys., vol. 42, pp. 2953-6.

Akkerman, Z. L., Efstathiadis, H. and Smith, F. W., 1996, "Thermal stability of diamondlike carbon films," J. Appl. Phys., vol. 80, pp. 3068-3075.

Alam, M. and Sun, Q., 1993, "The kinetics of chemical vapor deposited diamond-oxygen reaction," J. Mater. Res., vol. 8, pp. 2870-2878.

Allen, M. P. and Tildesley, D. J., 1989, Computer Simulation of Liquids (Oxford University Press, New York).

Anders, A., Fong, W., Kulkarni, A. V., Ryan, F. W. and Bhatia, C. S., 2001, "Ultrathin diamond-like carbon films deposited by filtered carbon vacuum arcs," IEEE T. Plasma Sci., vol. 29, pp. 768-775.

Anders, A., 2002, "Energetic deposition using filtered cahtodic arc plasmas," Vacuum, vol. 67, pp.673-686.

Anders, S., Diaz, J., Ager, J. W., Lo, R. Y. and Bogy, D. B., 1997, "Thermal stability of amorphous hard carbon films produced by cathodic arc deposition," Appl. Phys. Lett., vol. 71, pp. 3367-3369.

Bandic, Z. Z. and Victora, R. H., 2008, "Advances in magnetic data storage technologies," Proc. IEEE, vol. 96, pp. 1749-1753.

Beghi, M. G., Ferrari, A. C., Bottani, C. E., Libassi, A., Tanner, B. K., Teo, K. B. K. and Robertson, J., 2002, "Elastic constants and structural properties of nanometre-thick diamond-like carbon films," Diam. Relat. Mater., vol. 11, pp. 1062-1067.

Berendsen, H. J. C., Postma, J. P. M., van Gunsteren, W. F., DiNola, A., and Haak, J. R., 1984, "Molecular dynamics with coupling to an external bath," J. Chem. Phys., vol. 81, pp. 3684-3690.

Bhushan, B., Kellock, A. J., Cho, N. H., and Ager III, J. W., 1992, "Characterization of chemical bonding and physical characteristic of diamond-like carbon amorphous carbon and diamond films," J. Mater. Res., vol. 7, pp. 404-410.

Bhushan, B., 1999, "Chemical, mechanical and tribological characterization of ultra-thin and hard amorphous carbon coatings as thin as 3.5 nm: recent developments," Diam. Relat. Mater., vol. 8, pp. 1985-2015.

Biersack, J. P., Berg, S. and Nender, C., 1991, "T-DYN Monte Carlo simulations applied to ion assisted thin film processes," Nucl. Instrum. Meth. Phys. Res. B, vol. 59/60, pp. 21-27.

Biersack, J., 1999, "TRIM-DYNAMIC applied to marker broadening and SIMS depth profiling," Nucl. Instrum. Methods Phys. Res. B, vol. 153, pp. 398-409.

Binning, G., Quate, C. F. and Gerber, C., 1986, "Atomic force microscopy," Phye. Rev. Lett., vol. 56, pp. 930-933.

Binning, G., Rohrer, H., Gerber, C. and Weibel, E., 1982, "Surface studies by scanning tunneling microscopy," Phys. Rev. Lett., vol. 49, pp. 57-61.

Brenner, D. W., 1990, "Empirical potential for hydrocarbons for use in simulating the chemical vapor deposition of diamond films," Phys. Rev. B, vol. 42, pp. 9458–8471

Brenner, D. W., 1992, "Erratum: Empirical potential for hydrocarbons for use in simulating the chemical vapor deposition of diamond films," Phys. Rev. B, vol. 46, pp. 1948–1948

Brenner, D. W., Shenderova, O. A., Harrison, J. A., Stuart, S. J., Ni, B., and Sinnott, S. B., 2002, "A second-generation reactive empirical bond order (REBO) potential energy expression for hydrocarbons," J. Phys: Cond. Matter. vol. 14, pp. 783–802.

Brown, I. G., 1998, "Cathodic arc deposition of films," Annu. Rev. Mater. Sci., vol. 28, pp. 243-269.

Byon, E. and Anders, A., 2003, "Ion energy distribution functions of vacuum arc plasmas," J. Appl. Phys., vol. 93, pp. 1899-1906.

Casiraghi, C., Ferrari, A. C., Ohr, R., Chu, D. and Robertson, J., 2004(A), "Surface properties of ultra-thin tetrahedral amorphous carbon films for magnetic storage technology," Diam. Relat. Mater., vol. 13, pp. 1416-1421.

Casiraghi, C., Ferrari, A. C., Robertson, J., Ohr, R., Gradowski, M. V., Schneider, D. and Hilgers, H., 2004(B), "Ultra-thin carbon layer for high density magnetic storage devices," Diam. Relat. Mater., vol. 13, pp. 1480-1485.

Castiglioni, C., Mapelli, C., Negri, F. and Zerbi, G., 2001, "Origin of the D line in the Raman spectrum of graphite: A study based on Raman frequencies and intensities of polycyclic aromatic hydrocarbon molecules," J. Chem. Phys., vol. 114, pp. 963-974.

Challener, W. A., Peng, C., Itagi, A. V., Karns, D., Peng, W., Peng, Y., Yang, X., Zhu, X., Gokemeijer, N. J., Hsia, Y. T., Ju, G., Rottmayer, R. E., Seigler, M. A. and Gage, E. C., 2009, "Heat-assisted magnetic recording by a near-field transducer with efficient optical energy transfer," Nat. Photon, vol. 3, pp. 220-224.

Chen, Z. Y., Zhao, J. P., Yano, T. and Ooie, T., 2002, "Carbon nitride films with low friction coefficient synthesized by nitrogen-ion-beam-assisted pulsed laser deposition", Diamond Relat. Mater., vol. 11, pp. 1629-1632.

Chhowalla, M., Ferrari, A. C., Robertson, J. and Amaratunga, G. A. J., 2000, "Evolution of sp2 bonding with deposition tem," Appl. Phys. Lett., vol. 71, pp. 1419-1421.

Chhowalla, M., Robertson, J., Chen, C. W., Silva, S. R. P., Davis, C. A., Amaratunga, G. A. J. and Milne, W. I., 1997, "Influence of ion energy and substrate temperature on the optical and electronic properties of tetrahedral amorphous carbon (ta-C) films," J. Appl. Phys., vol. 81, pp. 139-145.

Chung, C. K., Peng, C. C., Wu, B. H. and Chen, T. S., 2007, "Residual stress and hardness behaviors of the two-layer C/Si films," Surf. Coat. Technol., vol. 202, pp. 1149-1153.

Conway, N. M., LLie, A., Robertson, J., Milne, W. I. and Tagliaferro, A., 1998, "Reduction in defect density by annealing in hydrogenated tetrahedral amorphous carbon," Appl. Phys. Lett., vol. 73, pp. 2456-2458.

Cuomo, J. J., Pappas, D. L., Lossy, R., Doyle, J. P., Bruley, J., Di Bello, G. W. and Krakow, W., 1992, "Energetic carbon deposition at oblique angles," J. Vac. Sci. Technol. A, vol. 10, pp. 3414-3418.

Davis, C. A., Knowles, K. M., and Amaratunga, G. A. J., 1995, "Cross-sectional structure of tetrahedral amorphous carbon thin films," Surf. Coat. Technol. vol. 76-77, pp. 316-321

Davis, C. A., Amaratunga, G. A. J., and Knowles, K. M., 1998, "Growth mechanism and cross-sectional structure of tetrahedral amorphous carbon thin films," Phys. Rev. Lett. vol. 80, pp. 3280-3283

Díaz, J., Paolicelli, G., Ferrer, S. and Comin, F., 1996, "Separation of the sp3 and sp2 components in the C1s photoemission spectra of amorphous carbon films," Phys. Rev. B, vol. 54, pp. 8064-8069.

Ding, Q., Wang, L., Hu, T., Wang, Y. and Zhang Y., 2011, "An explanation for laser-induced spallation effect in a-C:H films: altered phase evolution route caused by hydrogen doping," J. Appl. Phys., vol. 109, pp. 013501.

Dong, L., Smith, R. W. and Srolovitz, D. J., 1996, "A two-dimensional molecular dynamics simulation of thin film growth by oblique depositon," J. Appl. Phys., vol. 80, pp. 5682-5690.

Dobisz, E. A., Bandic, Z. Z., Wu, T.-W. and Albrecht, T., 2008, "Patterned media: nanofabrication challenges of future disk drives," Proc. IEEE, vol. 96, pp. 1836-1846.

Dulong, B. J., Haynes, R. D. and Robertson, M. D., 2008, "A study in the computation time required for the inclusion of strain field effects in Bloch-wave simulations of TEM diffraction contrast images," Ultramicroscopy, vol. 108, pp. 415-425.

Erdemir, A. and Donnet, C., 2006, "Tribology of diamond-like carbon films: recent progress and future prospects," J. Phys. D: Appl. Phys., vol. 39, pp. R311-R327

Espinosa, H. D., Peng, B., Moldovan, N., Friedmann, T. A., Xiao, X., Mancini, D. C., Auciello, O., Carlisle, J., Zorman, C. A. and Merhegany, M., 2006, "Elasticity, strength, and toughness of single crystal silicon carbide, ultrananocrystalline diamond, and hydrogen-free tetrahedral amorphous carbon," Appl. Phys. Lett., vol. 89, pp. 073111(1-3),.

Fallon, P. J., Veerasamy, V. S., Davis, C. A., Robertson, J., Amaratunga, G. A. J., Milne, W. I., and Koskinen, J., 1993, "Properties of filtered-ion-beam deposited diamondlike carbon as a function of ion energy," Phys. Rev. B., vol. 48, pp. 4777-4782.

Ferrari, A. C. and Robertson, J., 2000, "Interpretation of Raman spectra of disordered and amorphous carbon," Phys. Rev. B, vol. 61, pp. 14095-14107.

Ferrari, A. C., Rodil, S. E., Robertson, J., and Milne, W. I., 2002, "Is stress necessary to stabilize sp3 bonding in diamond-like carbon?" Diamond Relat. Mater., vol. 11, pp. 994-999.

Ferrari, A. C. and Robertson, J., 2004, "Raman spectroscopy of amorphous, nanosrtructured, diamond-like carbon and nanodiamond," Phil. Trans, R. Soc. Lond. A., vol. 362, pp. 2477-2512.

Ferrari, A. C., 2004, "Diamond-like carbon for magnetic storage disks," Surf. Coat. Technol., vol. 180/181, pp. 190-206.

Ferrari, A. C., Kleinsorge, B., Morrison, N. A., Hart, A., Stolojan, V. and Robertson, J., 1999, "Stress reduction and bond stability during thermal annealing of tetrahedral amorphous carbon," J. Appl. Phys., vol. 85, pp. 7191-7197.

Ferrari, A. C., Rodil, S. E. and Robertson, J., 2003, "Interpretation of infrared and Raman spectra of amorphous carbon nitrides," Phys. Rev. B, vol. 67, pp. 155306-20.

Franzblau, D. S., 1991, "Computation of ring statistics for network models of solids," Phys. Rev. B, vol. 44, pp. 4925-4929

Fung, M. K., Lai, K . H., Chan, C. Y., Bello, I., Lee, C. S., Lee, S. T., Mao, D. S. and Wang, X., 2000, "Mechanical properties and corrosion studies of amorphous carbon on magnetic disks prepared by ECR plasma technique," Thin Solid Films, vol. 368, pp. 198-202.

Goglia, P. R., Berkowitz, J., Hoehn, J., Xidis, A. and Stover, L., 2001, "Diamond-like carbon applications in high density hard disc recording heads," Diam. Relat. Mater., vol. 10, pp. 271-277.

Grierson, D. S., Sumant, A. V., Konicek, A. R., Friedmann, T. A., Sullivan, J. P. and Carpick, R. W., 2010, "Thermal stability and rehybridization of carbon bonding in tetrahedral amorphous carbon," J. Appl. Phys., vol. 107, pp. 033523(1-5).

Grill, A., 1997, "Tribology of diamondlike carbon and related materials: an updatd review," Surf. Coat. Technol., vol. 94-95, pp. 507-513.

Grill, A., 1999, "Diamond-like carbon: state of the art," Diam. Relat. Mater., vol. 8, pp. 428-434.

Grill, A., Patel, V. and Meyerson, B. S., 1990, "Optical and tribological properties of heat-treated diamond-like carbon," J. Mater. Res., vol. 5, pp. 2531-2537.

Gupta, S., Weiner, B. R., Nelson, W. H. and Morell, G., 2003, "Ultraviolet and visible Raman spectroscopic investigations of nanocrystalline carbon thin films grown by bias-assisted hot-filament chemical vapor deposition," J. Raman Spect., vol. 34, pp. 192-198.

Guthrie, M., Tulk, C. A., Benmore, C. J., Xu, J., Yarger, J. L., Klug, D. D., Tse, J. S., Mao, H-K., and Hemley, R. J., 2004, "Formation and structure of a dense octahedral glass," Phys. Rev. Letters vol. 93, pp. 115502

Guttman, L., 1990, "Ring structure of the crystalline and amorphous forms of silicon dioxide," J. Non-Cryst. Solids, vol. 116, pp. 145-147

Hauert, R., 2004, "An overview on the tribological behavior of diamond-like carbon in technical and medical applications," Tribol. Int., vol. 37, pp. 991-1003.

Haynes, W. M., 2011, CRC Handbook of Chemistry and Physics, 92nd ed., CRC Press, New York.

Ikemoto, J.-I., Imai, Y. and Nakagawa, S., 2008, "Control of curie temperature of FePt(Cu) films prepared from Pt(Cu)/Fe bilayers," IEEE Trans. Mag., vol. 44, pp. 3543-3546.

Jager, H. U. and Albe, K., 20002, "Molecular-dynamics simulations of stready-state growth of ion-deposited tetrahedral amorphous carbon films," J. Appl. Phys., vol. 88, pp. 1129-1135

Jalili, N., and Laxminarayana, K., 2004, "A review of atomic force microscopy imaging system: application to molecular metrology and biological sciences," Mechatronics, vol. 14, pp. 907-945.

Jayawardhana, S., Kostovski, G., Mazzolini, A. P. and Stoddart, P. R., 2011, "Optical fiber sensor based on oblique angle deposition," Appl. Optics, vol. 50, pp. 155-162.

Kalish, R., Lifshitz, Y., Nugent, K. and Prawer, S., 1999, "Thermal stability and relaxation in diamond-like-carbon. A Raman study of films with different sp3 fractions (ta-C to a-C)," J. Appl. Phys., vol. 74, pp. 2936-2938.

Kaukonen, H. –P., and Nieminen, R. M., 1992, "Molecular-dynamics simulation of the growth of diamondlike films by energetic carbon-atom beams," Phys. Rev. Lett. vol. 68, pp. 620-623

Kelires, P. C. , 2000, "Intrinsic stress and local rigidity in tetrahedral amorphous carbon," Phys. Rev. B., vol. 62, pp. 15686-15694.

Kelires, P. C., 2001, "Intrinsic stress and stiffness variations in amorphous carbon," Diam. Relat. Mater., vol. 10, pp. 139-144.

King, S. V., 1967, "Ring configuration in a random work model of vitreous silica," Nature vol. 213, pp. 1112

Knight, D. S. and White, W. B., 1989, "Characterization of diamond films by Raman spectroscopy," J. Mater. Res., vol. 4, pp. 385-393.

Kohara, S., Akola, J., Morita, H., Suzuya, K., Weber, J. K. R., Wilding, M. C., and Benmore, C. J., 2011, "Relationship between topological order and glass forming ability in densely packed enstratite and forsterite composition glasses," *PNAS* vol. **108**, pp. 14780-14785

Kryder, M. H., Gage, E. C., McDaniel, T. W., Challener, W. A., Rottmayer, R. E., Ganping, J., Hsia, Y.-T. and Erden, M. F., 2008, "Heat assisted magnetic recording," Proc. IEEE, vol. 96, pp. 1810-1835.

Krishnaswamy, J., Rengan, A., Narayan, J., Vedam, K. and McHargue, C. J., 1989, "Thin-film deposition by a new laser ablation and plasma hybrid technique," Appl. Phys. Lett., vol. 54, pp. 2455-2457.

Kulikovsky, V., Vorlicek, V., Bohac, P., Kurdyumov, A., Deyneka, A. and Jastrabik, L., 2003, "Thermal stability of microhardness and internal stress of hard a-C films with predominantly sp2 bonds," Diam. Relat. Mater., vol. 12, pp. 1378-1384.

Leng, Q., Han, H., Mao, M., Hiner, C. and Ryan, F., 2000, "Magnetic dead layers in NiFe/Ta and NiFe/Si/diamond-like carbon films," J. Appl. Phys., vol. 87, pp. 6621-6623.

Levesque, D. and Verlet, L., 1993, "Molecular dynamics and time reversibility," J. Stat. Phys., vol. 72, pp. 519–537.

Li, D. J., Guruz, M. U., Bhatia, C. S. and Chung Y.-W., 2002, "Ultrathin CNx overcoats for 1Tb/in.2 hard disk drive systems", Appl. Phys. Lett., vol. 81, pp. 1113-1115.

Lifshitz, Y., Kasi, S. R., Rabalais, J. W., and Eckstein, W., 1990, "Subplantation model for film growth from hyperthermal species," Phys. Rev. B vol. 41, pp. 10468.

Liu, D. and Bensetter, G., 2005, "Conducting atomic force microscopy for nanoscale electron emissions from various diamond-like carbon films," Appl. Surf. Sci., vol. 249, pp. 315-321.

Liu, D., Benstetter, G., Lodermeier, E. and Vancea, J., 2003, "Influence of the incident angle of energetic carbon ions on the properties of tetrahedral amorphous carbon (ta-C) films," J. Vac. Sci. Technol. A, vol. 21, pp. 1665-1670.

Liu, F.-X. and Wang, Z.-L., 2009, "Thickness dependence of the structure of diamond-like carbon films by Raman spectroscopy," Surf. Coat. Technol., vol. 203, pp. 1829-1832.

Liu, F.-X., Yao, K.-L. and Liu, Z.-L., 2007, "Substrate tilting effect on structure of tetrahedral amorphous carbon films by Raman spectroscopy," Surf. Coat. Technol., vol. 201, pp. 7235-7240.

Lu, Y., Peng, C., Ganesan, Y., Huang, J. Y. and Lou, J., 2011, "Quantitative in situ TEM tensile testing of an individual nickel nanowire," Nanotechnology, vol. 22, pp. 355702(1-6).

Lucas, C. A., Nguyen, T. D. and Kortright, J. B., 1991, "X-ray reflectivity measurements of the expansion of carbon films upon annealing," Appl. Phys. Lett., vol. 59, pp. 2100-2102.

Ma, T., Hu, Y., Wang, H. and Li, X., 2007, "Effect of impact angle and substrate roughness on growth of diamondlike carbon films," J. Appl. Phys., vol. 101, pp. 014901(1-5).

Ma, T., Hu, Y., Wang, H. and Li, X., 2007, "Microstructure and stress properties of ultrathin diamondlike carbon films during growth: Molecular dynamics simulations," Phys. Rev. B, vol. 75, pp. 035425-8

Ma, Y., Chen, X. and Liu, B., 2012, "Experimental study of lubricant depletion in heat assisted magnetic recording over the lifetime of the device", Tribol. Lett., vol. 47, pp. 175-182.

Marks, N. A., McKenzie, D. R., and Pailthorpe, B. A., 1996, "Molecular-dynamics study of compressive stress generation," Phys. Rev. B, vol. 53, pp. 4117-4124

Marks, N. A., 1997, "Evidence for subpicosecond thermal spikes in the formation of tetrahedral amorphous carbon," Phys. Rev. B, vol. 56, pp. 2441-2446

Marks, N. A., 2005, "Thin film deposition of tetrahedral amorphous carbon: a molecular dynamics study," Diamond Relat. Mater., vol. 14, pp. 1223-1232

Martin, J. D., Goettler, S. J., Fosse, N., and Iton, L., 2002, "Designing intermediate-range order in amorphous materials," Nature vol. 419, pp. 381-384

McKenzie, D. R., 1996, "Tetrahedral bonding in amorphous carbon," Rep. Prog. Phys., vol. 59, pp. 1611-1664.

Monteiro, O. R., 2001, "Thin film synthesis by energetic condensation," Annu. Rev. Mater. Res., vol. 31, pp. 111-137.

Nevot, L. and Croce, P., 1980, "Caractérisation des surfaces par réflexion rasante de rayons X. Application à l'étude du polissage de quelques verres silicates", Rev. Phys. Appl., vol. 15, p.761-779.

Orwa, J. O., Andrienko, I., Peng, J. L. and Prawer, S., 2004, "Thermally induced sp2 clustering in tetrahedral amorphous carbon (ta-C) films," J. Appl. Phys., vol. 96, pp. 6286 - 6297.

Pan. L. and Bogy, D. B., 2009, "Data storage: heat-assisted magnetic recording," Nat. Photon., vol. 3, pp. 189-190.

Parratt, L. G., 1954, "Surface studies of solids by total reflection of X-rays", Phys. Rev., vol. 95, pp. 359-369.

Pharr, G. M., Callahan, D. L., McAdams, S. D., Tsui, T. Y., Anders, S., Anders, A., Ager III, J. W., Brown, I. G., Bhatia, C. S., Silva, S. R. P. and Robertson, J., 1996, "Hardness, elastic modulus, and structure of very hard carbon films produced by cathodic-arc deposition with substrate pulse biasing," Appl. Phys. Lett., vol. 68, pp. 779-781.

Plimpton, S. J., 1995, "Fast parallel algorithms for short-range molecular dynamics," J. Comp. Phys., vol. 117, pp. 1-9

Polo, M. C., Andujar, J. L., Hart, A., Robertson, J., and Milne, W. I., 2000, "Preparation of tetrahedral amorphous carbon films by filtered cathodic vacuum arc deposition," Diamond Relat. Mater., vol. 9, pp. 663-667.

Rino, J. P., Ebbsjo, I., Branicio, P. S., Kalia, R. K., Nakano, A., Shimojo, F., and Vashishta, P., 2004, "Short- and intermediate-range structural correlations in amorphous silicon carbide: A molecular dynamics study," Phys. Rev. B, vol. 70, 045207

Robertson, J., 2001, "Ultrathin carbon coatings for magnetic storage technology," Thin Solid Films, vol. 383, pp. 81-88.

Robertson, J., 2002, "Diamond-like amorphous carbon," Mater. Sci. Eng. R, vol. 37, pp. 129-281.

Robertson, J., 2003, "Requirements of ultrathin carbon coatings for magnetic storage technology," Tribol. Int., vol. 36, pp. 405-415.

Rong, C.-B., Yang, L. and Liu, J.-P., 2007, "Curie temperatures of annealed FePt nanoparticle systems," J. Appl. Phys., vol. 101, pp. 09K505.

Roux, S. L., and Jund, P., 2010, "Ring statistics analysis of topological networks: New approach and application to amorphous GeS_2 and SiO_2 systems," Comp. Mater. Sci., vol. 49, pp. 70-83

Roux, S. L., and Jund, P., 2010, "ISAACS – Interactive structure analysis of amorphous and crystalline systems," J. Appl. Cryst., vol. 43, pp. 181-185

Samad, M. A., Rismani, E., Yang, H., Sinha, S. K. and Bhatia, C. S., 2011, "Overcoat free magnetic media for lower magnetic spacing and improved trobological properties for higher areal densities," Tribol. Lett., vol. 43, pp. 247-256.

Savvides, N. and Window, B., "Diamondlike amorphous carbon films prepared by magnetron sputtering of graphite," J. Vac. Sci. Technol. A, vol. 3, pp. 2386-2390.

Schroeder, B. and Gibson, G. A., 2007, "Understanding disk failure rates: what does an MTTF of 1,000,000 hours mean to you?", ACM Trans. Storage, vol. 3, Article 8.

Smith, E. and Dent, G., 2005, "Modern Raman spectroscopy: a practical approach," Hoboken, NJ : J. Wiley.

Shin, J.-K., Lee, C.-S., Lee, K.-R. and Eun, K. Y., 2001, "Effect of residual stress on the Raman-spectrum analysis of tetrahedral amorphous carbon films," Appl. Phys. Lett., vol. 78, pp. 631-633.

Siegal, M. P., Provencio, P. N., Tallant, D. R., Simpson, R. L., Kleinsorge, B. and Milne, W. I., 2000, "Bonding topologies in diamondlike amorphous-carbon films," Appl. Phys. Lett., vol. 76, pp. 2047-2049.

Sigmund, P., 1969, "Theory of sputtering. I. Sputtering yield of amorphous and polycrystalline targets," Phys. Rev., vol. 184, pp. 383-416.

Simone, A., Javier, D., Joel, III, W. A., Yu, L. R. and David, B. B., 1997, "Thermal stability of amorphous hard carbon films produced by cathodic arc deposition," J. Appl. Phys., vol. 71, pp. 3367-3369.

Stillinger, F. H., and Weber, T. A., 1985, "Computer simulation of local order in condensed phases of silicon," Phys. Rev. B, vol. 31, pp. 5262–5271.

Stipe, B. C., Strand, T. C., Poon, C. C., Balamane, H., Boone, T. D., Katine, J. A., Li, J.-L., Rawat, V., Nemoto, H., Hirotsune, A., Hellwig, O., Ruiz, R., Dobisz, E., Kercher, D. S., Robertson, N., Albrecht, T. R. and Terris, B. D., 2011, "Magnetic recording at 1.5 Pb m-2 using an integrated plasmonic antenna," Nat. Photon., vol. 4, pp. 484-488.

Stuart, S. J., Tutein, A. B., and Harrison, J. A., 2002, "A reactive potential for hydrocarbons with intermolecular interactions," J. Chem. Phys., vol. 112, pp. 6472–6486.

Tagawa, N. and Tani, H., 2011, "Lubricant depletion characteristics induced by rapid laser heating in thermally assisted magnetic recording," IEEE Trans. Mag., vol. 47, pp. 105-110.

Tai, F. C., Lee, S. C., Chen, J., Wei, C. and Chang, S. H., 2009, "Multipeak fitting analysis of Raman spectra on DLCH film," J. Raman Spect., vol. 40, pp. 1055-1059.

Takabayashi, S., Okamoto, K., Sakaue, H., Takahagi, T., Shimada, K. and. Nakatani, T, 2008, "Annealing effect on the chemical strucutre of diamondlike carbon," J. Appl. Phys., vol. 104, pp. 043512.

Tersoff, J., 1988, "New empirical approach for the structure and energy of covalent systems," Phys. Rev. B vol. 37, pp. 6991–7000

Tersoff, J., 1989, "Modeling solid-state chemistry: interatomic potentials for multicomponent systems," Phys. Rev. B vol. 39, pp. 5566–5568

Tsai, H. and Bogy, D. B., 1987, "Critical review: characterization of diamondlike carbon films and their application as overcoats on thin-film media for magnetic recording," J. Vac. Sci. Technol., vol. A5(6), pp. 3287-3312,

Voevodin, A. A. and Donley, M. S., 1996, "Preparation of amorphous diamond-like carbon by pulsed laser deposition: a critical review," Surf. Coat. Technol., vol. 82, pp. 199-213.

Wan, D. and Komvopoulos, K., 2004, "Transmission electron microscopy and electron energy loss spectroscopy analysis of ultrathin amorphous carbon films," J. Mater. Res., vol. 19, pp. 2131-2136.

Wan, D. and Komvopoulos, K., 2006, "Probabilistic analysis of tertrahedral carbon hybridization in amorphous carbon films," Appl. Phys. Lett., vol. 88, pp. 221908(1-3).

Wan, D. and Komvopoulos, K., 2007, "Tetrahedral and trigonal carbon atom hybridization in thin amorphous carbon films synthesized by radio-frequency sputtering," J. Phys. Chem. C, vol. 111, pp. 9891-9896.

Wang, D.-L., Seki, T., Takanashi, K., Shima, T., Li, G.-Q., Saito, H. and Ishio, S., 2008, "Dot size dependence of magnetization reversal process in L10-FePt dot arrays," IEEE Trans. Mag., vol. 44, pp. 3464-3467.

Wang, J.-P., 2008, "FePt magnetic nanoparticles and their assembly for future magnetic media," Proc. IEEE, vol. 96, pp. 1847-1863.

Wang, N. and Komvopoulos, K., 2011, "Thermal stability of ultrathin amorphous carbon films for energy-assisted magnetic recording," IEEE Trans. Magn., vol. 47, pp. 2277-2282.

Wang, N. and Komvopoulos, K., 2012, "Incidence angle effect of energetic carbon ions on deposition rate, topography, and structure of ultrathin amorphous carbon films deposited by filtered cathodic vacuum arc." IEEE Trans. Magn. vol. 48, pp. 2220-2227.

Wang, N. and Komvopoulos, K., 2013, "The multilayered structure of ultrathin amorphous carbon films synthesized by filtered cathodic vacuum arc deposition," J. Mater. Rev. 28, pp. 2124-2131

Wei, Q. and Narayan, J., 2000, "Superhard diamondlike carbon: preparation, theory, and properties," Int. Mater. Rev., vol. 45, pp. 133-164.

Wei, Q., Li, K.-D., Lian, J. and Wang, L., 2008, "Angular dependence of sputtering yield of amorphous and polycrystalline materials," J. Phys. D: Appl. Phys., vol. 41, pp. 17002(1-4).

Wesner, D., Krummacher, S., Carr, R., Sham, T. K., Strongin, M., Eberhardt, W., Weng, S. L., Williams, G., Howells, M., Kampas, F., Heald, S. and Smith, F. W., 1983, "Synchrotron-radition studies of the transition of hydrogenated amorphous carbon to graphitic carbon," Phys. Rev. B, vol. 28, pp. 2152-2156.

Wood, R., 2009, "Future hard disk drive systems," J. Magn. Magn. Mater., vol. 321, pp. 555-561.

Wormington, M., Panaccione, C., Matney, K. M. and Bowne, D. K., 1999, "Characterization of structures from X-ray scattering data using genetic algorithms", Philos. Trans, R. Soc. London, Ser. A, vol. 357, pp. 2827-2850.

Wu, R. L. C., Miyoshi, K., Vuppuladhadium, R. and Jackson, H. E., 1992, "Physical and tribological properties of rapid thermal annealed diamond-like carbon films," Surf. Coat. Technol., vol. 54-55, pp. 576-580.

Xu, S., Tay, B. K., Tan, H. S., Zhong, L., Tu, Y. Q., Silva, S. R. P. and Milne, W. I., 1996, "Properties of carbon ion deposited tetrahedral amorphous carbon films as a function of ion energy," J. Appl. Phys., vol. 79, pp. 7234-7240.

Yang, Y., Aryal, M., Mielczarek, K., Hu, W. and Zakhidov, A., 2010, "Nanoimprinted P3HT/C60 solar cells optimized by oblique deposition of C60," J. Vac. Sci. Techol. B, vol. 28, pp. 1071-1023.

Yao, Y. and Thölen, A., 2000, "TEM investigation on stress contrast and interfaces of contacting particles," Mater. Charact., vol. 44, pp. 441-452.

Yasui, N., Inaba, H., Furusawa, K., Saito, M. and Ohtake, N., 2009, "Characterization of head overcoat for 1 Tb/in2 magnetic recording," IEEE Trans. Mag., vol. 45, pp. 805-809.

Yuan, X., and Cormack, A. N., 2002, "Efficient algorithm for primitive ring statistics in topological networks," Comp. Mater. Sci. vol. 24, pp. 343-360

Yuan, Z.-M., Liu, B., Zhou, T., Goh, C. K., Ong, C. L., Cheong, C. M. and Wang, L., 2009, "Perspectives of magnetic recording system at 10 Tb/in2," IEEE Trans. Magn., vol. 45, pp. 5038-5043.

Yusop, M. Z., Yamaguchi, K., Suzuki, T., Ghosh, P., Hayashi, A., Hayashi, Y. and Tanemura, M., 2011, "Morphology and size of ion induced carbon nanofibers: effect of ion incidence angle, sputtering rate, and temperature," Jpn. J. Appl. Phys., vol. 50, pp. 01AF10(1-6).

Zhang, H.-S. and Komvopoulos, K., 2008, "Direct-current cathodic vacuum arc system with magnetic-field mechanism for plasma stabilization," Rev. Sci. Instrum., vol. 79, pp. 073905(1-7).

Zhang, H.-S. and Komvopoulos, K., 2009(A), "Synthesis of ultrathin carbon films by direct current filtered cathodic vacuum arc," J. Appl. Phys., vol. 105, pp. 083305(1-7).

Zhang, H.-S. and Komvopoulos, K., 2009(B), "Surface modification of magnetic recording media by filtered cathodic vacuum arc," J. Appl. Phys., vol. 106, pp. 093504(1-7).

Zhong, M., Zhang, C., Luo, J. and Lu, X., 2009, "The protective properties of ultra-thin diamond like carbon films for high density magnetic storage devices," Appl. Surf. Sci., vol. 256, pp. 322-328.

Zhu, J., Han, J., Han, X., Schlaberg, H. I. and Wang, J., 2008, "sp3-rich deposition conditions and growth mechanism of tetrahedral amorphous carbon films deposited using filtered arc," J. Appl. Phys., vol. 104, pp. 013512(19).